Universitat Autònoma de Barcelona

Inference of cosmological and black holes population parameters using gravitational waves data

Christos Karathanasis

Universitat Autònoma de Barcelona, Department of Physics

Institut de Fisica d'Altes Energies (IFAE)

Inference of cosmological and black holes population parameters using gravitational waves data

PhD thesis by

Christos Karathanasis

Director:

Dr. Lluïsa Maria Mir

Tutor:

Prof. Eduard Massó

October 2022

Introduction

One of the biggest and unexpected discoveries in physics was the fact that the Universe is expanding. In 1912, Vesto Slipher discovered that light from galaxies was redshifted, which at that time did not lead to the conclusion that the Universe is expanding, but was later interpreted as galaxies receding from the Earth. In 1915, Einstein introduced the theory of General Relativity, which, in 1922, was used by Alexander Friedmann to provide theoretical evidence that the Universe is expanding. In 1924, Knut Lundmark, found observational evidence for Universe's expansion. In 1927, Georges Lemaître independently reached a similar conclusion as Friedmann on a theoretical basis, and also presented observational evidence for a linear relationship between distance to galaxies and their recessional velocity. Finally, in 1929, Edwin Hubble observationally confirmed Lundmark's and Lemaître's findings.

Nowadays, it is well believed that the Universe is expanding, but the rate at which it is expanding today is unknown. Current measurements based on observational data from the early and late life of the Universe indicate a statistically significant difference that can not be explained simply from systematic uncertainties. This difference between late and early time measurements led to a tension for the value of the current expansion rate of the Universe.

General Relativity is currently the most successful theory of gravity. Among its various predictions, one of the most important is the existence of gravitational waves. The first gravitational waves detection in 2015 opened a new window for observing the Universe. Gravitational waves observations are useful for a plethora of different physical phenomena, like astrophysics, black hole physics, gravity theories beyond General Relativity and more.

However, gravitational waves observations are most useful for cosmological estimations. This is because luminosity distance is directly embedded in gravitational waves data, which allows a unique estimation of cosmological parameters, independent of other measurements.

In this thesis we will present methodologies to use gravitational waves data to infer cosmological parameters. We will focus on cosmological estimations, but we will also see that we can infer models and parameters of astrophysical significance. We will also present results and constraints on results that govern theories beyond General Relativity.

Contents

List of Figures

List of Tables

Chapter 1

Theoretical Background

Gravity has always been one of the most elusive fundamental notions of nature. Even though it is the one that we interact with the most in our daily lives, the nature of gravity prevents us from understanding it in depth. Humanity relies on experiments to create and validate theories that describe nature. One of the fundamental traits of gravity is its weakness. Gravity is very weak and performing experiments to understand it in extreme cases requires large masses, something that scientists are not able to do yet. For many years our only way of studying gravity was with simple experiments in Earth. That changed when it was understood that gravity governs the large scale motion of objects like planets, galaxies, galaxy clusters, etc. This discovery led humanity on exploring gravity through the Universe. The latest and most successful theory for the nature and effects of gravity is the theory of General Relativity.

1.1 Basics of the Theory of General Relativity

The theory of General Relativity (GR) was created by Albert Einstein in 1915. Einstein realized that space and time can be combined in one 4-dimensional manifold, called spacetime. In this framework, gravity is merely the effect of curved spacetime. The presence of mass or energy curves spacetime, which leads to the curved physical trajectories of freely falling observers.

Since GR is a theory that incorporates the curvature of spacetime into physical

notions, it is necessary to be able to calculate lengths of paths that particles follow in that spacetime. For this we use the metric tensor $g_{\mu\nu}$ (simply referred to as the metric for the rest of the text), which is one of the key tensors in GR and serves to define the line element and get the lengths of paths in a given spacetime. From now on Greek letters in tensors will be used for the description of all dimensions, time ($t = x_0$) and spatial coordinates (x_i), whereas latin letters will only describe spatial coordinates. Also following Einstein's notation up and down repeated indices imply summation over all possible combinations. Given a manifold with a metric $g_{\mu\nu}$, the line element is written as:

$$ds^2 = g_{\mu\nu} dx^\mu dx^\nu, \tag{1.1}$$

where $dx^\mu = (dt, dx^i)$. Having a metric, we can also define a new tensor operation called contraction:

$$X_{\alpha,\beta,...\sigma...} = g^{\mu\nu} X_{\alpha\beta...\mu\nu...\sigma...}, \tag{1.2}$$

which allows to reduce the number of indexes of a tensor, or even contract all the indexes and create a scalar. In the case of a flat spacetime (i.e. no curvature) the metric takes the special form $\eta_{\mu\nu} = diag(-1, 1, 1, 1)$. Consequently, in this case we have:

$$(ds^2)_{flat} = \eta_{\mu\nu} dx^\mu dx^\nu = -c^2 dt^2 + dx_i dx^i, \tag{1.3}$$

where c is the speed of light. The spacetime in this case is called Minkowski spacetime. In the Minkowski spacetime, the physical trajectories of freely falling observers are straight lines.

In GR, freely falling observers follow physical trajectories, which are called geodesics and depend on the curvature of spacetime. Geodesics are defined from the following equation:

$$\frac{d^2 x^\mu}{d\lambda^2} + \Gamma^\mu_{\rho\sigma} \frac{dx^\rho}{d\lambda} \frac{dx^\sigma}{d\lambda} = 0, \tag{1.4}$$

where λ is the affine parameter that parametrizes the trajectory and Γ are the Christoffel

symbols, which are given by:

$$\Gamma^{\mu}_{\rho\sigma} = \frac{1}{2} g^{\mu\nu}(\partial_\rho g_{\nu\sigma} + \partial_\sigma g_{\nu\rho} - \partial_\nu g_{\rho\sigma}), \tag{1.5}$$

where we defined the operator $\partial_\rho = \partial/\partial_\rho$. Now we can now define the curvature tensor, also called Riemann tensor, which, as the name implies, describes the curvature of spacetime:

$$R^{\mu}_{\nu\rho\sigma} = \partial_\rho \Gamma^{\mu}_{\nu\sigma} - \partial_\sigma \Gamma^{\mu}_{\nu\rho} + \Gamma^{\mu}_{\rho\lambda}\Gamma^{\lambda}_{\nu\sigma} - \Gamma^{\mu}_{\sigma\lambda}\Gamma^{\lambda}_{\nu\rho}. \tag{1.6}$$

Furthermore, from the curvature tensor we define two additional objects, a tensor and a scalar. They are called Ricci tensor and Ricci scalar, respectively, and are given by:

$$R_{\mu\nu} = g^{\lambda\sigma} R_{\sigma\mu\lambda\nu}, \; R = g^{\mu\nu} R_{\mu\nu}. \tag{1.7}$$

The Ricci scalar, which is also called the scalar curvature, is the simplest curvature invariant of a manifold. It assigns a real number to each point of the manifold, which is determined by the intrinsic geometry of the manifold near that point.

Now in order to associate the presence of mass or energy with curvature we need to define GR's field equation. GR, as every modern theory, is a field theory which means that is governed by field equations. The field equations of GR are:

$$R_{\mu\nu} - \frac{1}{2} g_{\mu\nu} R = \frac{8\pi G}{c^4} T_{\mu\nu}, \tag{1.8}$$

where G is the Newton constant. On the right hand side of the field equations we have the tensor $T_{\mu\nu}$, which is called energy-momentum tensor. This tensor encapsulates all the information about any mass-energy distribution that exists in a given system. It is a purely mass dependent tensor that bears no information about the curvature of spacetime. On the left hand side of the field equations we have a combination of tensors that define a new tensor, also called Einstein tensor, which involves only curvature dependent objects. The equality between the two means that in the presence of mass or energy, i.e. a non-zero $T_{\mu\nu}$, the Einstein tensor has nonzero components. In other words, the presence of mass or energy forces spacetime to curve. There is the freedom of

adding a term that is proportional to the metric:

$$R_{\mu\nu} - \frac{1}{2}g_{\mu\nu}R + \Lambda g_{\mu\nu} = \frac{8\pi G}{c^4}T_{\mu\nu}. \tag{1.9}$$

where Λ is called cosmological constant and describes a constant energy density. This new term can also be moved to the right hand side of the field equations and be considered as an energy density of vacuum space (see more in Sec. 1.3). Energy conservation in GR is expressed with the equation:

$$\nabla_\mu T^\mu_\nu = \partial_\mu T^\mu_\nu + \Gamma^\mu_{\mu\lambda}T^\lambda_\nu - \Gamma^\lambda_{\nu\mu}T^\mu_\lambda = 0, \tag{1.10}$$

where ∇_μ is called the covariant derivative.

There is a very important point to make here. While it is true that the presence of mass or energy always means that spacetime will be curved, the opposite statement does not always stand. To understand this, it is better to rewrite the field equations in an equivalent form:

$$R_{\mu\nu} = \frac{8\pi G}{c^4}(T_{\mu\nu} - \frac{1}{2}g_{\mu\nu}T), \tag{1.11}$$

where $T = g^{\mu\nu}T_{\mu\nu}$. In the case of an empty spacetime we have $T_{\mu\nu} = 0$ which, from the equation above, implies that $R_{\mu\nu} = 0$. However, this does not imply that the Riemann tensor will have all of its elements equal to zero, .i.e., $R^\mu_{\nu\rho\sigma} = 0$. There are special solutions of the field equations for which spacetime is empty but not flat.

1.2 Fundamental Concepts of Gravitational Waves

Gravitational waves (GW) are special solutions of GR field equations. They are ripples in the fabric of spacetime that propagate and affect the geodesics of observers. The simplest case to study GW is to consider that they have small amplitude. That way the field equations of GR can be expanded around the Minkowski spacetime:

$$g_{\mu\nu} = \eta_{\mu\nu} + h_{\mu\nu},\ |h_{\mu\nu}| << 1, \tag{1.12}$$

where $\eta_{\mu\nu}$ is the Minkowski spacetime and $h_{\mu\nu}$ a small perturbation. Substituting this expression into the field equations and keeping only terms up to first order in h we find the linearized GR field equations:

$$\Box\bar{h}_{\mu\nu} + \eta_{\mu\nu}\partial^{\rho}\partial^{\sigma}\bar{h}_{\rho\sigma} - \partial^{\rho}\partial_{\nu}\bar{h}_{\mu\rho} - \partial^{\rho}\partial_{\mu}\bar{h}_{\nu\rho} = -\frac{16\pi G}{c^4}T_{\mu\nu}, \tag{1.13}$$

where we have defined the operator $\Box = \eta_{\mu\nu}\partial^{\mu}\partial^{\nu}$ and we have used the tensor:

$$\bar{h}_{\mu\nu} = h_{\mu\nu} - \frac{1}{2}\eta_{\mu\nu}h,\ h = \eta^{\mu\nu}h_{\mu\nu}. \tag{1.14}$$

The linearized equations can be further simplified by choosing a proper gauge. We can always transform from a coordinate system x_{μ} to another $x^{'}_{\mu}$ as:

$$x^{'\mu} = x^{\mu} + \xi^{\mu}(x). \tag{1.15}$$

If the derivatives $\partial_{\nu}\xi_{\mu}$ are smaller, or of the same order as $h_{\mu\nu}$, then the condition $|h_{\mu\nu}|<< 1$ is not spoiled. Under this coordinate transformation, we have to lowest order:

$$\bar{h}^{'}_{\mu\nu}(x^{'}) = \bar{h}_{\mu\nu}(x) - (\partial_{\nu}\xi_{\mu} + \partial_{\mu}\xi_{\nu} - \eta_{\mu\nu}\partial_{\rho}\xi^{\rho}) \tag{1.16}$$

By choosing our coordinate system appropriately (fixing the ξ's), we can find one that the additional condition $\partial^{\nu}\bar{h}_{\mu\nu} = 0$ is satisfied. In this coordinate system, we can write the linearized field equations as:

$$\Box\bar{h}_{\mu\nu} = -\frac{16\pi G}{c^4}T_{\mu\nu}. \tag{1.17}$$

Outside of the GW source, where $T_{\mu\nu} = 0$, this equation is written simply as $\Box\bar{h}_{\mu\nu} = 0$. This allows for an additional coordinates selection and simplification of the form of $\bar{h}$. We have the freedom of transforming our coordinates $x^{''\mu} = x^{'\mu} + \epsilon^{\mu}$. By selecting ϵ such that the condition $\Box\epsilon^{\mu} = 0$ is satisfied, then we can define:

$$\epsilon_{\mu\nu} = \partial_{\mu}\epsilon_{\nu} + \partial_{\nu}\epsilon_{\mu} - \eta_{\mu\nu}\partial_{\rho}\epsilon^{\rho}, \tag{1.18}$$

which also satisfies $\Box\epsilon^{\mu\nu} = 0$. The elements of ϵ^{μ} are arbitrary and only need to satisfy the vanishing of the box operator. This means that we have the freedom of choosing three out of the four elements and impose three conditions on the $\bar{h}$ tensor. The most usual and handy conditions to impose are the following:

$$\bar{h}^{0\mu} = 0,\ \bar{h}^{i}_{i} = 0,\ \partial^{j}\bar{h}_{ij} = 0. \tag{1.19}$$

This gauge is called transverse-traceless (TT) gauge. In this gauge $\bar{h}$ takes a simpler form:

$$h^{TT}_{\mu\nu} = \begin{pmatrix} 0 & 0 & 0 & 0 \\ 0 & h_{+} & h_{\times} & 0 \\ 0 & h_{\times} & -h_{+} & 0 \\ 0 & 0 & 0 & 0 \end{pmatrix}, \tag{1.20}$$

where we have defined the non zero elements of $\bar{h}_{\mu\nu}$ as $h_{+}, h_{\times}$, called h-plus and h-cross, respectively. In the TT gauge the GW have two polarizations that are given by $h_{+}, h_{\times}$.

The TT gauge is a general coordinate transformation that can be used also in the case of a non-vanishing energy-momentum tensor (see Sec. 1.2 of [1]). In the most general case of non-vanishing $T_{\mu\nu}$ and at distances r much larger than the typical radius of the source, the solutions of Eq. 1.17 in the TT gauge are:

$$h^{TT}_{ij} = \frac{1}{r}\frac{2G}{\pi c^{5}}\Lambda_{ij,kl}(\hat{n})\int d\omega T_{kl}e^{-i\omega(t-r)/c}, \tag{1.21}$$

where we have expanded over distance and have taken the Fourier transformation (for details see Sec. 3.1 of [1]). Here, Λ_{ij} are the tensors that transform into the TT gauge, $\hat{n}$ is the direction of propagation of the GW, r is the distance from the source and ω is the 0^{th} component of the wave-vector $k^{\mu} = (\omega c, k^{i})$ and comes from the Fourier transform.

The most promising sources of GW are coalescences of binary systems consisting of compact objects, like black holes or neutron stars. For this type of coalescences, and assuming that the sources move with non-relativistic speeds, we can expand Eq. 1.21

for small velocities and by keeping only the leading term we find:

$$\begin{aligned} h_+(t) &= \frac{1}{r}\left(\frac{GM_c}{c^2}\right)^{5/4}\left(\frac{5}{cT}\right)^{1/4}\frac{1+\cos^2\iota}{2}\cos[\Phi(T)], \\ h_\times(t) &= \frac{1}{r}\left(\frac{GM_c}{c^2}\right)^{5/4}\left(\frac{5}{cT}\right)^{1/4}\cos\iota\sin[\Phi(T)], \end{aligned} \tag{1.22}$$

where $T = t_{coal} - t$ and t_{coal} is the time of coalescence of the binary and M_c is a quantity called chirp mass:

$$M_c = \frac{(m_1 m_2)^{3/5}}{(m_1 + m_1)^{1/5}}, \tag{1.23}$$

where $m_1,\ m_2$ the masses of the objects.

The parameter ι defines the inclination of the binary plane with respect to the axis along the line of sight of the observer. For orbits that are edge-on, $\iota = \pi/2$ and the function $h_\times$ vanishes. In this case the GW are linearly polarized. On the contrary, if $\iota = 0$ h_+ is a cosine function whereas $h_\times$ is a sine function with the same amplitude as h_+. Consequently, in this case the GW are circularly polarized. The function Φ is the phase of the GW, given by:

$$\Phi(T) = -2\left(\frac{5GM_c}{c^3}\right)^{-5/8} T^{5/8} + \Phi_0, \tag{1.24}$$

where Φ_0 is the phase at the time of coalescence t_{coal}. From Eqs. 1.22, we can see that the chirp mass affects both the amplitude and the phase of GW. A representation of h_+ and $h_\times$ for some arbitrary choice of the parameters can be seen in Fig. 1.1.

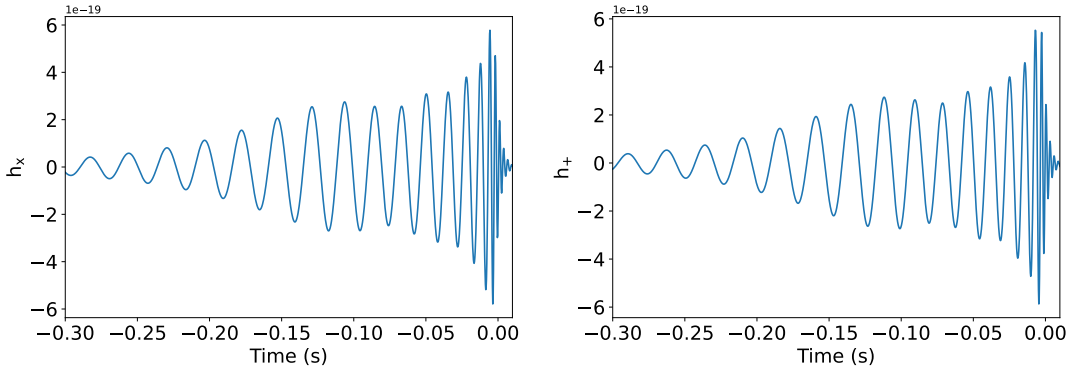

Figure 1.1: Representation of the $h_\times$ and h_+ as functions of time. The plot was created with $m_1 = m_2 = 25$ solar masses.

From Eqs. 1.22 it can be seen that both h_+ and $h_\times$ are inversely proportional to the distance from the source. As we will see in the next chapters, this will be very important for cosmological analysis.

1.3 Standard Model of Cosmology

In the last section we considered a flat metric as a background where fluctuations propagate. However, the Universe is expanding in reality. Since sources of GW are at cosmological distances, we need to take into account the cosmological expansion and the effect that it will have on h_+ and $h_\times$. Before we explore the effects of the cosmological expansion on $h_+,\ h_\times$ we need to understand the dynamics of an expanding spacetime.

The Cosmological Principle is the hypothesis that seems to be consistent with observations. According to it, the Universe is spatially homogenous and isotropic at very large scales, but evolves with time. In the framework of GR, this translates to a metric of the form:

$$ds^2 = -c^2dt^2 + R^2(t)d\sigma^2, \tag{1.25}$$

where $R(t)$ is known as the scale factor, and $d\sigma^2$ is the 3-dimensional metric:

$$d\sigma^2 = \gamma_{ij}dx^i dx^j, \tag{1.26}$$

where γ_{ij} are the elements of spatial metric. The 3-dimensional metric of a spatially homogenous space can be written as [2]:

$$d\sigma^2 = e^{2\beta(\hat{r})}d\hat{r}^2 + \hat{r}^2 d\Omega^2, \tag{1.27}$$

where $\hat{r}$ is the radial coordinate and $d\Omega^2$ is the metric on the 2-dimensional sphere $d\Omega^2 = d\theta^2 + \sin^2\theta d\phi^2$. Calculating the Riemann tensor [2] one can show that:

$$\beta(\hat{r}) = -\frac{1}{2}\ln(1 - \kappa\hat{r}^2), \tag{1.28}$$

where κ is a constant. Now the 3-dimensional metric can be written as:

$$d\sigma^2 = \frac{1}{1-\kappa\hat{r}^2}d\hat{r}^2 + \hat{r}^2 d\Omega^2, \tag{1.29}$$

In fact we can normalize $\kappa = \hat{\kappa}|\kappa|$, where $\hat{\kappa}$ can take the following values:

$$\hat{\kappa} = [-1, 0, 1]. \tag{1.30}$$

The value of $\hat{\kappa}$ sets the type of spacetime through its connection to the 3-dimensional curvature. The case $\hat{\kappa} = -1$ is called open, the case $\hat{\kappa} = 0$ is called flat and the case $\hat{\kappa} = 1$ is called closed. A useful coordinate transformation to better understand the physical interpretation of the above cases is the following:

$$d\chi = \frac{d\tilde{r}/\sqrt{|\kappa|}}{\sqrt{1-\hat{\kappa}\tilde{r}^2}}, \tag{1.31}$$

where $\tilde{r} = \sqrt{|\kappa|}\hat{r}$. With this, the 3-dimensional metric is written as:

$$d\sigma^2 = d\chi^2 + S_\kappa^2(\chi)d\Omega^2, \tag{1.32}$$

where:

$$S_\kappa(\chi) = \begin{cases} \dfrac{\sin(\sqrt{|\kappa|}\chi)}{\sqrt{|\kappa|}} & \text{, for } \hat{\kappa} = +1 \\ \chi & \text{, for } \hat{\kappa} = 0 \\ \dfrac{\sinh(\sqrt{|\kappa|}\chi)}{\sqrt{|\kappa|}} & \text{, for } \hat{\kappa} = -1 \end{cases} . \tag{1.33}$$

For example, for $\hat{\kappa} = 0$ we have:

$$d\sigma^2 = d\chi^2 + \chi^2 d\Omega^2 = dx^2 + dy^2 + dz^2, \tag{1.34}$$

which is simply the flat Euclidean space. For $\hat{\kappa} = +1$ we get the metric of a 3-dimensional sphere, whereas for $\hat{\kappa} = -1$ the 3-dimensional metric is a space with negative curvature. Such a space extends forever, which is the reason why it is called open.

Hence, imposing the Cosmological Principle led to a 4-dimensional metric of the

form:

$$ds^2 = -c^2dt^2 + R^2(t)\left[\frac{d\hat{r}^2}{1-\kappa\hat{r}^2} + \hat{r}^2 d\Omega^2\right], \tag{1.35}$$

which is called Friedmann–Lemaître–Robertson–Walker (FLRW) metric. By normalizing with the value of the scale factor at beginning of time $R_0 = R(t=0)$ we get the final form of the metric:

$$ds^2 = -c^2dt^2 + a^2(t)\left[\frac{dr^2}{1-kr^2} + r^2 d\Omega^2\right], \tag{1.36}$$

where $a(t) = R(t)/R_0,\ r = R_0\hat{r},\ k = \kappa/R_0^2$. The coordinates that appear in the FLRW metric are called comoving coordinates. This comes from the fact that an observer initially at rest in this frame will remain at fixed coordinate values despite the expansion of the spacetime.

To be able to infer the scale factor we need to use the Einstein field equations 1.8. Therefore, we need the energy-momentum distribution of the Universe $T_{\mu\nu}$. The usual choice is a perfect fluid that is at rest in the comoving coordinates. In this case we have:

$$T_{00} = \rho c^2,\ T_{0i} = 0,\ T_{ij} = g_{ij}p, \tag{1.37}$$

where ρ is the mass density of the fluid and p is its pressure. By assuming an equation of state that is given by:

$$p = \omega\rho c^2, \tag{1.38}$$

(where ω is a constant) and using the 0^{th} component of the energy conservation 1.10 we find:

$$\frac{\dot{\rho}}{\rho} = -3(1+\omega)\frac{\dot{a}}{a}, \tag{1.39}$$

where the dot represents the derivative with respect to time. Integrating this equation we get:

$$\rho \propto a^{-3(1+\omega)}. \tag{1.40}$$

The value of ω gives the type of cosmological fluid. One of the most popular choices is $\omega = 0$ which gives $\rho \propto a^{-3}$ and describes a set of collisionless and nonrelativistic particles

which have zero pressure. This is applicable to common matter, like stars and galaxies, and a universe with an energy density mostly coming from this type of fluid is called matter-dominated. Another example is $\omega = 1/3$ which gives $\rho \propto a^{-4}$ and describes a set of relativistic particle and the universe in this case is called radiation-dominated. Another interesting case is $\omega = -1$. Here $\rho \propto a^0$. This describes a universe with a constant in time vacuum energy, and is called vacuum-dominated. Using now the Einstein field equations 1.9 we find:

$$\begin{aligned} \left(\frac{\dot{a}}{a}\right)^2 &= \frac{8\pi G}{3}\rho - \frac{kc^2}{a^2} + \frac{\Lambda c^2}{3}, \\ \frac{\ddot{a}}{a} &= -\frac{4\pi G}{3}(\rho + \frac{3p}{c^2}) + \frac{\Lambda c^2}{3}. \end{aligned} \tag{1.41}$$

This set of equations are known as the Friedmann equations and the function $\dot{a}/a$ is called the Hubble function:

$$H(t) = \frac{\dot{a}}{a}. \tag{1.42}$$

The value of the Hubble function at the current epoch is called Hubble constant, $H_0 = H(t_0)$, where $t_0 = t_{today}$. Multiple experiments have given estimations of H_0, but their values disagree, many of which have a statistically significant disagreement outside of the 5σ credible intervals. This disagreement over the value of Hubble constant has led to the infamous H_0 tension [3, 4].

All the measurements indicate a value around 70 km s^{-1} Mpc^{-1}. However, estimations of H_0 seem to cluster around two different values. The early-time measurements, which are made using data from the early Universe, cluster around $H_0 =$ 67 km s^{-1} Mpc^{-1}, whereas those made using close by objects like stars, i.e., current epoch or late-time measurements, cluster around $H_0 = 73$ km s^{-1} Mpc^{-1}, as shown in Fig. 1.2.

The early-time measurements are made by analyzing the data of the cosmic microwave background (CMB). As we have seen, at a large scale the Universe is isotropic and homogenous. However, small deviations occurred during the early life of the Universe at small scales. At that time, the Universe was a hot dense plasma of matter and photons, and the photons couldn't escape from the matter because its density was large.

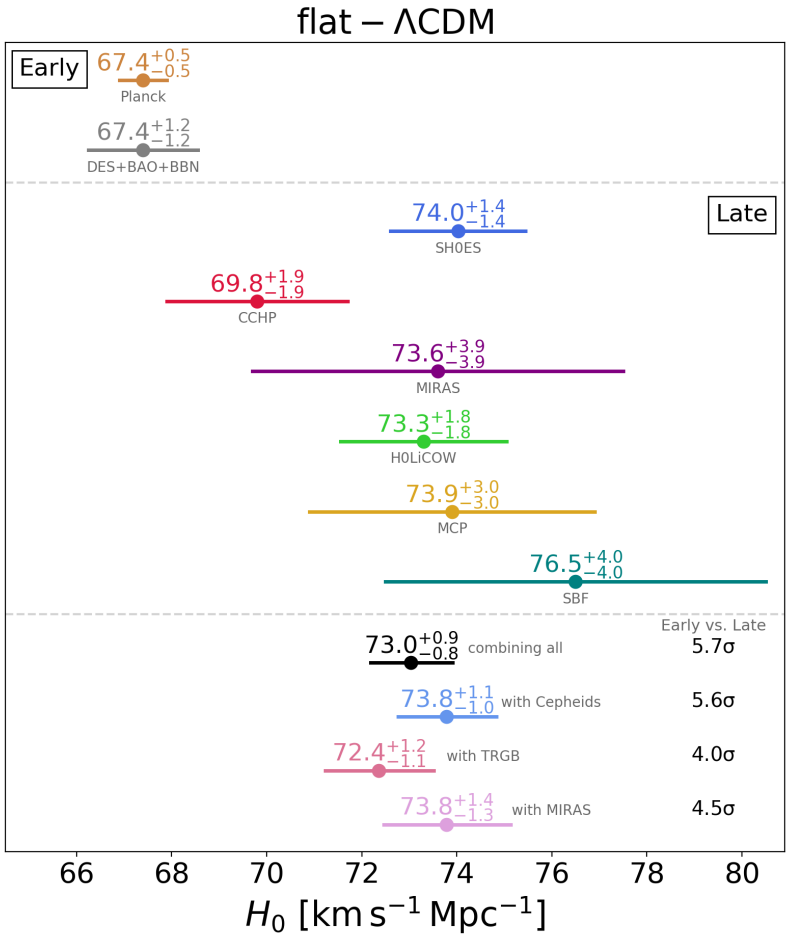

Figure 1.2: A summary of H_0 measurements. The tension over the value for late- vs early-time measurements can be seen. In the top panel of the plot one can find two measurements of H_0 using early-time data, along with their uncertainties. In the middle panel, various late-time measurements can be found. Finally, the last panel shows the H_0 values obtained by combining different late-time measurements and their statistical difference with respect to the Planck measurement. In the last panel the combined values from top to bottom are retrieved when: i) Combining all six measurements from the middle panel, ii) Combining the HOLICOW, SHOES, MCP and SBF measurements, iii) Combining the HOLICOW, CCHP, MCP and SBF measurements and iv) Combining the HOLICOW, MIRAS, MCP and SBF measurements. The plot was taken from Ref. [4].

Small perturbations in the plasma, that propagated as sound waves (also known as baryonic acoustic oscillations), created over- and under-densities in the plasma. As the Universe continued expanding, the density reached the point where the photons decoupled from the matter and escaped. Those photons is what we call CMB. The over- and under-densities at the plasma at the moment of the photon decoupling are imprinted

in the CMB. Studying the small differences in the temperature of the CMB across the sky can give an estimation of the H_0 value. This was done by the Planck collaboration in 2018, who measured $H_0 = 67.4 \ \pm 0.5$ km s^{-1} Mpc^{-1} [5].

On the other hand, late-time measurements are made by studying close-by objects or events, like for example type I supernovae. The physics behind those events is pretty well understood and their luminosities are well known. Their distances can be obtained from the light curves and then be calibrated using nearby Cepheid variable stars. This allows for an estimation of H_0. The Supernovae H_0 Equation of State (SHOES) of the Dark Energy (DES) collaboration produced such a measurement and estimated $H_0 = 74.0 \ \pm 1.4$ km s^{-1} Mpc^{-1} [6]. This result is in tension with the measurement made by the Planck collaboration to a level of 4σ.

As it is very clear from the discussion above, there is currently a tension on the value of H_0, however the nature of this is not known. It might indicate the need for new physics beyond the standard model of cosmology. However, there is no easy modification that does not create a different tension or disagreement with observations.

Another interesting quantity that we can define is the density parameter Ω. Assuming that a given type of fluid has an energy density ρ we can define the density parameter as:

$$\Omega = \frac{8\pi G}{3H^2}\rho = \frac{\rho}{\rho_{crit}}, \tag{1.43}$$

where we have defined the critical density as:

$$\rho_{crit} = \frac{3H^2}{8\pi G}. \tag{1.44}$$

It is called critical density because it allows to rewrite the first Friedmann (forgetting for now the vacuum energy term) equation as:

$$\Omega - 1 = \frac{kc^2}{H^2 a^2}. \tag{1.45}$$

It can easily be seen from this equation that the value of Ω is correlated with the sign of

the parameter k, which sets the type of the spacetime. We have:

$$\begin{aligned} \rho < \rho_{crit} &\Leftrightarrow \Omega < 1 \Leftrightarrow k < 0 \Leftrightarrow \textit{open} \\ \rho > \rho_{crit} &\Leftrightarrow \Omega > 1 \Leftrightarrow k > 0 \Leftrightarrow \textit{closed} \\ \rho = \rho_{crit} &\Leftrightarrow \Omega = 1 \Leftrightarrow k = 0 \Leftrightarrow \textit{flat} \end{aligned} \tag{1.46}$$

If we assume that the total energy and matter in the Universe consists of different perfect fluids, each component will have an energy density ρ_i which, in accordance with the above, we consider to be of the form:

$$\rho_i = \rho_{i,0} \left(\frac{a}{a_0} \right)^{-n_i}, \tag{1.47}$$

where the subscript i indicates the specific component, a_0 is the value of scale factor today $a_0 = a(t_0)$, ρ_{0i} is the value of energy density today $\rho_{0i} = \rho_i(t_0)$ and $\omega_i = \frac{1}{3} n_i - 1$. We can also define a fictitious energy density for the spatial curvature of the spacetime:

$$\rho_c = -\frac{3kc^2}{8\pi G a^2}. \tag{1.48}$$

With this we can summarize the various energy densities and the corresponding values as follows: i) for nonrelativistic particles, i.e. matter, we have $\omega_m = 0,\ n_m = 3$, ii) for relativistic particles we have $\omega_r = 1/3,\ n_r = 4$, iii) for curvature we have $\omega_c = -1/3,\ n_c = 2$, iv) for vacuum we have $\omega_\Lambda = -1,\ n_\Lambda = 0$. The first Friedmann equation can be written as:

$$H^2 = \frac{8\pi G}{3} \sum_i \rho_i, \tag{1.49}$$

where i runs over $i = \{m,\ r,\ c,\ \Lambda\}$. Notice that by dividing the equation above by H^2 we get:

$$\Omega_m + \Omega_r + \Omega_c + \Omega_\Lambda = 1, \tag{1.50}$$

where:

$$\begin{aligned}\Omega_{(m,r)} &= \frac{8\pi G}{3H^2}\rho_{(m,r)} = \frac{\rho_{(m,r)}}{\rho_{crit}},\\ \Omega_c &= -\frac{kc^2}{H^2a^2} = \frac{\rho_c}{\rho_{crit}},\\ \Omega_\Lambda &= \frac{\Lambda c^2}{3H^2} = \frac{\rho_\Lambda}{\rho_{crit}}, \rho_\Lambda = \frac{\Lambda c^2}{3H^2}.\end{aligned} \tag{1.51}$$

The functions above taken at the present time t_0 are:

$$\begin{aligned}\Omega_{(m,r),0} &= \frac{8\pi G}{3H_0^2}\rho_{(m,r),0},\\ \Omega_{c,0} &= -\frac{kc^2}{H_0^2a_0^2},\\ \Omega_{\Lambda,0} &= \frac{\Lambda c^2}{3H_0^2}.\end{aligned} \tag{1.52}$$

With these definitions we can rewrite Eq. 1.49 as:

$$E(t) = \frac{H}{H_0} = \sqrt{\Omega_{m,0}\left(\frac{a}{a_0}\right)^{-3} + \Omega_{r,0}\left(\frac{a}{a_0}\right)^{-4} + \Omega_{c,0}\left(\frac{a}{a_0}\right)^{-2} + \Omega_{\Lambda,0}}. \tag{1.53}$$

The above equation encapsules the evolution of a Universe with a matter density, a radiation density, curvature and the presence of a constant vacuum energy. A cosmological model with negligible contributions from curvature and radiation ($\Omega_{c,0} = \Omega_{r,0} = 0$) and $\Omega_{\Lambda,0}$ =constant is called flat Λ Cold Dark Matter (flat ΛCDM).

1.4 Gravitational Waves on an Expanding Background

We are now in a position of inferring the effect of the cosmological expansion on the GW. Going back to the metric of Eq. 1.36, assuming that two observers are at coordinates (r_1, θ, ϕ) and (r_2, θ, ϕ), respectively, and with zero velocities, their coordinate, or comoving, distance is $r = r_2 - r_1$. This distance will remain unchanged despite the expansion of the Universe, however it has no physical meaning. The spatial distance that has physical meaning is the spatial proper distance r_{prop} which is given by:

$$dr_{prop} = \sqrt{g_{ij}dx^i dx^j} = a(t)\frac{dr}{\sqrt{1-kr^2}} \Rightarrow r_{prop}(t) = a(t)\int_{r_1}^{r_2}\frac{dr}{\sqrt{1-kr^2}}. \tag{1.54}$$

To understand the effect of an expanding background in the GW propagation we imagine a source that lies at a comoving distance $r_{source} = r$ from an observer at $r_{obs} = 0$ and emits GW. Since GW travel at the speed of light, if the source emits a wavecrest at a time t_{emit} and the GW reach the observer at t_{obs}, then we have:

$$\int_{t_{emit}}^{t_{obs}} \frac{cdt}{a(t)} = \int_0^r \frac{dr}{\sqrt{1-kr^2}}. \tag{1.55}$$

For a second wavecrest emitted at $t_{emit} + \Delta t_{emit}$ and observed at $t_{obs} + \Delta t_{obs}$ we have a similar expression:

$$\int_{t_{emit}+\Delta t_{emit}}^{t_{obs}+\Delta t_{obs}} \frac{cdt}{a(t)} = \int_0^r \frac{dr}{\sqrt{1-kr^2}}. \tag{1.56}$$

Taking the difference of those two equations and keeping only the linear order in Δ_{emit} we find:

$$\Delta t_{obs} = \frac{a(t_{obs})}{a(t_{emit})} \Delta t_{emit}. \tag{1.57}$$

Looking at this equation, we understand that in an expanding universe there is a time dilation between time measured by the observer and time measured by the source. Here we define the redshift z of a source, which is given by:

$$1 + z(t_{emit}) = \frac{a(t_{obs})}{a(t_{emit})}. \tag{1.58}$$

The redhsift describes the time dilation between clocks of the source and of the observer. We can rewrite Eq. 1.57 as:

$$\Delta t_{obs} = (1+z)\Delta t_{emit}. \tag{1.59}$$

Consequently, we also have a difference between frequencies in the source frame and the frame of the observer:

$$f_{obs} = \frac{f_{emit}}{1+z}. \tag{1.60}$$

Since the energy is proportional to the frequency, the same equation stand for energies measured in the observer's frame and in the frame of the source. We say that energies are redshifted.

We can now define the luminosity distance of a source. The luminosity L of a source in its frame is given by:

$$L_{emit} = \frac{dE_{emit}}{dt_{emit}}. \tag{1.61}$$

In the case of a flat spacetime, i.e. no expansion and no redshift, the same luminosity would be measured by any observer in their frame. However, due to the expansion of spacetime we have:

$$L_{obs} = \frac{dE_{obs}}{dt_{obs}} = \frac{1}{(1+z)^2}\frac{dE_{emit}}{dt_{emit}}. \tag{1.62}$$

The energy flux over the area A is given by:

$$F = \frac{L}{A}. \tag{1.63}$$

The area of the sphere centered at the source at comoving distance χ and at time t_{obs} is given directly from the coefficient of $d\Omega^2$ in Eq. 1.32 (modulo the function $a(t)$ that multiplies the 3-dimentional metric of Eq. 1.32):

$$A = \int a^2(t_{obs}) S_\kappa^2(\chi) d\Omega^2 = 4\pi a^2(t_{obs}) S_k^2(\chi). \tag{1.64}$$

Combining everything together we have:

$$F_{obs} = \frac{L_{obs}}{4\pi a^2(t_{obs}) S_k^2(\chi)} = \frac{L_{emit}}{4\pi d_L^2}, \tag{1.65}$$

where we have defined the luminosity distance at a time $t_{obs} = t_0$ as:

$$d_L = (1+z) a(t_0) S_k(\chi). \tag{1.66}$$

We can express the comoving distance χ as:

$$\chi = \int \frac{cdt}{a} = \int \frac{cda}{a^2 H(a)} = \frac{c}{H_0}\int \frac{da}{a^2 E(a)} = \frac{c}{H_0}\int \frac{dz}{E(z)}, \tag{1.67}$$

where we have expressed everything as a function of redshift. The functions $E(z)$ of

Eq. 1.53 as a function of redshift is:

$$E(z) = \frac{H}{H_0} = \sqrt{\Omega_{m,0}\,(1+z)^3 + \Omega_{r,0}\,(1+z)^4 + \Omega_{c,0}\,(1+z)^2 + \Omega_{\Lambda,0}}. \tag{1.68}$$

We can now give the expression for the luminosity distance in the case of the three types of universes:

$$d_L = (1+z)a(t_0)\begin{cases} \dfrac{1}{\sqrt{|k|}}\sin\left[\dfrac{c\sqrt{|k|}}{H_0}\int E(z)^{-1}dz\right] & \text{, for } k>0 \\ \dfrac{c}{H_0}\int E(z)^{-1}dz & \text{, for } k=0 \\ \dfrac{1}{\sqrt{|k|}}\sinh\left[\dfrac{c\sqrt{|k|}}{H_0}\int E(z)^{-1}dz\right] & \text{, for } k<0 \end{cases} \tag{1.69}$$

The luminosity distance is a very important quantity since it can be measured and encapsules the history of the evolution of the Universe. Notice from the equations above that, if the luminosity distance to a source and its redshift are known, we can estimate cosmological parameters like H_0.

We have now at our disposal everything we need to find the effect of an expanding background on the GW. The generalization of the operator $\Box$ for a curved spacetime with metric $g_{\mu\nu}$ is:

$$\Box = \frac{1}{\sqrt{-g}}\partial_\mu(\sqrt{-g}g^{\mu\nu}\partial_\nu), \tag{1.70}$$

where g is the determinant of $g_{\mu\nu}$. The FLRW metric can be rewritten in a form:

$$ds^2 = a^2(\eta)[-c^2dt^2 + dr^2 + r^2d\Omega^2]. \tag{1.71}$$

The coordinate η is called conformal time. Following [1], we search for a function of a form $\phi(r,\eta) = \dfrac{1}{\eta}f(r,\eta)$ that satisfies:

$$\Box\phi = 0 \Rightarrow \partial_r^2 f - f'' - 2\frac{a'}{a}f' = 0, \tag{1.72}$$

where $'$ denotes the derivative with respect to the conformal time and $f' = (1/c)\partial_\eta f$.

Defining $g(r,\eta) = a(\eta)f(r,\eta)$ we get:

$$\partial_r^2 g - g^{''} - 2\frac{a^{''}}{a}g = 0. \tag{1.73}$$

The solutions of this equation are of the form:

$$g(\eta, r) \propto e^{\pm i\omega(\eta - r/c)} \tag{1.74}$$

as long as $\omega^2 \gg 1/\eta^2$. In this case the last term of Eq. 1.73 drops out and we are left with a wave equation. In conclusion, any function of form $g(\eta - r/c)$ is a solution of Eq. 1.73, as long as its Fourier transform has frequencies that satisfy $\omega^2 \gg 1/\eta^2$. Thus, normalizing our solution with the present time t_0 we found that:

$$\phi(t, r) = g(t - r/c) \tag{1.75}$$

is a solution for a wave propagating on an FLRW spacetime. The only difference with the wave propagating in an nonexpanding background is the term $a(t_0)$.

Following the same logic, we understand that Eq. 1.22 expressed on an FLRW spacetime will change r to $ra(t_0)$ in the denominator. However, as we have seen in this chapter, frequencies also change. Therefore, the frequencies of the GW will get redshifted from the time dilation such that $f_{GW,obs} = f_{GW,source}/(1+z)$, where z is the redhsift of the GW source. The final expressions for $h_+,\ h_\times$ of GW produced from a binary coalescence and propagating through FLRW spacetime are:

$$\begin{aligned} h_+(t) &= \frac{4}{d_L}\left(\frac{GM_{cz}}{c^2}\right)^{5/3}\left(\frac{\pi f_{GW,obs}}{c}\right)^{2/3}\frac{1+\cos^2\iota}{2}\cos[\Phi(t_0)], \\ h_\times(t) &= \frac{4}{d_L}\left(\frac{GM_{cz}}{c^2}\right)^{5/3}\left(\frac{\pi f_{GW,obs}}{c}\right)^{2/3}\cos\iota\sin[\Phi(t_0)], \end{aligned} \tag{1.76}$$

where:

$$\Phi(t_0) = -2\left(\frac{5GM_{cz}}{c^3}\right)^{-5/8} t_0^{5/8} + \Phi_0, \tag{1.77}$$

with the redshifted chirp mass M_{cz} given by:

$$M_{cz} = (1+z)M_c. \tag{1.78}$$

We can absorb the redshift contribution of the chirp in the masses of the objects instead:

$$M_{cz}(m_1^s, m_2^s) = (1+z)M_c(m_1^s, m_2^s) = M_c(m_1^d, m_2^d), \tag{1.79}$$

where m_1^s, m_2^s are the masses in the frame of the source, or source frame masses, and m_1^d, m_2^d are the masses in the frame of the detector, or redshifted masses, which are given by:

$$\begin{aligned} m_1^d &= (1+z)m_1^s, \\ m_2^d &= (1+z)m_2^s. \end{aligned} \tag{1.80}$$

From Eq. 1.76 it can be seen that both h_+ and $h_\times$ are inversely proportional to the luminosity distance of the binary. It is embedded into the GW signal and can be directly evaluated by analysis of the GW data. Knowing the luminosity distance is very important for cosmology as it allows a unique method for the estimation of cosmological parameters, like H_0.

1.5 Modified Gravitational Waves Propagation

GW are ideal for cosmological parameters measurements since the luminosity distance is directly embedded into the signal. However, they also allow testing GR at cosmological scales [7, 8]. The propagation of GW in an FLRW is described by Eq. 1.73. In many modified GR theories there is an additional term that arises in the propagation equation, called friction term $\delta(\eta)$, which modifies the propagation of GW and allows for an additional energy dissipation as the GW propagate.

Working in the Fourier space, the modified propagation of GW can be written as [9]:

$$h_A^{''} + 2\frac{a^{'}}{a}\left[1 - \delta(\eta)\right] h_A^{'} + k^2 c^2 h_A = 0, \tag{1.81}$$

where k is the four-dimensional wave vector and $h_A = h_A(\eta, k)$ are the GW polarizations $A = \{+, x\}$. Notice here that when $\delta(\eta) = 0$ we get the propagation equation of GR. The term $H(\eta) = \dfrac{a^{'}}{a}$ is the Hubble function expressed as a function of the conformal time $\eta = \int dt/a(t)$. By defining $\dfrac{\tilde{a}^{'}}{\tilde{a}} = H(\eta)\left[1 - \delta(\eta)\right]$ we get a similar expression as that of GR. However now, as GW propagate over cosmological distances, the amplitude falls off as $1/\tilde{a}$ instead of $1/a$, which is the GR result. This means that the luminosity distances travelled by photons and GW are going to be different. Denoting the luminosity distance travelled by photons as d_L^{EM} and the one travelled by GW as d_L^{GW} we have:

$$d_L^{GW}(z) = d_L^{EM}(z) e^{-\int_0^z [\delta(z)/(1+z)]dz}. \tag{1.82}$$

The exact functional form of the friction term depends on the modified theory of GR. In some models of a running Planck mass with redshift, the friction term is parametrized as [10]:

$$\delta(z) = -\frac{c_M}{2}\frac{\Omega_\Lambda(z)}{\Omega_{\Lambda,0}} \tag{1.83}$$

where c_M is a constant. This gravity model modifies GR at late times: the friction term is proportional to the dark energy parameter Ω_Λ, which is dominant at present times. Assuming a flat universe and neglecting the density of radiation we get:

$$d_L^{GW}(z) = d_L^{EM}(z) \exp\left[\frac{c_M}{2\Omega_{\Lambda,0}} \ln\left(\frac{1+z}{\left[\Omega_m(1+z)^3 + \Omega_{\Lambda,0}\right]^{1/3}}\right)\right] \tag{1.84}$$

The Ξ_0 parametrization [11] is also an interesting choice of luminosity distance modification. Scalar-tensor theories describe the presence of a scalar field in GR. These theories are nowadays categorized into the Horndeski and beyond Horndeski, as well as DHOST classes [12, 13, 14, 15]. It was shown that in these cases the GW luminosity distance is given by:

$$d_L^{GW}(z) = d_L^{EM}(z)\left(\Xi_0 + \frac{1-\Xi_0}{(1+z)^n}\right), \tag{1.85}$$

where Ξ_0 and n are constants. At low redshifts the luminosity distances of photons and GW coincide. On the contrary, at very large redshifts we have $d_L^{GW}(z) = d_L^{EM}(z)\Xi_0$. While the above relation is phenomenological, the parameters Ξ_0 and n can generally be

related to a combination of free parameters of the modified GR theory (see Table 1 of [16]).

Another interesting parametrization is to consider extra spacetime dimensions[17]. GR is very successful at small scales like the solar system. If a theory beyond GR considers extra dimensions, like DGP gravity [18] and quantum gravity models[19], it needs to screen the extra effects at small scales. The modified GW luminosity distance in the case of extra dimensions is given by[20]:

$$d_L^{GW}(z) = d_L^{EM}(z)\left[1 + \left(\frac{d_L^{EM}(z)}{(1+z)R_c}\right)^n\right]^{(D-4)/2n}, \tag{1.86}$$

where D is the number of spacetime dimensions ($D = 4$ for GR). The effects of the extra dimensions are screened below the scale R_c. The parameter n controls the stiffness of the transition. In cases where GW probe scales much larger than the screening scale, $R_c \ll d_L^{EM}$, we have:

$$d_L^{GW}(z) = d_L^{EM}(z)\left(\frac{d_L^{EM}(z)}{R_c}\right)^{(D-4)/2}(1+z)^{(4-D)/2}. \tag{1.87}$$

Chapter 2

Detection of Gravitational Waves

In the previous chapter we saw that GW are propagating perturbations of the spacetime geometry that change the physical trajectories of observers. Due to the weak nature of gravity and the fact that GW sources are at cosmological distances from Earth, the GW that arrive to Earth are very hard to detect. Consequently, in order for a detector to be able to detect GW, it needs to be very sensitive to the small spacetime deviations that the GW cause. One of the proposed solutions to tackle this problem, which actually was created and led to the first GW detection, is Fabry-Pérot interferometers. In this chapter we will describe the basic concepts of a Fabry-Pérot interferometer, introduce the LIGO-Virgo detectors, and noise sources that couple into the data and make it harder to distinguish real GW signals.

2.1 Interaction of Gravitational Waves With Test Masses

To understand what an interferometer is, how it works and why it is able to detect GW, we need to first study the effect that GW have on test masses. As we have seen, observers or test masses in a given spacetime with metric $g_{\mu\nu}$ follow geodesics that are given from Eq. 1.4. Test masses follow time-like curves for which $ds^2 < 0$, therefore we can define the proper time τ from:

$$c^2 d\tau^2 = -ds^2 = -g_{\mu\nu} dx^\mu dx^\nu. \tag{2.1}$$

The physical interpretation of proper time is that it gives the time measured by a clock carried along this trajectory. We can use τ to parametrize the trajectory in this case and write the geodesic equation as:

$$\frac{d^2x^\mu}{d\tau^2} + \Gamma^\mu_{\rho\sigma}\frac{dx^\rho}{d\tau}\frac{dx^\sigma}{d\tau} = 0. \tag{2.2}$$

Now consider two nearby test masses, following two geodesics, one parametrized by $x^\mu(\tau)$ and the other by $x^\mu(\tau)+\xi^\mu(\tau)$. If $|\xi^\mu|$ is much smaller than the typical variational scale of the gravitational field, taking the difference between the geodesic equations of the two trajectories and keeping only terms up to first order in ξ^μ, we find the equation of the geodesic deviation:

$$\frac{d^2\xi^\mu}{d\tau^2} + 2\Gamma^\mu_{\rho\sigma}\frac{dx^\rho}{d\tau}\frac{d\xi^\sigma}{d\tau} + \xi^\nu\partial_\nu\Gamma^\mu_{\rho\sigma}\frac{dx^\rho}{d\tau}\frac{dx^\sigma}{d\tau} = 0. \tag{2.3}$$

Considering now an earthbound detector, we can use the equation of geodesic deviation to infer the effect of GW. Assuming that the detector moves non relativistically and expanding around a spacetime point P, Eq. 2.3 gives:

$$\frac{d^2\xi^i}{d\tau^2} + \xi^\nu\partial_\nu\Gamma^i_{00}\left(\frac{dx^0}{d\tau}\right)^2 = 0. \tag{2.4}$$

Following [1] Chapter 1.3.3 this can be further simplified to:

$$\frac{d^2\xi^i}{d\tau^2} = -R^i_{0j0}\xi^j\left(\frac{dx^0}{d\tau}\right)^2. \tag{2.5}$$

In the case of GW passing, the Riemann tensor R^i_{0j0} in the above equation is already of first order in h. This means that we can neglect higher order terms and write $\tau = t$ and $dx^0/d\tau = c$. Then the equation becomes:

$$\ddot{\xi}^i = -c^2R^i_{0j0}\xi^j, \tag{2.6}$$

where again the dot denotes the derivative with respect to the coordinate time t. Next we need to calculate the Riemann tensor. In the linearized theory this is invariant, which

means that we can calculate it in any coordinate system that we want. We are going to choose the TT frame, in which one finds:

$$R^i_{0j0} = -\frac{1}{2c^2}\ddot{h}^{TT}_{ij}, \tag{2.7}$$

and finally the geodesic deviation equation is written as:

$$\ddot{\xi}^i = \frac{1}{2}\ddot{h}^{TT}_{ij}\xi^j. \tag{2.8}$$

Now that we have found the equation of geodesic deviation for nearby test masses in the event of GW passing, we can calculate the actual effect of the GW on them. We consider GW that propagate along the z axis and a ring of test masses in the (x, y) plane. The components of h^{TT} can be read from Eq. 1.20. For GW propagating towards the z axis the h^{TT}_{zi} components are zero, which, by looking at the geodesic deviation equation, means that a test particle initially at $z = 0$, will remain at $z = 0$ after the passage of the wave and the displacement will be confined to the (x, y) plane.

To better understand the effect of GW on the ring of test masses we will consider the simplest solution of Eq. 1.17 in empty space, which is that of a plane wave with frequency $f_{GW} = \frac{\omega_{GW}}{2\pi}$ and only the plus polarization. By choosing the origin of time so that $h^{TT}_{ab} = 0$ at $t = 0$, we have:

$$h^{TT}_{ab} = h_+ \sin\omega_{GW} t \begin{pmatrix} 1 & 0 \\ 0 & -1 \end{pmatrix}, \tag{2.9}$$

where $\omega_{GW} = 2\pi f_{GW}$ and a, b are the indices in the (x, y) plane. We write $\xi_a(t) = (x_0 + \delta x(t), y_0 + \delta y(t))$, where x_0, y_0 are the unperturbed positions and $\delta x(t), \delta y(t)$ are the displacements produced by the GW. Then by keeping only terms at first order in h, integrating Eq. 2.8 gives:

$$\begin{aligned} \delta x &= -\frac{h_+}{2} x_0 \omega^2_{GW} \sin\omega_{GW} t, \\ \delta y &= \frac{h_+}{2} x_0 \omega^2_{GW} \sin\omega_{GW} t. \end{aligned} \tag{2.10}$$

The deformations that such GW causes to the ring of test masses can be seen in Fig. 2.1. In the same plot the deformation caused by a wave with only the cross polarization is also depicted. As it is illustrated in the figure, the passing of GW causes distances between test masses to change.

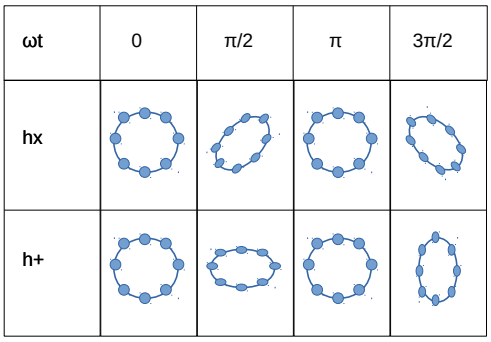

Figure 2.1: The effect of the two polarizations of a plane gravitational wave for different times.

Consider now a wave with both h_+ and $h_\times$ that propagates along the $z^{'}$ axis in a coordinate system $(x^{'}, y^{'}, z^{'})$. In this case we have:

$$h_{ij}^{'TT} = \begin{pmatrix} h_+ & h_\times & 0 \\ h_\times & -h_+ & 0 \\ 0 & 0 & 0 \end{pmatrix}. \tag{2.11}$$

Assume now that we have two test masses in a coordinate system (x, y, z), with coordinates $\xi_x = (L, 0)$ and $\xi_y = (0, L)$, respectively. The geodesic deviation of the two test masses along the x, y axes are given by:

$$\ddot{\xi}_x = \frac{1}{2}\ddot{h}_{xx}L, \;\; \ddot{\xi}_y = \frac{1}{2}\ddot{h}_{yy}L. \tag{2.12}$$

The polarizations h_+ and $h_\times$ are defined in the $(x^{'}, y^{'}, z^{'})$. In order to find the effect that GW have on the test masses in the (x, y, z) we need to define the rotated tensor

h^{TT}:

$$h_{ij}^{TT} = R_{ik}R_{jl}h_{kl}^{'TT}, \tag{2.13}$$

where R_{ij} is the rotation tensor. The first rotation is by an angle θ around the $y^{'}$ axis and the second by an angle ϕ around the $z^{'}$ axis. Performing the above calculations we find:

$$\begin{aligned} h_{xx} &= h_{+}(\cos^2\theta\cos^2\phi - \sin^2\phi) + 2h_{\times}\cos\theta\sin\phi\cos\phi, \\ h_{yy} &= h_{+}(\cos^2\theta\sin^2\phi - \cos^2\phi) - 2h_{\times}\cos\theta\sin\phi\cos\phi. \end{aligned} \tag{2.14}$$

The relative distance difference between the two test masses is given by:

$$\frac{1}{2}(h_{xx} - h_{yy}) = \frac{1}{2}h_{+}(1+\cos^2\theta)\cos 2\phi + h_{\times}\cos\theta\sin 2\phi). \tag{2.15}$$

Therefore, we can define two functions that depend only on the rotation angles, which are called antenna factors:

$$\begin{aligned} F_{+}(\theta,\phi) &= \frac{1}{2}(1+\cos^2\theta)\cos 2\phi, \\ F_{\times}(\theta,\phi) &= \cos\theta\sin 2\phi \end{aligned} \tag{2.16}$$

From the equations above we see that there exist special directions of incoming GW, with respect to the coordinate system of the test masses, that leave the relative distance between the test masses unaffected. In the next section, we are going to see that this practically means that our detectors have blind spots over the sky.

2.2 Fabry-Perot Interferometers

To be able to detect GW passing from Earth we need a detector that can measure distances with high accuracy. For this we can use Fabry-Pérot interferometers which are based on the design of a Michelson interferometer. A Michelson interferometer is an instrument able to measure changes in the travel time of light extremely accurately. It consists of a monochromatic light source sending light to a beam splitter which splits the beam into two beams with equal amplitudes travelling in orthogonal directions,

called arms. At the end of each arm there are mirrors that reflect the light back into the beam splitter, where they recombine. A part of the recombined beam travels to a photodetector, while a part goes back into the laser (see Fig. 2.2).

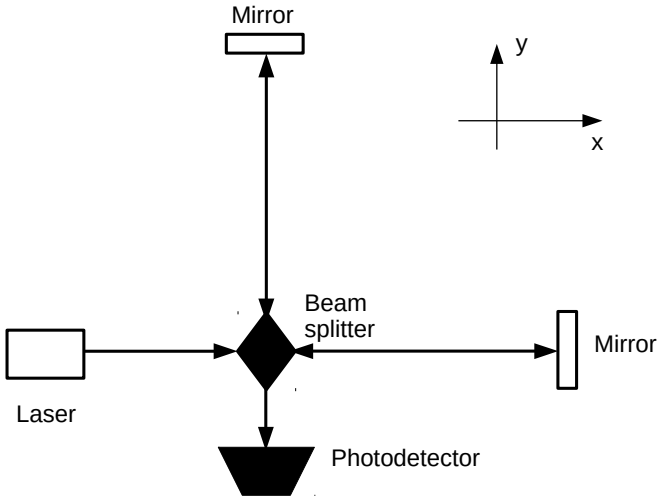

Figure 2.2: Illustration of a Michelson interferometer.

Following what was presented in the previous section, we consider the mirrors at the end of each arm as test masses positioned at the coordinates $(L_x, 0)$ and $(0, L_y)$, where L_x, L_y are the lengths of the arms. Denoting by ω_L the frequency of the laser, and by k_L its wave number, the power E_{out} measured by the photodetector is proportional to (see Section 9.1 of Ref. [1]):

$$|E_{out}|^2 = E_0^2 \sin^2[k_L(L_y - L_x)]. \tag{2.17}$$

Consequently, any change in the lengths of the arms results in a variation of the power measured by the photodetector. This is the basic principle that allows us to detect GW, since as we have seen in the previous section, GW do cause changes in distances between test masses. We consider now two photons that travel along the two arms while a plane wave passes. For them the times $t_{(x,y)}$ at which they will return to the beam splitter,

assuming that they leave from it at t_0, are given by (see Section 9.1.1 of Ref. [1]):

$$t_{(x,y)} - t_0 = \frac{2L_{(x,y)}}{c} \pm \frac{L_{(x,y)}}{c} h(t_0 + L_{(x,y)}/c) \frac{\sin(\omega_{GW} L_{(x,y)}/c)}{\omega_{GW} L_{(x,y)}/c}. \tag{2.18}$$

In practise, we are interested in photons that recombine at the beam splitter at a fixed time $t_{(x)} = t_{(y)} = t$ but originate from different times $t_0^{(x)}$ and $t_0^{(y)}$, respectively. By keeping as always only terms that are at first order in h we can rewrite the equations above as:

$$t_0^{(x,y)} = t - \frac{2L_{(x,y)}}{c} \mp \frac{L_{(x,y)}}{c} h(t - L_{(x,y)}/c) \frac{\sin(\omega_{GW} L_{(x,y)}/c)}{\omega_{GW} L_{(x,y)}/c}. \tag{2.19}$$

The arm distances L_x, L_y are made as similar as possible. We can take into account small deviations by defining $L = (L_x + L_y)/2$ and writing $2L_x = 2L + (L_x - L_y), 2L_y = 2L - (L_x - L_y)$. The terms $h(t - L_(x, y)/c)$ are already at first order in h, so we can simply replace $L_{(x,y)}$ by L. Consequently, the electric field at the beam splitter at $t_0^{(x,y)}$ for a plus only polarized wave $h_+ = h_0 \cos(\omega_{GW} t)$ is given by:

$$E^{(x,y)} = \mp \frac{1}{2} E_0 e^{-i\omega_L (t - 2L/c) + i\phi_0 + i\Delta\phi_{(x,y)}}, \tag{2.20}$$

where $\phi_0 = k_L(L_x - L_y)$ and $\Delta\phi_{(x,y)} = \pm h_0 k_L L \frac{\sin(\omega_{GW} L/c)}{\omega_{GW} L/c} \cos[\omega_{GW}(t - L/c)]$. The parameter ϕ_0 depends only on the arms lengths, therefore it is something that the experimenter can choose. The terms $\Delta\phi_{(x)} = -\Delta\phi_{(y)}$ contain the effect of GW. In the limit of $\omega_{GW} L/c << 1$ we get:

$$\Delta\phi \simeq h(t - L/c) k_L L. \tag{2.21}$$

From this equation we see that the effect of GW in the detector gets more significant for larger L. For typical GW this translates into arms of lengths of hunderds of kilometers. However, this is not feasible in a ground based interferometer both for technical and financial reasons. We tackle this by including cavities into the arms and effectively increase the response of the interferometer. A Michelson interferometer with Fabry-Pérot

cavities in the arms is called a Fabry-Pérot interferometer (see Fig. 2.3).

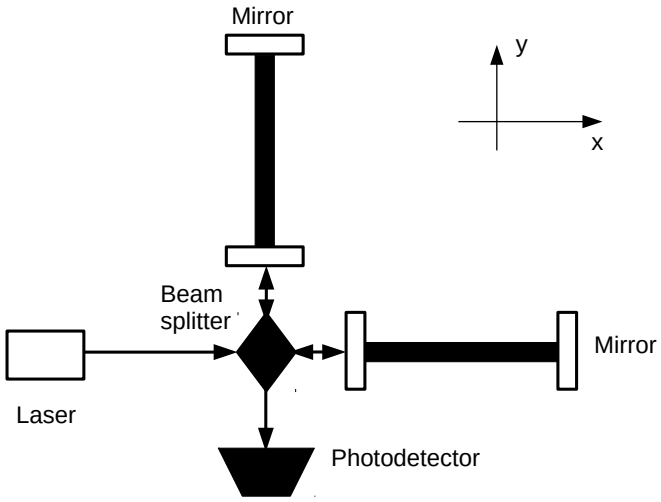

Figure 2.3: Illustration of a Fabry-Pérot interferometer.

A Fabry-Pérot cavity consists of two mirrors placed parallel to each other at a fixed distance. An incoming electric field into the cavity is partially transmitted and reflected when it reaches the mirrors. This causes the field to be trapped inside the cavity and bounce constantly back and forth. In an interferometer, this effectively increases its response, making it more suitable for GW detection. We consider again an only plus polarized wave with $h_+ = h_0 \cos(\omega_{GW} t)$. In this case, Eq. 2.21 for the cavity along the x axis becomes:

$$\Delta\phi \simeq \frac{2F}{\pi} k_L L h_0 \cos(\omega_{GW} t), \tag{2.22}$$

where F is called finesse of the cavity. It is defined as (see Section 9.2.1 of Ref. [1]):

$$F = \frac{\pi\sqrt{r_1 r_2}}{1 - r_1 r_2}, \tag{2.23}$$

where r_1, r_2 are the amplitude reflectivities of the two mirrors of the cavity. As we can see, the response has increased by a factor of $(2/\pi)F$. From the discussion in this section we understand that our detectors response to incoming GW depends on the relative difference between the length of the arms. However, as we saw in the previous chapter, there are special directions from which incoming waves do not affect the relative

difference. Consequently, interferometers have blind spots over the sky and are not able to detect any GW coming from those. This effect can be minimized by building more interferometers with different orientations.

Currently, there exist three ground-based, fully operational, Fabry-Pérot interferometers able to detect GW. Two of them are 4-km long arm interferometers, they consistute the Laser Interferometer Gravitational-Wave Observatory (LIGO) and are located at Hanford and Livingston, both in the USA. The third operational interforemeter is Virgo, which is a 3-km arm long interferometer located at Cascina, Italy. LIGO led to the first GW detection [21] and Virgo joined the official observational runs two years later. In Fig. 2.4 the locations of these interferometers can be seen, as well as some additional current or planned interferometers. The GEO600 is a 600-meter long arm operational interferometer that is located in Hanover, Germany. KAGRA is a 3-km arm long interferometer located at Japan near the Kamioka mine. Both of those are operational but with not enough sensitivity to be able to detect GW. KAGRA is currently being upgraded and is expected to reach the necessary sensitivity. LIGO-India is another interferometer that is currently being made, but is not operational yet.

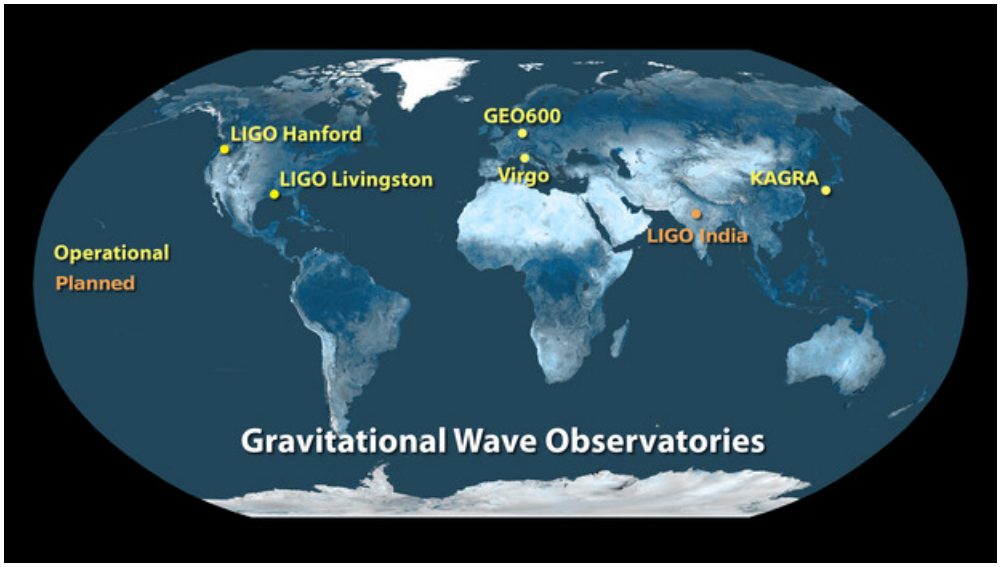

Figure 2.4: World map with the locations of the ground-based interferometers taken from https://www.ligo.caltech.edu/image/ligo20160211c.

2.3 Noise Sources

As every detector, interferometers are suffering from various noise sources that we need to take into account in order to be able to detect GW. In this chapter we will consider some of the sources of noise that couple into the interferometer's signal and reduce its sensitivity.

2.3.1 Quantum Noise

Quantum noise originates from effects due to the quantum nature of light and of particles that compose the interferometer's parts, like the mirrors. It mainly composes of shot noise and radiation pressure noise at high and low frequencies, respectively. Below we briefly discuss those.

Shot Noise

The first noise source originates from the quantum nature of the laser. As it is well known, laser light comes in discrete quanta, i.e. photons. Assuming that during an observation time T the number of photons that reach the photodetector is N_γ, the average power measured is given by:

$$P = \frac{1}{T} N_\gamma \hbar \omega_L, \tag{2.24}$$

where $\hbar$ is the reduced Planck constant and ω_L is the frequency of the laser. When we try to count the number of discrete independent events, the outcome of measurements is governed by the Poisson statistics:

$$p(N|M) = \frac{1}{N!} M^N e^{-M}, \tag{2.25}$$

where M is the average value of N. When N is large the Poisson distribution becomes a Gaussian distribution with standard deviation $\Delta N = \sqrt{N}$. Therefore, there is a

fluctuation in the power measured by the photodetector given by:

$$\Delta P_{shot} = \frac{1}{T}\Delta N_\gamma \hbar\omega_L = \frac{1}{T}\sqrt{N_\gamma}\hbar\omega_L = \left(\frac{\hbar\omega_L}{T}P\right)^{1/2}. \tag{2.26}$$

In the absence of GW, the output power of a Michelson interferometer is $P \propto |E_{out}|^2$, where E_{out} is given by Eq. 2.17. Therefore, we find:

$$\Delta P_{shot} = \left(\frac{\hbar\omega_L}{T}P_0\right)^{1/2} |\sin\phi_0|, \tag{2.27}$$

where P_0 is the input power. From Eq. 2.20 we see that when GW pass, the output power of the interferometer becomes:

$$P = P_0 \sin^2(\phi_0 + \Delta\phi) = P_0 \sin^2(\phi_0) + P_0|\sin 2\phi_0|\Delta\phi + (\text{higher order terms}). \tag{2.28}$$

From the equation above we see that the fluctuation in the power due to the GW is given by:

$$(\Delta P)_{GW} = P_0|\sin 2\phi_0|\Delta\phi. \tag{2.29}$$

Consequently, the signal-to-noise ratio, assuming only the shot noise for a wave with only the plus polarization and coming from optimal direction, is:

$$\frac{S}{N} = \frac{(\Delta P)_{GW}}{\Delta P_{shot}} = \left(\frac{\hbar\omega_L}{TP_0}\right)^{-1/2} 2k_L L h_0 |\cos\phi_0|. \tag{2.30}$$

For a Fabry-Pérot interferometer this ratio is multiplied by a factor $(2/\pi)F$. The strain sensitivity is given by (see Section 9.4 of Ref. [1]):

$$\frac{S}{N} = \left[\frac{T}{S_n}\right]^{1/2} h_0. \tag{2.31}$$

Comparing the two last equations we find:

$$S_{n,shot}^{1/2} = \frac{1}{2k_L L|\cos\phi_0|}\left(\frac{\hbar\omega_L}{P_0}\right)^{1/2}, \tag{2.32}$$

.

Radiation Pressure

From Eq. 2.30 it can be seen that as we increase the power of the laser (P_0) then the signal-to-noise ratio of the shot noise becomes larger. This means that the shot noise becomes less important. However, increasing the power of the laser comes with a trade off. As we keep increasing the power, the radiation pressure that the incoming photons apply on the mirror becomes more important. Since the exact number of photons that hit the mirror fluctuates, this means that this pressure is not constant and will create a fluctuating force that moves the mirror.

To calculate the effect of the noise coming from radiation pressure consider a photon that hits the mirror and gets reflected back. The change in the momentum of the photon is twice the initial momentum of the photon $2|p|$. Since the energy of the photon is $E \propto p$, the force of a beam with power P on the mirror is $F = 2P/c$. Therefore, we have:

$$\Delta F = 2\sqrt{\frac{\hbar\omega_L P}{c^2 T}}. \tag{2.33}$$

Consider now the case of a Michelson interferometer of arms length L. Assuming that we have a mirror of mass M and that the photons move towards the x axis, then the force that acts on the mirror is $F = M\ddot{x}$. In the fourier space this is $\tilde{F}(f) = -M(2\pi f)^2\tilde{x}$. Following the arguments in Section 9.4.2 of Ref. [1] it turns out that for the radiation pressure case we have:

$$S_{n,rad\ pres}^{1/2} = \frac{4}{ML(2\pi f)^2}\sqrt{\frac{2\hbar\omega_L P}{c^2}}. \tag{2.34}$$

As we can see from above equation, the noise in this case is $S_n^{1/2} \propto P^{1/2}$ in contrast to the shot noise which was $S_n^{1/2} \propto P^{-1/2}$. In the case of a Fabry-Pérot interferometer, photons travel back and forth many times, due to fact that we have Fabry-Pérot cavities in the arms. The number of times that photons bounce is of the order $O(N) = (2/\pi)F$, where F here is the Finesse of the cavity. This brings another multiplicative factor in the above expression. For more details the reader can look at Section 9.4 of Ref. [1]. The quantum noise as a function of frequency can be seen in Fig. 2.5.

2.3.2 Additional Noise Sources

Here we will briefly discuss about additional noise sources that couple into the interferometer and reduce the sensitivity. The reader can follow the references Chapter 8 and Chapter 9 of Refs. [1],[22, 23, 24, 25] for more a detailed discussion.

Thermal Noise

Thermal noise or Brownian noise originates from the Brownian movements of atoms. Those microscopic movements of the atoms give rise to vibrations in the mirrors as well as the suspensions that hold the mirrors in place. The vibrations lead to displacements that couple in the interferometers' signal and limit the sensitivity. The effect of this noise can be computed using the fluctuation-dissipation theorem (see Chapter 9 of Ref. [1]).

Gravity Gradient

Earth's gravity field is not constant but features small variations in time due to microseismic noise. This leads to small mass density fluctuations in the Earth which directly change the gravitational field and couple into the interferometers signal.

Excess Gas

Any amount of residual gas in the tubes of the interferometers arms will lead to an extra noise. This is due to the fact that the gas particles will give rise to fluctuations in the effective refractive index along the laser's path.

The estimated effects of all the aforementioned sources of noises can be seen in Fig. 2.5.

2.3.3 Environmental Noise Sources

In the case of ground-based interferometers, we also need to take into account noise that originates from the environment. In particular, disturbances from the surroundings, like earthquakes, passing vehicles, etc, or disturbances from the infrastructure itself, like

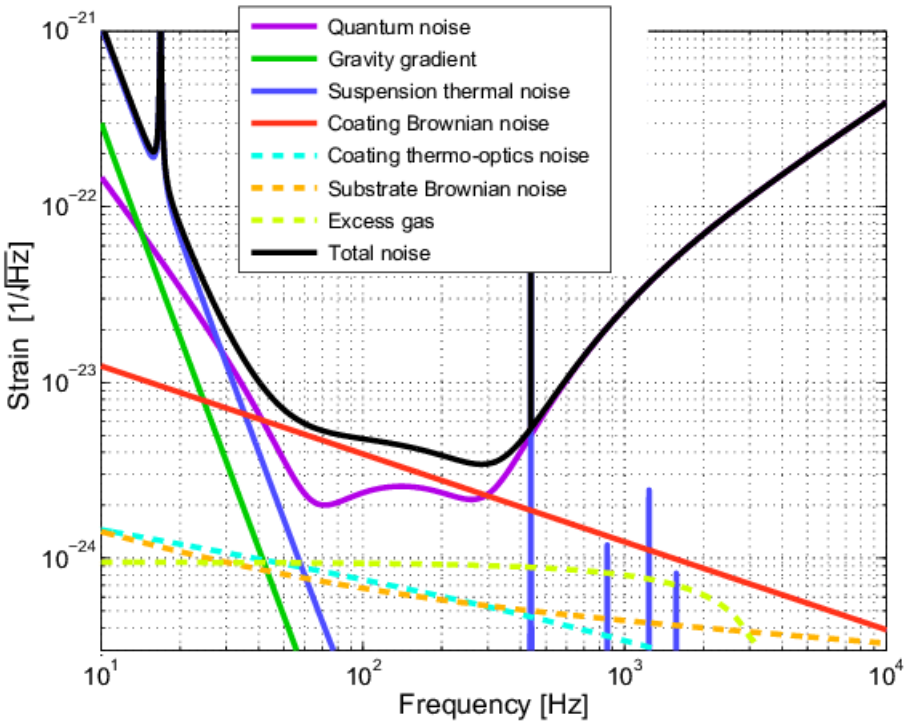

Figure 2.5: The different noises and the total sum of them as estimated for the Virgo interferometer. The plot was taken from Ref. [22].

acoustic, or electromagnetic disturbances, affect interferometers and need to be taken into account. Some infrastructure noises were investigated in [26]. In it, we present the investigation results of various noise features, and their coupling paths, resulting in a decrease of the sensitivity of the detector. Noise hunting is the process during which noise sources and their coupling paths to the interferometer are being identified.

The first noise source that was investigated was the scattered light. Scatter light originates from a small fraction of the laser light circulating in the interferometer that can be scattered off by any illuminated surface. Unless it gets blocked, there is a chance of this light re-entering the main beam path which will cause an additional noise modulated by the motion of the scattering surface. This is called scattered light noise. Typical evidences of scattered light are spectral noise features, such as bumps in photodiode signals, which are non-stationary in time, with a typical timescale of a few hours. Bumps width typically increases with the level of microseismic noise.

We used two experimental methods to test whether scattered light noise was impacting

the sensitivity. Firstly, we switched off the heating, ventilation and air conditioning (HVAC) systems. We witnessed a clear reduction of the noise below 30 Hz (see Fig. 2.6). This led us to believe that the noise bumps at 20 Hz and 40 Hz in the sensitivity are correlated with the acoustic noise inside the laser clean room.

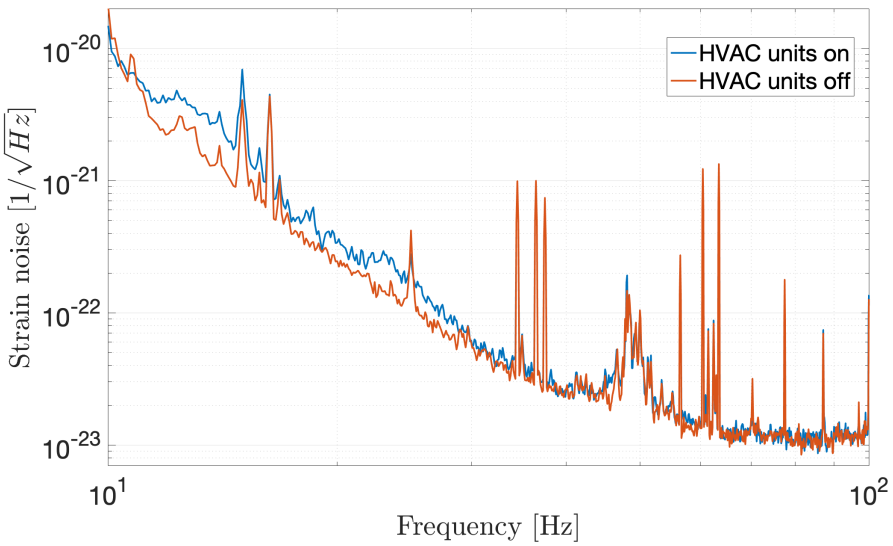

Figure 2.6: Sensitivity before(blue) and while all heating, ventilation, and air conditioning (HVAC) units were off (red).

Secondly, we used shakers and/or loudspeakers to increase the vibration noise of specific parts and try to identify the source of the bump at around 20 Hz. For this we placed a small shaker in one of the laser bench legs in the laser room. We found a clear correlation of this peak with the vibration modes of the table (see Fig. 2.7). Next we moved on investigating possible electromagnetic noise coupling into the interferometer. We performed two injections, a near-field injection trying to localize an anomalous coupling to magnetic fields within the central area, and a far-field to test any possible coupling of ambient magnetic and radio frequency fields.

The near-field injections were done in multiple locations in the north arm end building of Virgo. In Fig. 2.8 the specific locations can be seen. We injected magnetic signals of frequencies 28 Hz and 368 Hz. The colorbar in the plot indicates the effect in the amplitude spectral density (ASD).

We found that the coupling of the low frequency stimulus (28 Hz, triangles) was

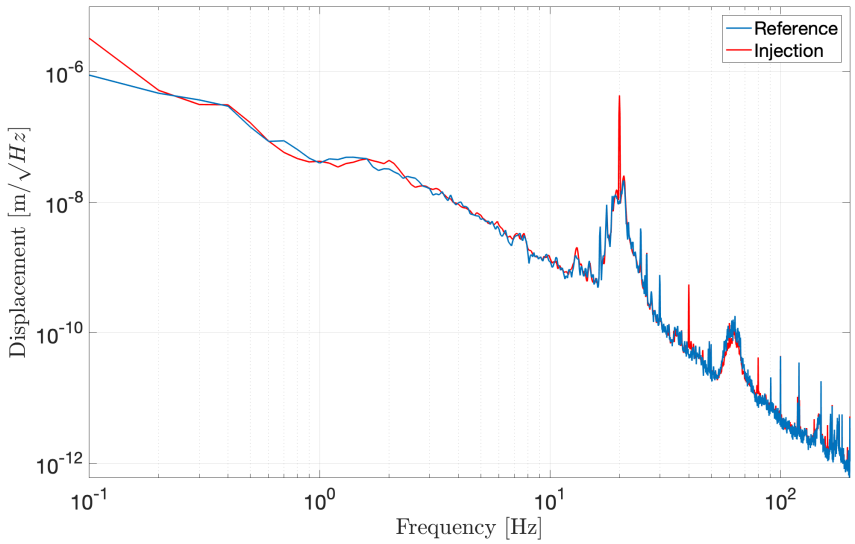

Figure 2.7: Displacement of the bench in quiet condition(blue) and during the seismic noise injection(red).

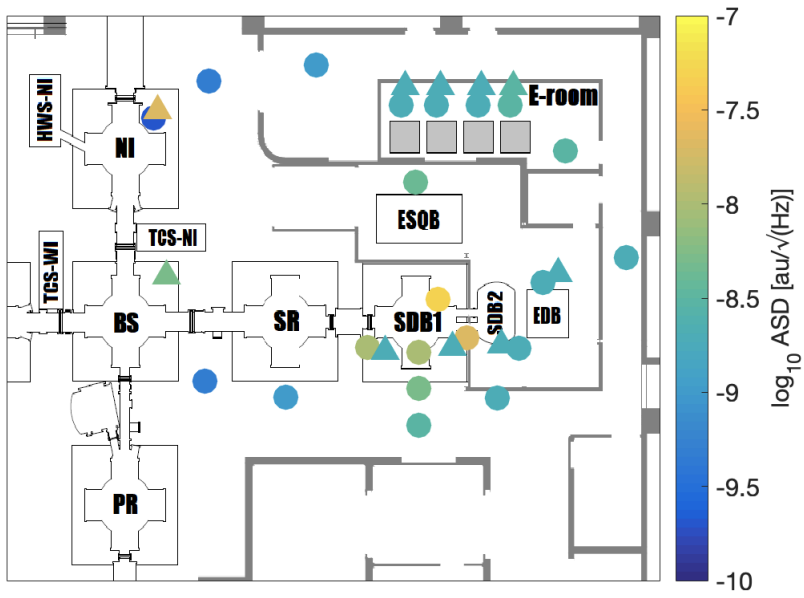

Figure 2.8: Near-field magnetic injection map. Positions of injections for both signals at 28 Hz (triangles) and at 368 Hz (circles). The marker color shade indicates the intensity of the induced excitation measured in the output port power.

becoming stronger near the mirror at the input of the North arm (NI). This is due to some magnets that are located on the mirror to reduce the total magnetic moment. On the other hand, the coupling of high frequency stimulus (368 Hz, circles) got more significant as we approached the output suspended bench (SDB1). In this case we

identified the noise path as: ambient magnetic fields shake the SDB1 bench acting on the coil-magnet actuators. The enhanced bench vibration increases the coupling of scattered light noise from the bench.

The far-field injections were performed in the central building of Virgo. In Fig. 2.9 the noise projection of the ambient magnetic field for different ASD percentiles of the magnetic field can be seen (different blue curves), as well as the quiet strain noise of the interferometer (black curve). In the case of the noise being close to the quiet strain,

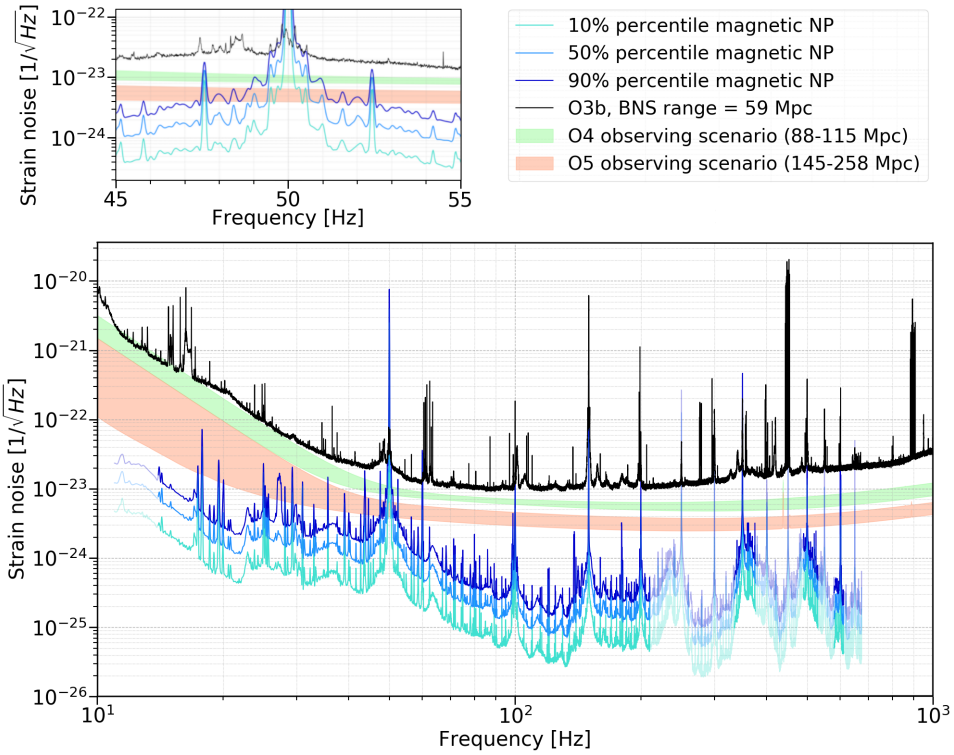

Figure 2.9: Noise projection of ambient magnetic fields in the central building. The strength of the ambient magnetic field is visualized in the form of percentiles computed over one week period with a frequency resolution of 0.05 Hz. The projected noise (blue shaded curves) is compared with the O3b measured sensitivity (black curve) and with Virgo future observing scenarios, named O4 and O5.

this requires immediate attention since it will reduce the current sensitivity. If that is not the case, it can be ignored, however it might become relevant as the detector sensitivity improves. We assume that if the noise is at least a factor of ten below the current sensitivity, it is not expected to contribute significantly currently, but might become a problem in the future observing runs. If the noise is closer than that, but

still below the current sensitivity, it will become a problem in the following run as the sensitivity of the detector will improve. As we can see in the figure, we found that the noise from the ambient field was well below the strain for most of the frequency band at that time sensitivity (O3b). However, there were some frequencies where the 90^{th} percentile (or even 50^{th} percentile) had a predicted noise level which was less than a factor of ten below the strain noise. This means that if nothing is done, the magnetic noise will become important for the next runs (O4,O5) where the sensitivity of the detector is expected to be better.

Finally, we investigated the noise coming for the main electric system (mains) in Virgo, which is at 50 Hz. The noise appeared as symmetric peaks around 50 Hz. The most significant was a pair of peaks that could be grouped in two families: one at ± 1.25 Hz, with its double at ± 2.5 Hz, and another at ± 1.7 Hz with its double at ± 3.4 Hz and triple at ± 5.1 Hz (see Fig: 2.10). This noise is associated with power controlled loads that cause periodic amplitude modulation of the mains. To identify from which device the noise was coming from, we used a magnetic probe that was connected to a portable Chromebook. We followed the noise emissions along power cables and which led us at the two optical benches hosting the CO_2 lasers of the switchboard in the thermal compensation system area. Finally, by selectively switching off devices on the benches, the source was identified in the infrared laser beam profiles. In Fig: 2.10 one can see the response of the magnetometer (top plot) and the strain noise curve of Virgo (bottom plot) when the selected devices were off (blue) or on (red).

2.4 Monitoring of the Stray Light Using an Instrumented Baffle

Scattered light is one of the most significant noise sources in an inteferometer. To monitor it, an instrumented baffle was installed in the Virgo input mode cleaner cavity in preparation for the installation of baffles in the main arm cavities. The input mode cleaner cavity purpose is to isolate any higher order modes of the beam before it enters the arm cavities. The installation of the baffle was done on April 2021[27].

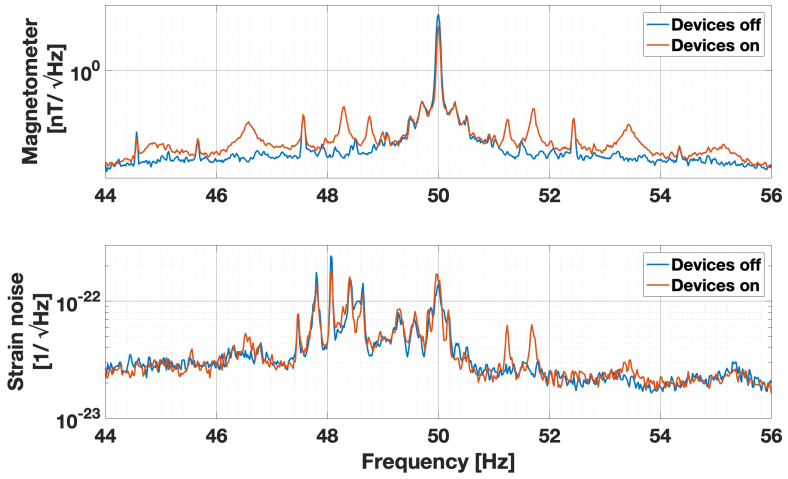

Figure 2.10: Response of a magnetometer (top) and the strain noise (bottom) when devices were on (red) and off (blue).

The baffle can be seen in Fig. 2.11. It is divided in two halves with a polished surface. The inner radius of the baffle is 7 cm and the outer is 17.5 cm. The baffle

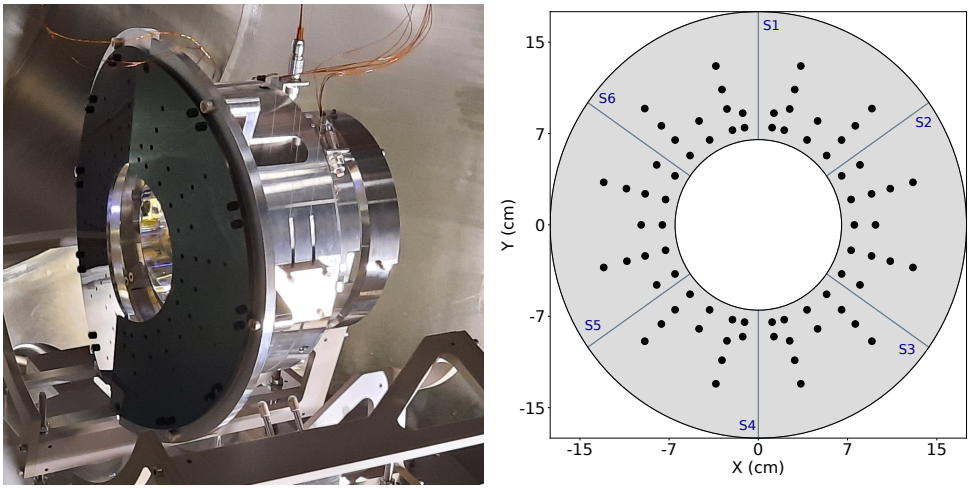

Figure 2.11: (left) Picture of the instrumented baffle installed inside the input mode cleaner tower. (right) Sketch of the location of the photosensors in the baffle in the x-y plane. The gray lines define the six regions where sensors signals are added to determine various observables in the data and simulation.

features holes in its surface which allow for photosensors to be placed behind to monitor the stray light. It has in total 76 sensors symmetrically placed shown as in the right plot of Fig. 2.11. The calibration of the photosensors was done in the laboratory before their installation in the baffle. They showed a good linearity in the response for the whole range of interest and a less than 3% sensor-to-sensor variation.

The first raw measurements from the baffle can be seen in Fig. 2.12 in the top plots. In those, the average number of counts that each photosensor measured can be seen from the different colors of each. The values that corresponds to each color can be seen in the colorbar. The two plots were made from two different data sets, averaging over one hour of data taking. The baffle showed good performance in the absence of light in the cavity with average noise levels in the channels limited to up to seven counts, with a root mean square of 0.01 to 0.16 counts. As expected, the signals are concentrated at low radius with sensors reaching more than 100 counts. In the same figure, the bottom plot shows

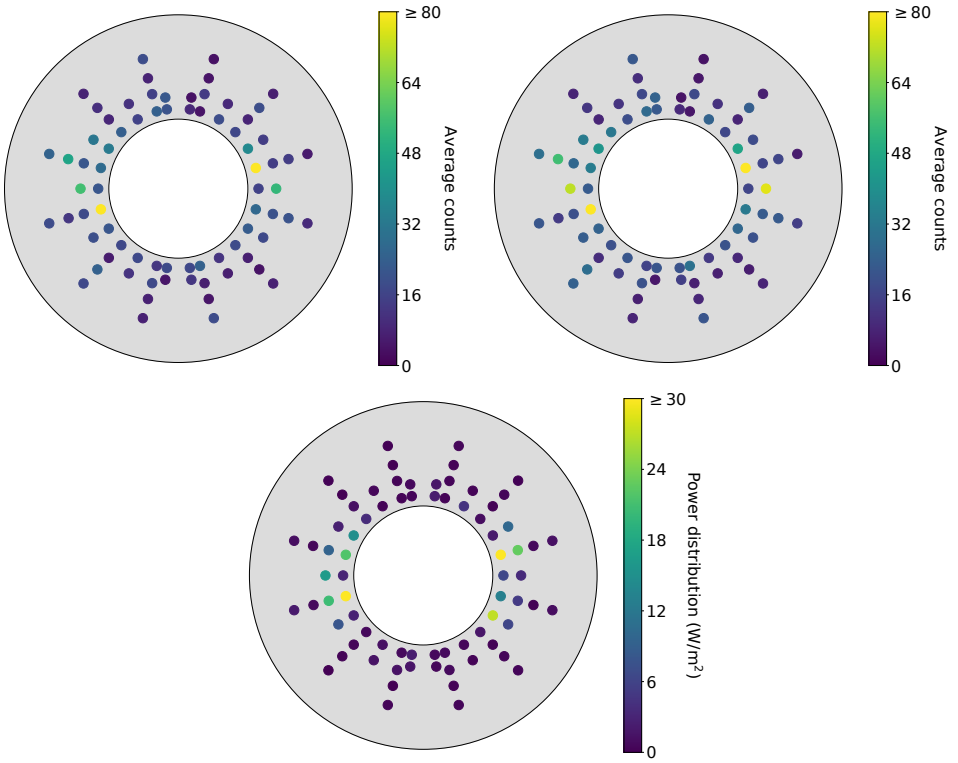

Figure 2.12: 2-D map of the power distribution for measurements on two different data sets (top) and from simulations (bottom).

a power distribution of light in the surface of the baffle. This plot was created from simulations of the cavity with the baffle only approximately simulated as a geometrical position. In the colorbar the power in W/m^2 that corresponds to each sensor can be found. The comparison of the simulation and the actual raw data is in accordance. The results will be used to calibrate the simulations and will be useful in future attempts to understand and reduce the scattered light noise.

The baffle installed in the input mode cleaner was a first approach to the baffle design, installation and analysis of the data that it provided. It has been taking data for more than a year (at the time of writing) with no degradation of performance. The current plan is to follow up with an installation of baffles in front of the end mirrors in the towers of Virgo.

Chapter 3

Inference of Cosmological Parameters Using Gravitational Waves

The detection of GW offers a new way of observing the Universe. Specifically for cosmology, GW are highly important since they serve as standard sirens. A standard siren is an object whose luminosity distance (Eq. 1.66) can be found from the signal alone, requiring no additional calibration. Indeed, as was stated in Chapter 1, GW signals from compact binary coalescences at our detectors are inversely proportional to their luminosity distance. This is important since analyses that are using luminosity distances, like cosmological inference analyses, are more robust and less prone to systematics errors. In this chapter we will see how we can use GW data to infer cosmological parameters, as well as other parameters that are of astrophysical interest.

3.1 Introduction to Bayesian Inference

To be able to give estimations of parameters that govern the theory or model that we want to test, we need to perform a statistical analysis. Bayesian inference is most useful for testing theories and estimate the most probable values of parameters. It is based in the construction of a probability distribution function, called posterior, from a prior

probability distribution and a likelihood function. The prior probability expresses the knowledge that we have for the parameters before the data get analysed. The likelihood function is constructed based on the statistical model that we use.

The posterior is given by the Bayes theorem:

$$p(\theta|x, I) = \frac{p(x|\theta, I)p(\theta|I)}{p(x|I)}, \tag{3.1}$$

where θ are the parameters that we wish to estimate and x are the observations, or data points. The term $p(x|\theta, I)$ is the likelihood and represents the probability of observing the data x given θ. The term $p(\theta|I)$ is the prior and is the knowledge that we have on θ before x is analyzed. Finally, the term $p(x|I)$ is the marginal likelihood and is given by:

$$p(x|I) = \int p(x|\theta, I)p(\theta|I)d\theta. \tag{3.2}$$

The notation I expresses any additional information that is not explicitly stated. This term will be expanded when the information it contains becomes pertinent.

Bayesian inference can also be used as a criterion for choosing between models from the data through the calculation of the Bayes factor. Assuming two models M_1, M_2, each with parameters θ_1, θ_2, and some observed data x, the Bayes factor is given by:

$$B = \frac{p(x|\theta_1, M_1)}{p(x|\theta_2, M_2)} = \frac{p(\theta_1|x, M_1)p(\theta_2)}{p(\theta_2|x, M_2)p(\theta_1)}. \tag{3.3}$$

Calculating the Bayes factor allows for a direct evaluation of which model is the most preferable based on the data. As we will see in the next sections this is very useful when the exact model is unknown. We will make use of Bayesian inference in the next chapters.

3.2 Inference of Cosmological Parameters Using Solely Gravitational Waves

In Chapter 1 we have seen that GW provide the luminosity distance of the events. This is highly important for cosmology since few luminosity distances to events or objects are known in the entire Universe. Additionally, if we could acquire the redshift of the sources, we could give estimations about the cosmological parameters that govern a specific cosmological model. One way to get an estimation of the redshift is by assuming that the masses of black holes in their source frame follow a certain distribution [28]. This method of acquiring the redshift depends only on GW data and uses no electromagnetic (EM) information (for example, no galaxy catalogues).

We consider the case of GW produced by compact binaries coalescence (CBC), and more specifically black holes. We denote the distribution of source frame masses of black holes as $p_s(m_s|\Lambda_m)$, where Λ_m is the set of hyper-parameters that govern the p_s distribution. Due to expanding background of the Universe, the masses will be redshifted and the mass distribution in the detector frame will be different than p_s.

Analyzing the GW data we get estimations of the detector frame masses of the black holes, as well as the luminosity distance to the event. Assuming a cosmological model with hyper-parameters Λ_c we can transform the luminosity distance to redshift $z = z(d_L|\Lambda_c)$. This allows to infer the source frame masses distribution from the observed detector frame distribution. Consequently, by assuming a certain p_s model and a cosmological model, we can conjointly put constraints on the parameters Λ_c and Λ_m by inferring which values fit better the observed data.

We need to construct the general Bayesian framework for the conjoint estimation of cosmological parameters and any additional parameter that govern our models, like for example the mass parameters. We denote the set of cosmological and other parameters as $\Lambda = \{\Lambda_c, \Lambda_m, ..\}$. Assuming that we have N_{obs} GW detected events associated with data $\{x\} = \{x_1, x_2, ..., x_{N_{obs}}\}$, the posterior on Λ in this case can be written as:

$$p(\Lambda|\{x\}, N_{obs}, I) \propto p(\{x\}, N_{obs}|\Lambda, I)p(\Lambda, I), \tag{3.4}$$

where I contains any other information that is not explicitly stated, like for example the cosmological model considered, and $p(\Lambda, I)$ is the prior on Λ. The term $p(\{x\}, N_{obs}|\Lambda, I)$ can be expanded as:

$$p(\{x\}, N_{obs}|\Lambda, I) = p(N_{obs}|\Lambda, I)p(\{x\}|N_{obs}, \Lambda, I), \tag{3.5}$$

where the term $p(\{x\}|N_{obs}, \Lambda, I)$ is the likelihood of observing data $\{x\}$ given Λ and $p(N_{obs}|\Lambda, I)$ is a Poisson distribution that relates the number of observed with the expected number of events:

$$p(N_{obs}|\Lambda, I) \propto \exp(-N_{exp}(\Lambda))N_{exp}(\Lambda)^{N_{obs}}, \tag{3.6}$$

where N_{exp} is the expected number of events, calculated from the merger rate model, which we will introduce later. Each of the GW events are detected in a data chunk x_i and are independent of the data of the rest of the events. In this case we can write:

$$p(\{x\}|N_{obs}, \Lambda, I) = \prod_{i=1}^{N_{obs}} p(x_i|D_{GW}, \Lambda, I), \tag{3.7}$$

where D_{GW} is the hypothesis of having a trigger that passed the detection criteria. Events are defined as the triggers that pass the detection criteria and can be distinguished from noise. For the scope of this work, we will consider the signal-to-noise ratio (SNR) as the detection criteria. Triggers are going to be considered events when their SNR is above a certain threshold that we will impose.

We can further expand the terms in Eq. 3.7 using the Bayes theorem:

$$p(x_i|D_{GW}, \Lambda, I) = \frac{p(D_{GW}|x_i, \Lambda, I)p(x_i|\Lambda, I)}{p(D_{GW}|\Lambda, I)}. \tag{3.8}$$

On the numerator, the term $p(D_{GW}|x_i, \Lambda, I)$ is the probability of detecting an event in the data x_i and with a given set of hyper-parameters Λ. This is by definition equal to 1 since we will only consider events that pass the SNR threshold. Denoting as θ the parameters that describe individual black holes in their source frame, like their masses,

we can write:

$$p(x_i|\Lambda, I) = \int p(\theta|x_i, \Lambda, I) p_{pop}(\theta|\Lambda, I) d\theta. \tag{3.9}$$

The term $p_{pop}(\theta|\Lambda, I)$ is called the population induced prior and gives the prior probability distribution of source frame parameters given certain hyper-parameters. This is given by:

$$p_{pop}(\theta|\Lambda, I) = C p_s(m_{1,s}, m_{2,s}|\Lambda_m, I) R(z|\Lambda_R, I) \frac{p(z|\Lambda_c, I)}{(1+z)}, \tag{3.10}$$

where C is a normalization constant, and the denominator term $1 + z$ comes from the time dilation between the reference frame of the source and the observer. The distribution $R(z|\Lambda_R)$ describes the redshift evolution of the merger rate of CBC events. We can express it as a differential number distribution of total events happening in the Universe N per unit time in the source's frame t_s per unit comoving volume V_c. For this we choose a distribution similar to that of Ref. [29], which is characterized by a low-redshift power-law slope γ, a peak at redshift z_p, and a high-redshift power-law slope κ after the peak (see Fig. 3.1):

$$R(z|\Lambda_R, I) = \frac{dN}{dt_s dV_c} = R_0 \left[1 + (1+z_p)^{-\gamma-\kappa}\right] \frac{(1+z)^\gamma}{1 + [(1+z)/(1+z_p)]^{\gamma+\kappa}}. \tag{3.11}$$

In this case the set of hyper-parameters that governs the distribution is $\Lambda_R = \{z_p, \gamma, \kappa, R_0\}$. The distribution $p(z|\Lambda_c, I)$ gives the redshift distribution of sources given a cosmology model and certain cosmological parameters. We choose a uniform in comoving volume V_c distribution which is given by (see Fig. 3.2):

$$p(z|\Lambda_c, I) = \frac{\partial V_c}{\partial z}(\Lambda_c) = 4\pi C \frac{d_L^2}{H(z)}, \tag{3.12}$$

where C is a constant, d_L is the luminosity distance and $H(z)$ is the Hubble function. The number of expected events N_{exp} mentioned before is given by:

$$N_{exp}(\Lambda) = \int \frac{dN}{dt_{obs} dz}(\Lambda) dt_{obs} dz, \tag{3.13}$$

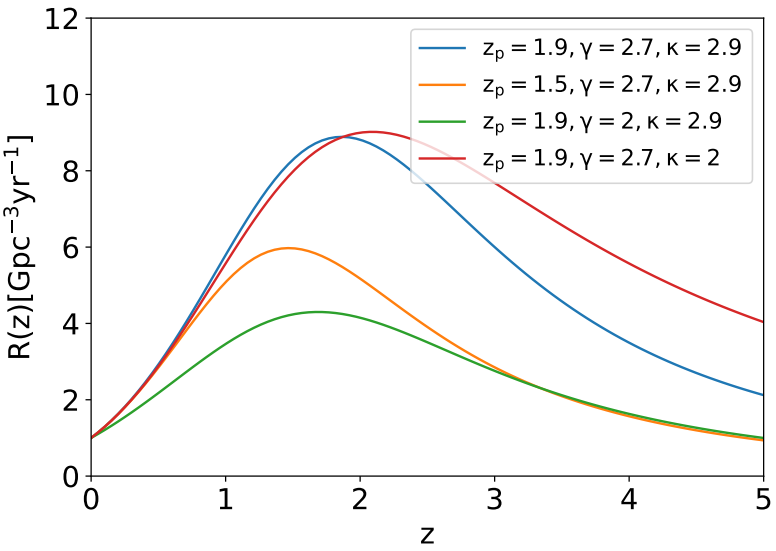

Figure 3.1: The distribution $R(z|\Lambda_R)$ as a function of redshift for various choices of the Λ_R parameters. In this plot $R_0 = 1$ Gpc^{-3}yr^{-1} was assumed.

where t_{obs} is the time measured in the observer's frame. Moving to source's frame and using the merger rate distribution $R(z)$ we find:

$$N_{exp}(\Lambda) = \int \frac{dN}{dt_s dV_c}(\Lambda)\frac{\partial V_c}{\partial z}\frac{dt_s}{dt_{obs}}dt_{obs}dz = T_{obs}\int \frac{R(z)}{1+z}\frac{\partial V_c}{\partial z}dz, \tag{3.14}$$

where T_{obs} is the total observational time.

Finally, the denominator in Eq. 3.8 is a normalization factor of the likelihood $p(x_i|\Lambda, I)$ and describes what is usually referred to as selection effects. This term can be written as an integral over all possible realizations of detectors' data that pass the detection threshold:

$$p(D_{GW}|\Lambda, I) = \int p(D_{GW}, \Lambda|\theta, I)p_{pop}(\theta|\Lambda, I)d\theta. \tag{3.15}$$

The term $p(D_{GW}, \Lambda|\theta, I)$ is the probability of detecting a source with parameters θ and hyper-parameters Λ given a detection criteria and noise realization of the detectors [30, 31, 32, 33]. The integral of Eq. 3.15 can be calculated numerically by doing a series of signal injections into detector noise and retrieving the set of events that passed the detection criteria, along with the parameters of those events. The parameters of the

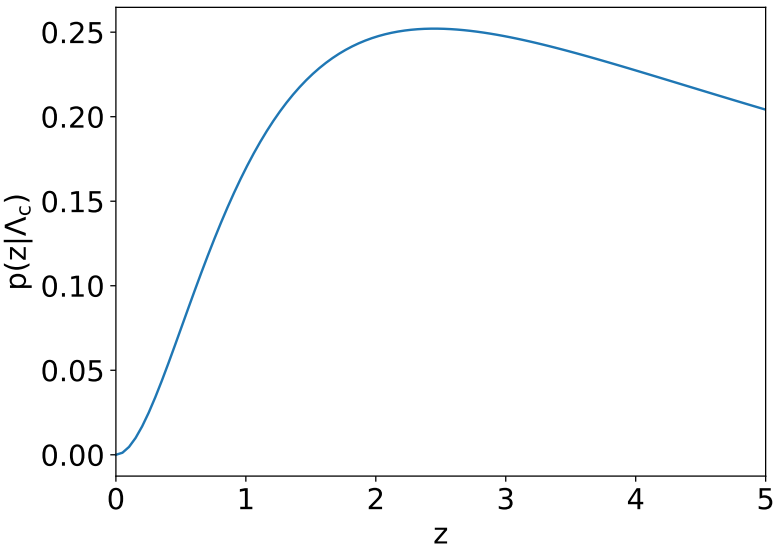

Figure 3.2: The uniform in comoving volume distribution as a function of redshift for a flat ΛCDM cosmology with $H_0 = 70$ km s^{-1} Mpc^{-1}, $\Omega_{m,0} = 0.3$. The distribution is normalized as to have an integral equal to 1.

black holes used in the injections are sampled from some initial distributions. Sources are assumed to be uniformly distributed over the sky. The parameters of a set of injections that were retrieved as detected with an SNR threshold of 9 can be seen in Fig. 3.3 .

Combining everything we arrive at the final expression of the posterior of the hyper-parameters Λ:

$$p(\{x\}|N_{obs}, \Lambda, I) \propto p(\Lambda|I) \prod_{i=1}^{N_{obs}} \frac{\int p(\theta|x_i, \Lambda, I) p_{pop}(\theta|\Lambda, I) d\theta}{\int p(D_{GW}, \Lambda|\theta, I) p_{pop}(\theta|\Lambda, I) d\theta}. \tag{3.16}$$

As we will see in the next chapter, this framework can be used to infer cosmological parameters, as well as other hyper-parameters, solely from GW data without the use of any EM data whatsoever. A flowchart picturing the Bayesian analysis that was described in this section can be seen in Fig. 3.4. A summary of all the notations and parameters that were mentioned here can be seen in Tab. 3.1.

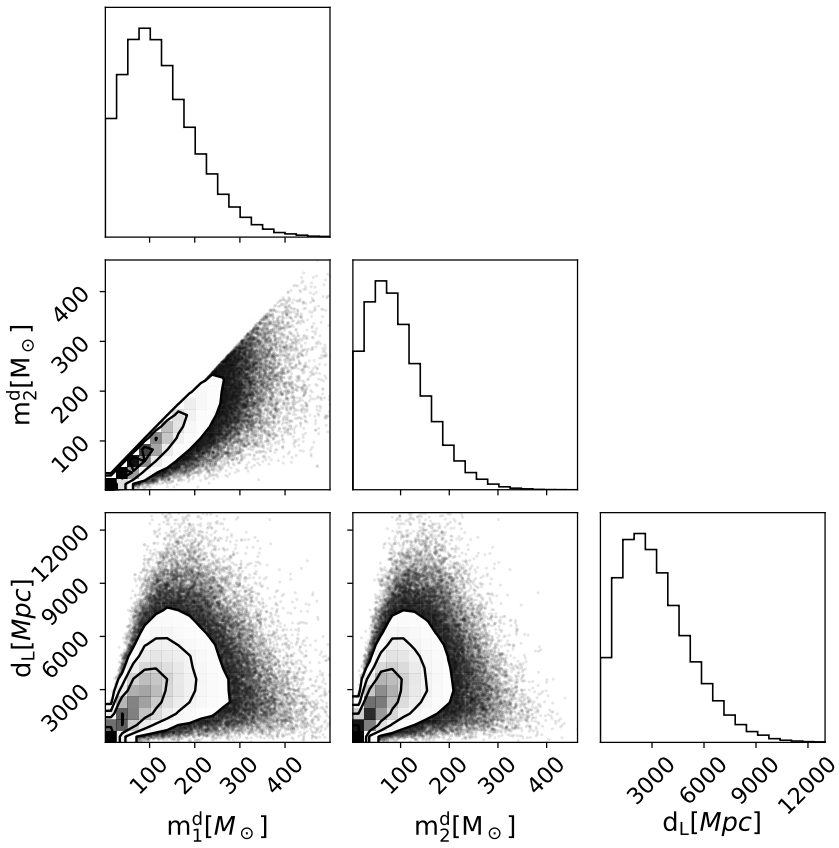

Figure 3.3: Histogram of the luminosity distances and detector frame masses of the injections with SNR higher than 9. The initial distributions from where the values of the parameters were drawn randomly were power-law distributions. For m_1^d the power slope was set to -2, for m_2^d it was set to 1 and for the distance it was set to 2.

3.3 Inference of Cosmological Parameters Using Gravitational Waves and Electromagnetic Data

In the previous section we constructed a Bayesian framework to estimate cosmological parameters using only GW data. However, we have at our disposal EM data that can be used to infer the redshift of the GW sources and use it to estimate the cosmological parameters.

The most straightforward way occurs when we can detect a direct EM counterpart of the GW event. Collisions of binary black boles (BBH) are not expected to emit any EM counterpart. However, this is expected for collisions of neutron star black holes (NSBH) binaries or binary neutron stars (BNS). Since EM counterparts are very well

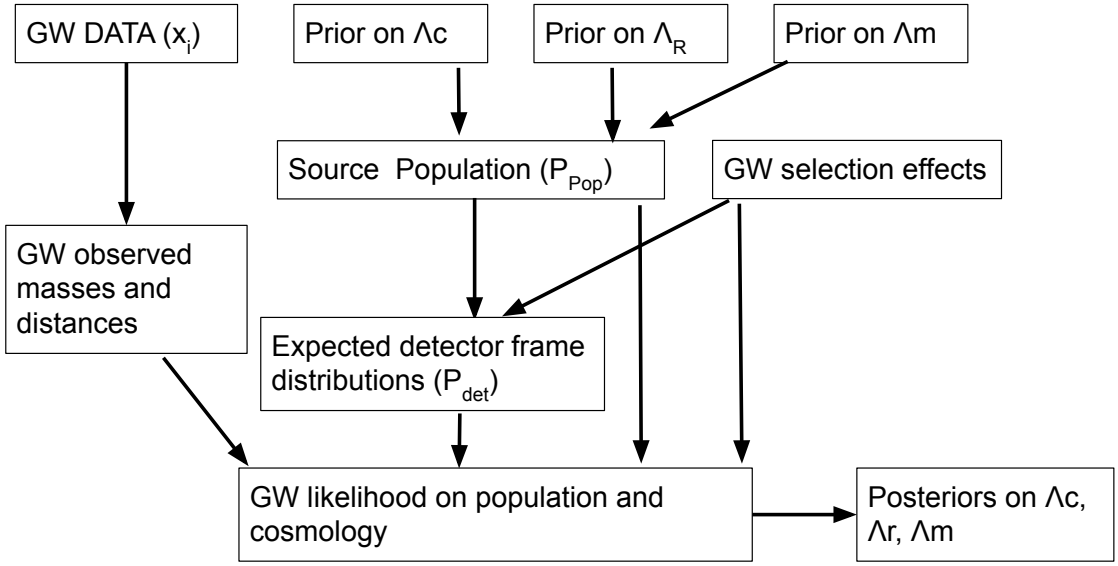

Figure 3.4: Flowchart of the Bayesian analysis described in Sec. 3.2.

localized in the sky, their detection can provide the redshift of the source by doing a cross correlation with galaxy catalogues and identifying the host galaxy.

In the case of absence of an EM counterpart detection, we can still do a cross correlation of the estimated sky area (see Fig. 3.5) of GW events and galaxy catalogues and get a statistical evaluation of the sources' redshifts (Sec. 3.3.1). With this we can get an estimation of cosmological parameters. In this section we will describe the Bayesian framework for both of these methods.

3.3.1 Galaxy Catalogue Method

If an EM counterpart is not detected, then we have to use a statistical method to infer the redshift of the sources. This relies on the cross correlation of the estimated sky area of an event, obtained from data analysis of the GW signal, with a galaxy catalogue [36, 37, 38, 39, 40, 41, 42, 43]. Galaxy catalogues contain a large number of galaxies with measured positions, luminosities and redshifts. By cross correlating the estimated sky area of an event with a galaxy catalogue, it is possible to retrieve a statistical redshift distribution by taking all the galaxies that lie inside the events' sky area (see Fig. 3.6).

First we need to describe the Bayesian framework that we are going to use [45, 46].

Parameters	Description
Λ	Set of hyperparameters we consider in our analysis, $\Lambda = \{\Lambda_c, \Lambda_R, \Lambda_m\}$.
Λ_c	Set of cosmological hyperparameters, like H_0.
$H(z)$	Hubble function.
H_0	Hubble constant.
$\Omega_{m,0}$	Energy density of matter at $z = 0$.
Λ_R	Set of hyperparameters related to the merger rates of BBHs.
$R(z)$	Merger rates model of BBHs.
R_0	Value of the merger rate model at $z = 0$.
γ, κ	Power law indexes of the merger model.
Λ_m	Set of mass hyperparameters, like the maximum mass value.
N_{obs}	Number of observed events.
N_{exp}	Expected number of events.
d_L	Luminosity distance of events.
z	Redshift of events.
V_c	Comoving volume given a cosmology.
x_i	GW data of the i^{th} event.
D_{GW}	Denotes that a GW signal was detected.
θ	All parameters that describe black holes in their source frame.
$m_{(1,2),s}$	Masses of black holes in their source frame.
$m_{(1,2),d}$	Masses of black holes in the detector frame.

Table 3.1: A brief description of the notation and parameters mentioned in Sec. 3.2.

Here we will consider the mass distribution parameters of CBC fixed, as well as the merger rate parameters, and we will focus on cosmological parameters. Specifically, we will focus on H_0 and consider the rest of the cosmological parameters fixed. In the case of N_{obs} GW detected events the posterior of H_0 can be written as:

$$p(H_0|\{x\}, I) \propto p(H_0|I)p(N_{obs}|H_0, I) \prod_{i=1}^{N_{obs}} p(x_i|D_{GW}, H_0, I), \tag{3.17}$$

where I again contains any other information that is not explicitly stated. The term $p(x_i|D_{GW}, H_0, I)$ will incorporate all the information that comes from the galaxy catalogue and the GW data. However, galaxy catalogues are incomplete, in the sense that they do not include all the galaxies of the Universe. There are always galaxies that are too faint to be seen from Earth. This brings an extra source of uncertainty that we need to include into our analysis. We will marginalise over the incompleteness of a galaxy by taking the cases where the real host galaxy of the GW event is or is not in the galaxy catalogue:

$$p(x_i|D_{GW}, H_0, I) = \sum_{g=G,\tilde{G}} p(x_i|g, D_{GW}, H_0, I)p(g|D_{GW}, H_0, I). \tag{3.18}$$

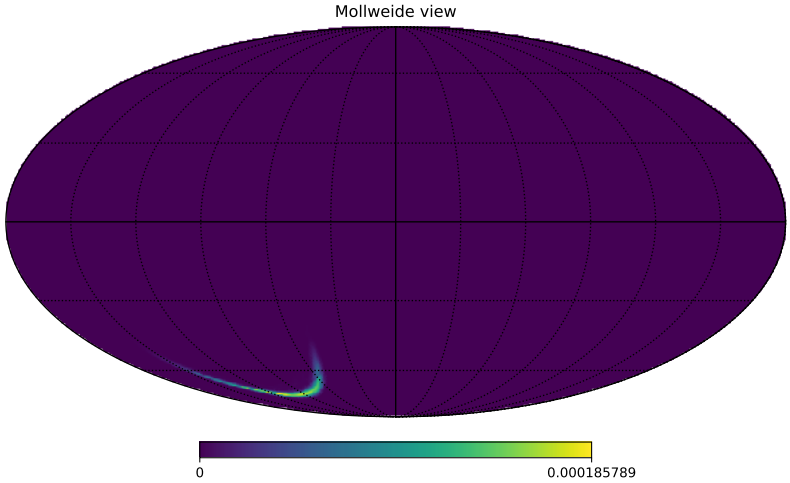

Figure 3.5: The estimated sky area (skymap) of the first GW event detected, GW150914 [21], using the python package HEALPY [34, 35]. The colorbar indicates the event's probability of origin over the sky based on its sky position and the estimated sky area of the GW event.

The terms $p(x_i|g, D_{GW}, H_0, I)$ denote the likelihood of the GW data given H_0 when the host galaxy is (when $g = G$), or is not (when $g = \tilde{G}$), inside the galaxy catalogue and can be obtained by marginalising over redshift, sky location, absolute magnitude and apparent magnitude. Apparent (m) and absolute (M) magnitudes indicate how bright an object is. The former indicates the brightness of an object as it can be seen from the Earth. The latter shows the apparent magnitude that an object would have if it was placed at a distance of ten parsec.

The terms $p(g|D_{GW}, H_0, I)$ denote the probability that the host galaxy is (when $g = G$), or is not (when $g = \tilde{G}$) in the galaxy catalogue, given that a GW signal was detected. We again expand the terms $p(x_i|g, D_{GW}, H_0, I)$ as:

$$p(x_i|g, D_{GW}, H_0, I) = \frac{p(x_i|g, H_0, I)}{p(D_{GW}|g, H_0, I)}, \tag{3.19}$$

and we find:

$$\begin{aligned} p(x_i|D_{GW}, H_0, I) =& \frac{p(x_i|G, H_0, I)}{p(D_{GW}|G, H_0, I)} p(G|D_{GW}, H_0, I) \\ &+ \frac{p(x_i|\tilde{G}, H_0, I)}{p(D_{GW}|\tilde{G}, H_0, I)} p(\tilde{G}|D_{GW}, H_0, I). \end{aligned} \tag{3.20}$$

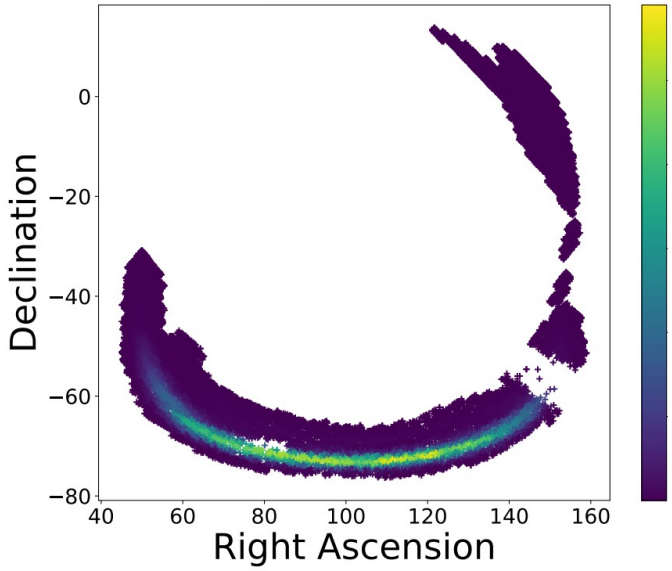

Figure 3.6: All the galaxies that fall inside the estimated sky area (skymap) of GW150914 using the galaxy catalogue Glade v2.4 [44] along with their right ascension and declination (see Fig. 3.7). Each galaxy gets a weight that depends on the probability of the event to originate from that galaxy's position. The colorbar indicates the weight that each galaxy got. Blue indicates the minimum value on the scale and yellow the highest.

We will now focus on each of these terms exclusively, starting from $p(x_i|G, H_0, I)$. This is given by:

$$p(x_i|G, H_0, I) = \int\int\int\int p(x_i|z, \Omega, s, H_0, I)p(z, \Omega, m, M|s, G, H_0, I)dzdmdMd\Omega, \tag{3.21}$$

where z is the redshift, Ω is the sky location, m and M are the apparent and absolute magnitude of galaxies, respectively, and s is the statement that a GW was emitted. The term $p(x_i|z, \Omega, s, H_0, I)$ is the likelihood of the GW data x_i assuming a certain redshift z, a sky location Ω and a Hubble constant H_0. This comes directly from the GW data. The term $p(z, \Omega, m, M|s, G, H_0, I)$ is the prior on z, m, M, Ω for galaxies inside the galaxy catalogue which host a GW source. This information comes directly from the galaxy catalogue which provides a list of galaxies. Each galaxy has a specific redshift,

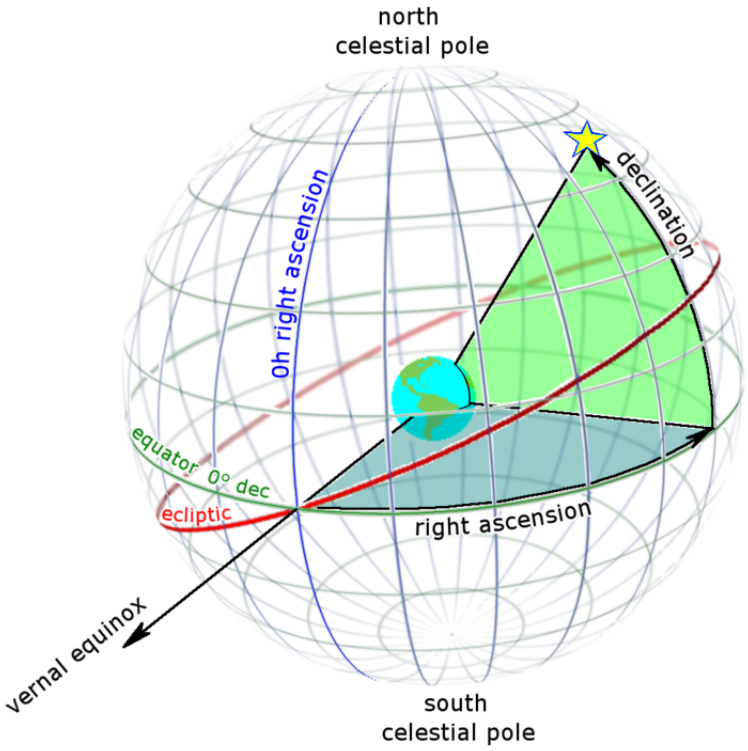

Figure 3.7: Definition of right ascension and declination on the celestial sphere. The plot was taken from
https://commons.wikimedia.org/wiki/File:Ra_and_dec_on_celestial_sphere.png

sky location and apparent magnitude, and thus this term can be expressed as:

$$p(z,\Omega,m,M|s,G,H_0,I) = \frac{p(s|z,M(z,m,H_0),I)\delta(M-M(z,m,H_0))p(z,\Omega,m|G,I)}{p(s|G,H_0,I)}, \tag{3.22}$$

where we have used the fact that knowing z, m, H_0 one can directly calculate the absolute magnitude $M = M(z, m, H_0)$. The term $p(z, \Omega, m|G, I)$ is the prior on z, Ω, m of all the galaxies in the catalogue, while $p(s|z, M(z, m, H0), I)$ is the probability of a galaxy with redshift z and absolute magnitude M to host a GW event. Now using Eqs. 3.21 and 3.22 we find:

$$p(x_i|G,H_0,I) = \frac{1}{p(s|G,H_0,I)}\int\int\int p(x_i|z,\Omega,s,H_0,I)p(s|z,M(z,m,H_0),I) \times p(z,\Omega,m|G,I)dzdmd\Omega. \tag{3.23}$$

Since the galaxies in a galaxy catalogue are discrete objects, we can estimate this integral numerically as a sum over all galaxies:

$$p(x_i|G,H_0,I) = \frac{1}{Np(s|G,H_0,I)} \sum_{j=0}^{N} p(x_i|z_j,\Omega_j,s,H_0,I)p(s|z_j,M_j(z_j,m_j,H_0),I), \tag{3.24}$$

where the sum runs over all galaxies that lie inside the estimated sky area of the i$^{\text{th}}$ GW event. Using the Bayes theorem to expand $p(s|z_j,M_j(z_j,m_j,H_0),I)$ we find:

$$\begin{aligned} p(x_i|G,H_0,I) =& \frac{1}{Np(s|G,H_0,I)} \sum_{j=0}^{N} p(x_i|z_j,\Omega_j,s,H_0,I) \frac{p(z_j,M_j(z_j,m_j,H_0)|s,I)p(s|I)}{p(z_j,M_j(z_j,m_j,H_0)|I)} = \\ =& \frac{1}{Np(s|G,H_0,I)} \sum_{j=0}^{N} p(x_i|z_j,\Omega_j,s,H_0,I) \frac{p(z_j|s,I)p(M_j(z_j,m_j,H_0)|s,I)p(s|I)}{p(z_j|I)p(M_j(z_j,m_j,H_0)|I)}, \end{aligned} \tag{3.25}$$

where we have also considered that the probability of a galaxy with redshift z and M absolute magnitude, assuming that GW were emitted, is just the product of the two probabilities. Further applying the Bayes theorem to $p(z_j|s,I)$ and $p(M(z_j,m_j,H_0)|z_j,s,I)$ results in the following equation:

$$p(x_i|G,H_0,I) = \frac{1}{Np(s|I)p(s|G,H_0,I)} \sum_{j=0}^{N} p(x_i|z_j,\Omega_j,s,H_0,I)p(s|z_j,I)p(s|M(z_j,m_j,H_0,I)). \tag{3.26}$$

Following the same steps for the $p(D_{GW}|G,H_0,I)$ term in Eq. 3.20 we find:

$$p(x_i|G,D_{GW},H_0,I) = \frac{\sum_{j=0}^{N} p(x_i|z_j,\Omega_j,s,H_0,I)p(s|z_j,I)p(s|M(z_j,m_j,H_0,I))}{\sum_{j=0}^{N} p(D_{GW}|z_j,\Omega_j,s,H_0,I)p(s|z_j,I)p(s|M(z_j,m_j,H_0,I))}. \tag{3.27}$$

This expression is sufficient for the simple case where we consider that redshifts of galaxies are delta-like functions. Real galaxies however have redshift uncertainties associated with them. Assuming that we can incorporate the uncertainties into a distribution, such that the redshift distribution of the j$^{\text{th}}$ galaxy is given by $p(z_j|I)$, we can rewrite the

previous equation as:

$$p(x_i|G, D_{GW}, H_0, I) = \frac{\sum_{j=0}^{N} \int p(x_i|z_j, \Omega_j, s, H_0, I) p(s|z_j, I) p(s|M(z_j, m_j, H_0, I)) p(z_j|I) dz_j}{\sum_{j=0}^{N} \int p(D_{GW}|z_j, \Omega_j, s, H_0, I) p(s|z_j, I) p(s|M(z_j, m_j, H_0, I)) p(z_j|I) dz_j}, \tag{3.28}$$

where the term $p(D_{GW}|z_j, \Omega_j, s, H_0, I)$ denotes again the probability of detection. This probability can be seen in Fig. 3.8 as a function of redshift and H_0.

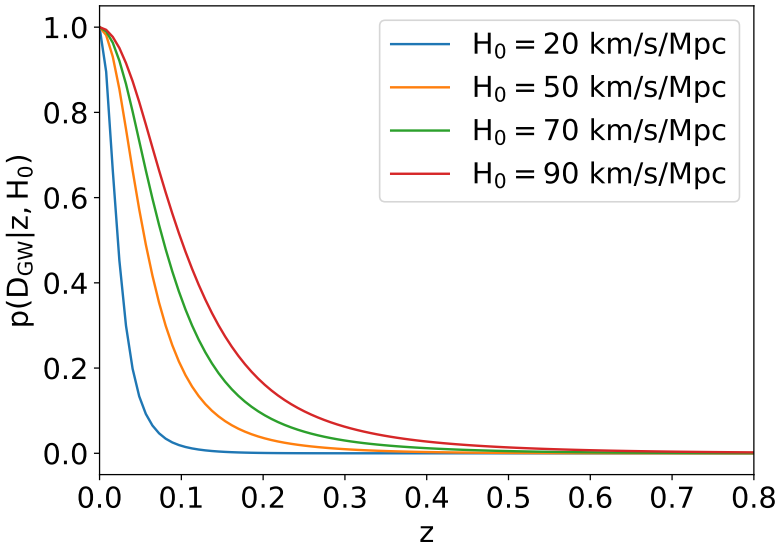

Figure 3.8: The probability of detection as a function of redshift z and H_0.

Next we will focus on the probability of a galaxy to be in the galaxy catalogue $p(G|D_{GW}, H_0, I)$, assuming that a GW event was detected. This term can be expressed as:

$$p(G|D_{GW}, H_0, I) = \int\int\int\int p(G|z, \Omega, m, M, D_{GW}, H_0, I) \times p(z, \Omega, m, M|D_{GW}, s, H_0, I) dz dm dM d\Omega. \tag{3.29}$$

Assuming that galaxy catalogues are apparent magnitude limited - in the sense that only the galaxies for which their apparent magnitudes pass an apparent magnitude threshold $m_{th} = m_{th}(\Omega)$ are contained within the galaxy catalogue - we can approximate $p(G|D_{GW}, H_0, I)$ with a Heaviside step function. By doing this and expanding terms

using the Bayes theorem, the last equation can be written as:

$$p(G|D_{GW}, H_0, I) = \int\int\int\int \Theta[m_{th}(\Omega) - m] \times \frac{p(D_{GW}|z, \Omega, s, H_0, I)p(z, \Omega, M, m|s, H_0, I)}{p(D_{GW}|s, H_0, I)} dz dm dM d\Omega. \tag{3.30}$$

The term $p(z, \Omega, M, m|s, H_0, I)$ is the prior on redshift, sky location, absolute magnitude and apparent magnitude, for galaxies which host a GW source. We consider that z, Ω, M are conditionally independent and then this term can be expressed as:

$$p(z, \Omega, M, m|s, H_0, I) = p(m|z, \Omega, M, s, H_0, I)p(z|s, I)p(\Omega|I)p(M|s, H_0, I). \tag{3.31}$$

We again use the fact that, if z, H_0, M are known, we can calculate $m = m(z, H_0, M)$ and also by expanding terms using the Bayes theorem we find:

$$p(z, \Omega, M, m|s, H_0, I) = \delta(m - m(z, M, H_0))\frac{p(s|z, I)p(z|I)}{p(s|I)}p(\Omega|I)\frac{p(s|M, I)p(M|H_0, I)}{p(s|H_0, I)}. \tag{3.32}$$

The term $p(z|I)$ is the redshift distribution of GW sources in the Universe. We again consider here a uniform in comoving volume distribution. Similarly, $p(M|H_0, I)$ is the absolute magnitude distribution of galaxies in the Universe. For this we consider a Schechter function distribution [47]:

$$P(M|H_0, I) \propto 10^{-0.4(\alpha+1)(M-M^*(H_0)} \exp[-10^{-0.4(M-M^*(H_0)}], \tag{3.33}$$

where α and M^* are model parameters. The term $p(\Omega|I)$ is the prior of sky position of galaxies over the sky, which is taken to be uniform. Finally, we have two terms that describe the weights of galaxies to host GW events based on their redshifts and luminosities. Those are respectively $p(s|z, I)$ and $p(s|M, I)$. The probability of a galaxy

with absolute magnitude M being host to a GW event is taken to be:

$$p(s|M,I) = \begin{cases} L(M), \text{ if we consider luminosity weighting for GW sources} \\ \text{constant , if the GW hosting probability is independent of luminosity} \end{cases}, \tag{3.34}$$

where $L(M)$ is the luminosity of galaxy with absolute magnitude M. As the redshift weighting we use the distribution of Eq. 3.11:

$$p(s|z,I) = \frac{R(z)}{1+z}, \tag{3.35}$$

where again $1+z$ is taken to account for the time dilation between frames. Combining everything together we have:

$$p(G|D_{GW},H_0,I) = \frac{1}{p(s|I)p(s|H_0,I)}\frac{1}{p(D_{GW}|s,H_0,I)}\times \\ \int\int\int_0^{z(M,m_{th}(\Omega),H_0)} p(D_{GW}|z,\Omega,s,H_0,I)p(s|z,I)p(z|I)p(\Omega|I)p(s|M,I)p(M|H_0,I)dzdMd\Omega. \tag{3.36}$$

Performing the same calculation for $p(D_{GW}|s,H_0,I)$ we find the final expression for this term:

$$p(G|D_{GW},H_0,I) = \\ \frac{\int\int\int_0^{z(M,m_{th}(\Omega),H_0)} p(D_{GW}|z,\Omega,s,H_0,I)p(s|z,I)p(z|I)p(\Omega|I)p(s|M,I)p(M|H_0,I)dzdMd\Omega}{\int\int\int p(D_{GW}|z,\Omega,s,H_0,I)p(s|z,I)p(z|I)p(\Omega|I)p(s|M,I)p(M|H_0,I)dzdMd\Omega}. \tag{3.37}$$

Since this is the probability of a galaxy to be inside the galaxy catalogue, we can easily define the probability for a galaxy to be outside the galaxy catalogue:

$$p(\tilde{G}|D_{GW},H_0,I) = 1 - p(G|D_{GW},H_0,I) \tag{3.38}$$

Finally we need to calculate the likelihood when the host galaxy is not in the galaxy catalogue. Following similar calculations as before we arrive at the expression:

$$p(x_i|\tilde{G}, D_{GW}, H_0, I) = \frac{\int\int\int_{z(M,m_{th}(\Omega),H_0)}^{\infty} p(x_i|z,\Omega,s,H_0,I)p(s|z,I)p(z|I)p(\Omega|I)p(s|M,I)p(M|H_0,I)dzdMd\Omega}{\int\int\int p(D_{GW}|z,\Omega,s,H_0,I)p(s|z,I)p(z|I)p(\Omega|I)p(s|M,I)p(M|H_0,I)dzdMd\Omega}. \tag{3.39}$$

Now we can consider the case where the galaxy catalogue is completely empty, i.e. it contains no galaxies. This is easy with our setup since we only have to consider that the apparent magnitude threshold of the galaxy catalogue tends to $m_{th} \to -\infty$. This means that $z(M, m_{th}, H_0) \to 0$ which leads to $p(G|D_{GW}0, s, H_0, I) = 0$, and $p(\tilde{G}|D_{GW}, s, H_0, I) = 1$. In this case, all the contribution in the likelihood comes for the out of catalogue likelihood term. The information that leads to an informative posterior in this special case comes from the population assumptions that we have made. We will see more about this later (see Sec. 4.2.3). A flowchart depicting the Bayesian analysis that was described in Sec. 3.3.1 can be seen in Fig. 3.9.

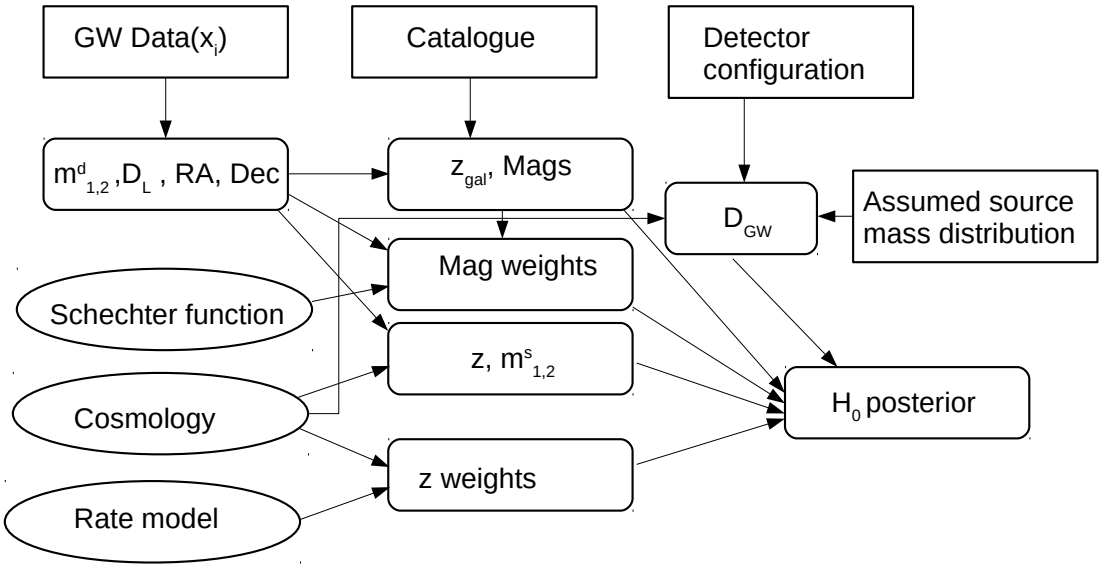

Figure 3.9: Flowchart of the Bayesian analysis described in Sec. 3.3.1.

3.3.2 Detection of an Electromagnetic Counterpart

EM counterparts are expected to be emitted in the case of a BNS event, rather than a BBH. Due to that, in this section we will focus on BNSs. In the event of a confident EM detection, there is a very small estimated sky area - almost point like - where the GW event can originate from. Therefore, it is quite possible that, after the cross correlation with a galaxy catalogue, it will lead to the identification of a single galaxy as the true host galaxy of the event. Here we will describe the modification of the method described previously in the case of EM counterpart detection. Denoting the EM data by x_{EM} and focusing on H_0, we can write its posterior as:

$$p(H_0|\{x, x_{EM}\}, s, I) \propto p(H_0|I) \prod_{i=1}^{N_{obs}} p(x_i, x_{EM}|D_{GW}, H_0, s, I), \tag{3.40}$$

where I contains any other information that is not explicitly stated. There are two reasons for focusing on H_0. First of all, EM counterpart, along with a confident GW BNS event, are expected to be detected only from relative close by galaxies with the current or planned GW detectors, i.e. at small redshifts, and consequently we will not be able to constrain the rest of the cosmological parameters. Secondly, H_0 is of much interest due to the H_0 tension. The term $p(x_i, x_{EM}|D_{GW}, H_0, I)$ incorporates all the information that comes from the EM and the GW data. This term can be expanded using the Bayes theorem as:

$$\begin{aligned} p(x_i, x_{EM}|D_{GW}, H_0, s, I) =& \frac{p(x, x_{EM}|H_0, s, I)p(D_{GW}, D_{EM}|x, x_{EM}, H_0, s, I)}{p(D_{GW}, D_{EM}|H_0, s, I)} = \\ &= \frac{p(x, x_{EM}|H_0, s, I)}{p(D_{EM}|D_{GW}, H_0, s, I)p(D_{GW}|H_0, s, I)}. \end{aligned} \tag{3.41}$$

The term $p(D_{GW}, D_{EM}|x, x_{EM}, H_0, I)$ is equal to 1, as it is assumed that the EM counterpart has been observed and also the GW event has been detected. The term $p(D_{EM}|D_{GW}, H_0, s, I)$ can also be considered equal to 1, as the detectability of EM counterparts is assumed to extend well beyond the distance to which compact binaries

are detectable. We can further expand the numerator as:

$$p(x, x_{EM}|H_0, s, I) = \int\int p(x, x_{EM}|H_0, s, I)p(z, \Omega|s, I)dzd\Omega = \int\int p(x|H_0, s, I)p(x_{EM}|H_0, s, I)p(z, \Omega|s, I)dzd\Omega, \tag{3.42}$$

where it has been assumed that the GW and EM data are independent of each other and so the joint GW-EM likelihood can be split. Expanding the previous term and assuming that, in the case of an EM counterpart a unique galaxy with $z = z_{obs}, \Omega = \Omega_{obs}$ will be identified as the host, we find:

$$\begin{aligned} p(x, x_{EM}|H_0, s, I) &\propto \int\int p(x|z, \Omega, H_0, I)\delta(z - z_{obs})\delta(\Omega - \Omega_{obs})p(\Omega|I)p(s|z, I)p(z|I)dzd\Omega \\ &\propto p(x|z_{obs}, \Omega_{obs}, H_0, I)p(\Omega_{obs}|I)p(s|z_{obs}, I)p(z_{obs}|I). \end{aligned} \tag{3.43}$$

In reality however, even galaxies in a galaxy catalogue have uncertainties, of which the most important are the redshift uncertainties. Assuming that the redshift distribution of the host galaxy is no longer a delta function, but instead is described by $p(z_{obs}|I)$, this gives:

$$p(x, x_{EM}|H_0, s, I) \propto \int p(x|z_{obs}, \Omega_{obs}, H_0, I)p(\Omega = \Omega_{obs}|I)p(s|z_{obs}, I)p(z = z_{obs}|I)p(z_{obs}|I)dz_{obs}. \tag{3.44}$$

Finally, expanding the denominator as before, we find:

$$p(x, x_{EM}|H_0, s, I) = \frac{\int p(x|z_{obs}, \Omega_{obs}, H_0, I)p(\Omega = \Omega_{obs}|I)p(s|z_{obs}, I)p(z = z_{obs}|I)p(z_{obs}|I)dz_{obs}}{\int\int p(D_{GW}|z, \Omega, s, H_0, I)p(\Omega|I)p(s|z, I)p(z|I)dzd\Omega}. \tag{3.45}$$

Tab. 3.2 summarizes all the additional parameters and notations used in the inference of cosmological parameters using GW and EM data.

Parameters	Description
G	Hypothesis that the host of the GW event is inside the galaxy catalogue.
$\tilde{G}$	Hypothesis that the host of the GW event is not inside the galaxy catalogue.
Ω	Sky location (right ascension and declination).
s	Denotes that a real GW signal was emitted.
m	Apparent magnitudes of galaxies.
M	Absolute magnitudes of galaxies.
m_{th}	Apparent magnitude threshold of the galaxy catalogue.
x_{EM}	EM data in case of the detection of an EM counterpart.

Table 3.2: A brief description of the notation and parameters mentioned in Sec. 3.3.1 and Sec. 3.3.2.

3.3.3 Pixelated Approach

Previously we saw how we can construct a posterior on H_0 doing a cross correlation of a galaxy catalogue with the sky area of a GW event. The relations that we found included integration over the sky area where the GW event has support (for the terms where the host is assumed to be included in the galaxy catalogue). This can be done considering the whole sky area of the GW event at once.

However, in that case we also need to make some assumptions. As described before, to calculate the probability that the true host galaxy is inside or outside the galaxy catalogue we need to use an apparent magnitude threshold m_{th}. In the case of considering the whole sky area of the event at once, m_{th} is taken to be the median of the apparent magnitudes of all the galaxies inside the estimated sky area of the event. As GW events can have large estimated sky areas and galaxy catalogues do not have uniform apparent magnitude distributions over the sky, due to known or unknown systematic uncertainties, this approach can become too simplistic.

A second assumption that we have to make concerns the GW data. The term $p(z, \Omega|x, H_0, I)$ contains the information of the distance and sky position of the event. Since we are assuming a given H_0 we can replace the redshift by the distance, i.e. replace $p(z, \Omega|x, H_0, I$ by $p(d_L(z, H_0), \Omega|x, I)$. To be able to integrate this expression we need to make the assumption that the GW data on distance and sky position are not correlated, and thus we can write:

$$p(d_L(z, H_0), \Omega|x, I) = p(d_L(z, H_0)|x, I)p(\Omega|x, I). \tag{3.46}$$

While this assumption does not create any significant bias [45], this approximation requires discarding some useful GW information, meaning that the results produced will be less informative than what they could be.

A more sophisticated approach that addresses both of these issues is the division of the sky into pixels [48]. This method allows for an estimation of the likelihood in each pixel independently, which minimizes both the effects mentioned above. After the calculation in each individual pixel, one needs to combine everything and get the likelihood over the whole sky area of the event. In this case, the likelihood for a single GW event is given by:

$$\begin{aligned} p(x_i|D_{GW}, H_0, I) &= \sum_{j=0}^{N_{pix}} p(x_i|\Omega_j, D_{GW}, H_0, I) p(\Omega_j|D_{GW}, H_0, I) = \\ &= \sum_{j=0}^{N_{pix}} p(x_i|\Omega_j, D_{GW}, H_0, I) \frac{p(D_{GW}|\Omega_j, H_0, I) p(\Omega_j|H_0, I)}{p(D_{GW}|H_0, I)}. \end{aligned} \tag{3.47}$$

Since the probability of detection is considered to be uniform over the sky, we can drop the Ω dependence in those terms and we find:

$$p(x_i|D_{GW}, H_0, I) = \sum_{j=0}^{N_{pix}} p(x_i|\Omega_j, D_{GW}, H_0, I) p(\Omega_j|H_0, I). \tag{3.48}$$

For each pixel it is again necessary to marginalise over the possibility that the host galaxy is in, or outside, the galaxy catalogue. Following the same method as before we can write:

$$p(x_i|\Omega_j, D_{GW}, H_0, I) = \sum_{g=G,\tilde{G}} p(x_i|\Omega_j, g, D_{GW}, H_0, I) p(g|\Omega_j, D_{GW}, H_0, I). \tag{3.49}$$

The expansion of these terms can be done in exactly the same way that was described previously in this section.

Chapter 4

Results

LIGO-Virgo O1, O2 and O3 observing runs took place during 2015-2021. During those runs, 90 confident GW detections originating from CBCs were identified. The methodologies presented in the previous chapter were used to analyze the confident GW detections and estimate various parameters, both cosmological and population related, with emphasis given on the Hubble constant. In this chapter we present the results that were obtained from the analyses.

4.1 Cosmological Inference From the First GW Catalogue

The first O1 and second O2 observing runs, took place from 09/12/2015 to 01/19/2016 and from 11/30/2016 to 08/25/2017, respectively. During those periods the LIGO-Virgo collaboration was able to identify eleven confident GW events, all originating from CBCs, that together form the first gravitational wave transient catalogue (GWTC-1). In this section, we present the cosmological results obtained using events from GWTC-1, but first we present briefly the events that constitute GWTC-1.

4.1.1 First Gravitational Waves Transient Catalogue

The first GWTC [49] consists of eleven CBC events, out of which ten are BBH and one is a BNS. The data from those events have been extensively analyzed by the LIGO-Virgo analysis teams and the posteriors of the parameters of the events (masses, distances,...)

were retrieved. In Fig. 4.1, the posteriors of the compact object's (BHs or NSs) masses,

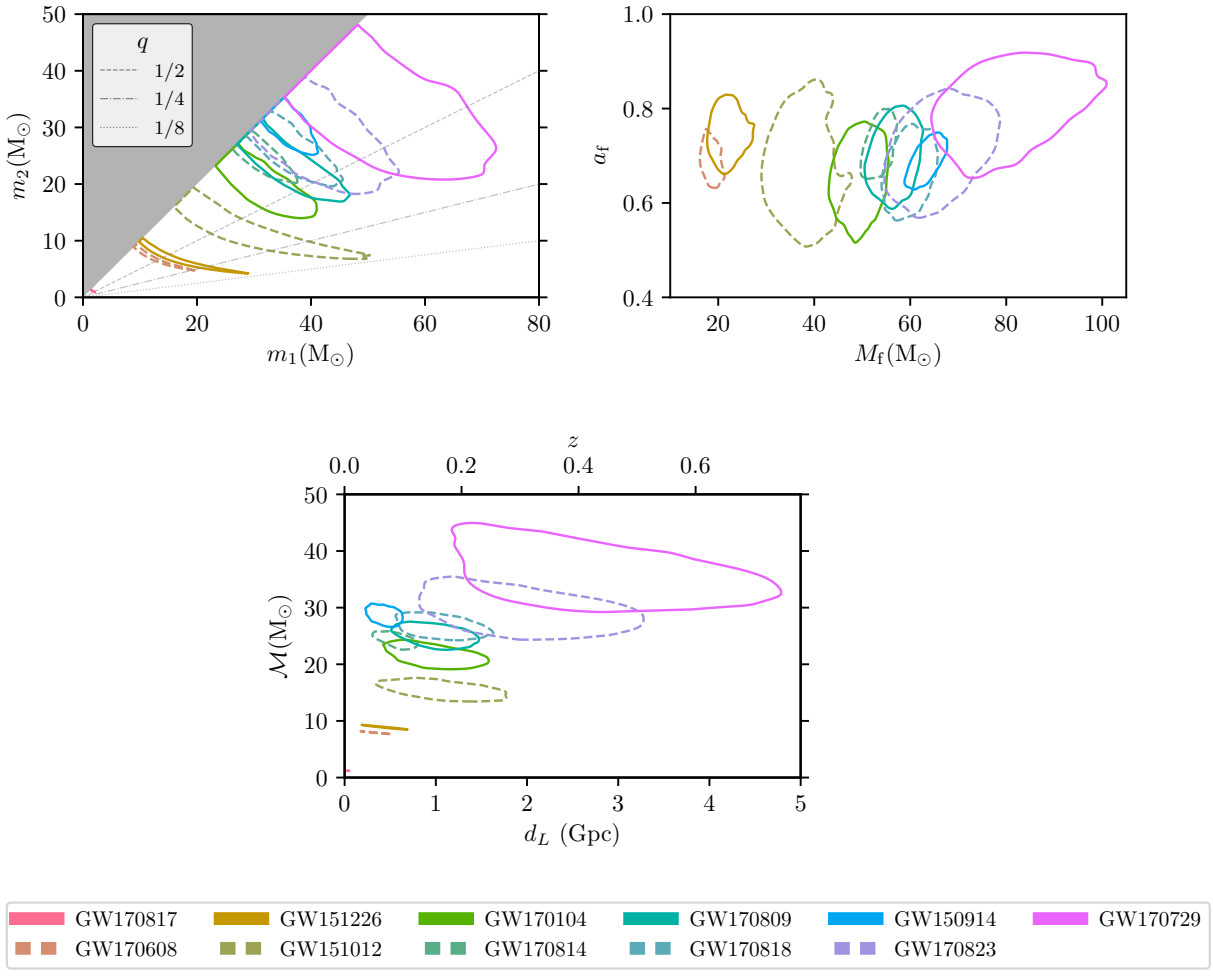

Figure 4.1: Estimated posteriors of the GWTC-1 events taken from Ref. [49]. Contours indicate the 90% confidence intervals of the estimated parameters. Top left: The masses on the two compact objects (BHs or NSs) in their source frame, assuming Planck cosmology. Top right: The spin and the mass of the final BH that was produced from the merger of the individual objects. Bottom: The source frame chirp masses and distances, as well as the redshift, assuming Planck cosmology. In the top right plot, GW170817 can not be seen due to the small final mass of the produced compact object.

distances, as well as the the mass and spin of the final BH, for all the GWTC-1 events can be seen. The countours indicate the 90% confidence intervals of the estimations. The estimated redshift, assuming Planck cosmology [5], can also be seen. All the masses in these plots are calculated in the source frame, assuming again Planck cosmology.

In these plots ten BBHs and one BNS, GW170817 [50], are depicted. The latter

was the first and only GW BNS detection and, at the same time, the first BNS with a detected EM counterpart, which led to the identification of the host galaxy and its redshift. Combining GW and EM data one can get an informative posterior of the Hubble constant (see Sec. 4.1.2). However, as we will see in the next sections, the rest of GW events also provide information that can be used.

4.1.2 Using Galaxy Catalogue Information

As we have seen in the previous chapter, we can use galaxy catalogues to get a statistical redshift estimation for the host galaxies of GW events and be able to do cosmological parameter estimation using GW data. However, if we are able to detect the EM counterpart of an event, then we are able to narrow down the potential host galaxy and get a much better redshift estimation. The methodologies for these cases were described in Sec. 3.3.1 and Sec. 3.3.2, respectively. In the following sections we will use those methodologies in real GW data from GWTC-1 to calculate a Hubble constant posterior.

The Case of GW170817

In the case of GW170817, we were able to detect the EM counterpart. On August 2017, the LIGO and Virgo detectors observed a strong GW signal from a BNS. Two seconds after the merger, a gamma-ray burst (GRB 170817A) was detected within a region of the sky consistent with the LIGO-Virgo-derived location of the GW source event [51, 52, 53, 54]. GW170817 is a highly significant event, especially for cosmology, since in this case a unique galaxy was identified as the true host galaxy [55, 56, 57, 58, 59]. More precisely, an optical transient signal within 10 arcsec of the galaxy NGC 4993 was detected (see Fig. 4.2). NGC 4993 has a redshift of $z = 0.0097$, which allowed for a very informative Hubble constant posterior. GW170817 has an estimated distance of $d_L = 40^{+7}_{-15}$ Mpc at 90% confidence interval. This makes it the closest GW event inside GWTC-1 and the best localized one with a sky area of $\Delta\Omega = 16$ deg^2. Assuming a flat-ΛCDM (given from Eq. 1.67 when $\Omega_{r,0} = \Omega_{c,0} = 0$) cosmological model and using the measured values from Planck for Ω_m and the methodology described in Sec. 3.3.2, we retrieve a posterior for the Hubble constant that can be seen in Fig. 4.3 (blue curve) along with the 1 and

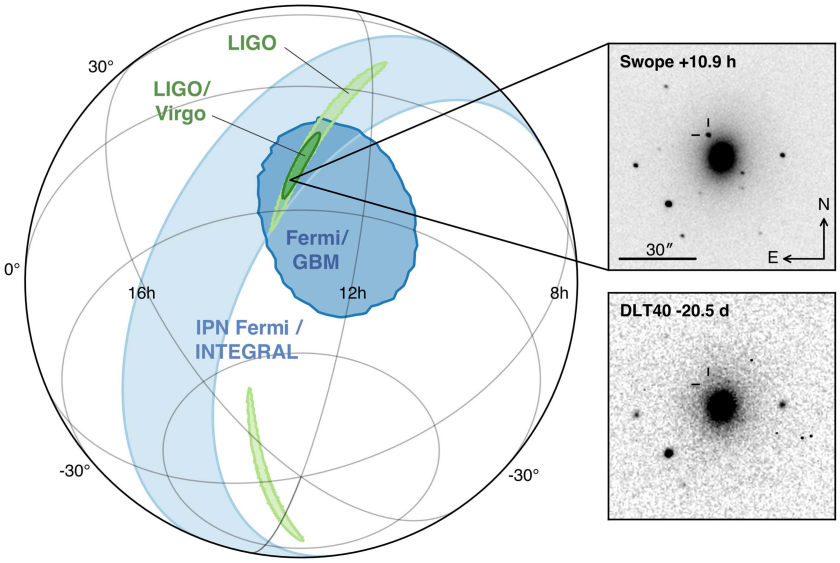

Figure 4.2: Left: The localization area of GW170817 on the sky using LIGO (wider green spots) only and LIGO-Virgo data (narrower green spot inside one of the two green spots obtained using only LIGO data). Top right: Image containg the location of the apparent host galaxy NGC 4993 10.9 hr after the merger. Bottom right: Image of the same region of the sky but 20.5 days before the merger. The plot was taken from Ref. [52].

2σ uncertainties that are depicted as vertical dashed and dotted blue lines. This gives an estimation of $H_0 = 70^{+12}_{-8}$ km/s/Mpc (maximum a posteriori and 68.3% confidence interval) [30]. In this plot, the vertical green and orange shaded regions indicate the measurements from Planck [5] and SHOES [6], along with their 1 and 2σ uncertainties.

Dark Sirens Analysis

For the rest of the GWTC-1 events, we do not have any EM counterpart detected. This means that we need to infer the redshift of the event statistically using a galaxy catalogue and the methodology that was described in Sec. 3.3.1 to estimate cosmological parameters. The galaxy catalogues that we used for this analysis were the GLADE version 2.4 [44] and the DES year 1 [60, 61].

GLADE is an all-sky galaxy catalogue ideal for GW sky area cross-correlation. It is a combination of different galaxy catalogues, namely the GWGC [62], 2MPZ [63], 2MASS XSC [64], HyperLEDA [65] and SDSS-DR12Q [66] catalogues. The number density of objects in the GLADE catalogue over the sky can be seen in Fig: 4.4. A clear

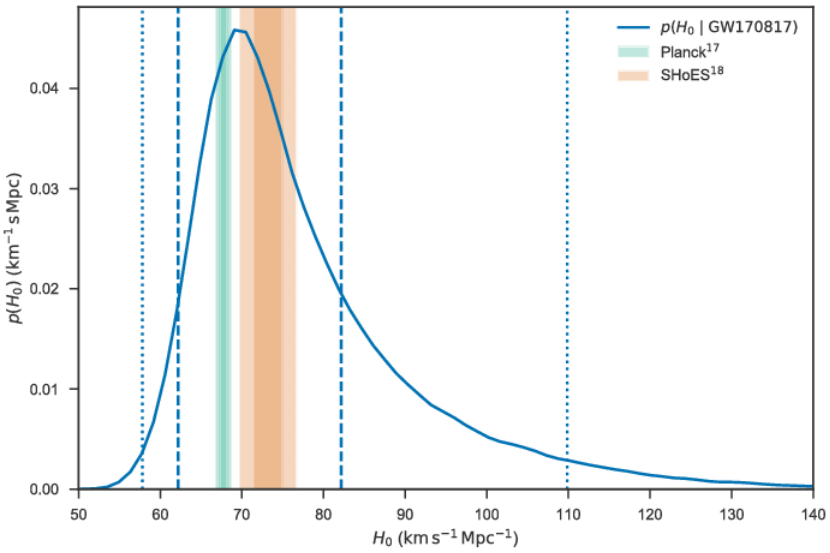

Figure 4.3: The Hubble constant posterior (blue curve) obtained from GW170817's data while using the identified host galaxy's NGC 4993 redshift, along with the 1 and 2σ uncertainties (vertical blue dashed and dotted lines). The estimated H_0 is 70^{+12}_{-8} km/s/Mpc (maximum a posteriori and 68.3% confidence interval). The vertical green and orange shaded regions indicate the measurements from Planck [5] and SHOES [6], along with their 1 and 2σ uncertainties. The plot was taken from Ref. [30].

reduction in the number density can be seen in the borders of the plots. This is because the galactic plane lies in this region and prevent us from seeing galaxies there. Due to GLADE being a combination of different galaxy catalogues with different sensitivities, we observe over- and under-densities in the numbers of objects. The GLADE catalogue is complete (in B-band luminosity) out to 37 Mpc and has an estimated completeness of 50% out to 91 Mpc. With the word bands astronomers refer to a section of light in the electromagnetic spectrum. More specifically, B band is the part of the visible spectrum with a filter with an effective wavelength midpoint of $\lambda_{\mathrm{eff}} = 445$ nm.

DES Year 1 is a survey mapping around 300 million galaxies. This galaxy catalogue has a sky coverage of around 5000 deg^2. In our analysis it was only used for the GW170814 event, which is a BBH with a small estimated sky area, since this was the only GW event where DES Year 1 covered a sufficient percentage of the estimated sky area. The public galaxy catalogue DES Year 1 that we used covers approximately 87% of GW170814's sky area. The area of the sky covered by DES Year 1 can be seen in Fig. 4.5, as a red shaded area. For this analysis we use the photometric redshifts which

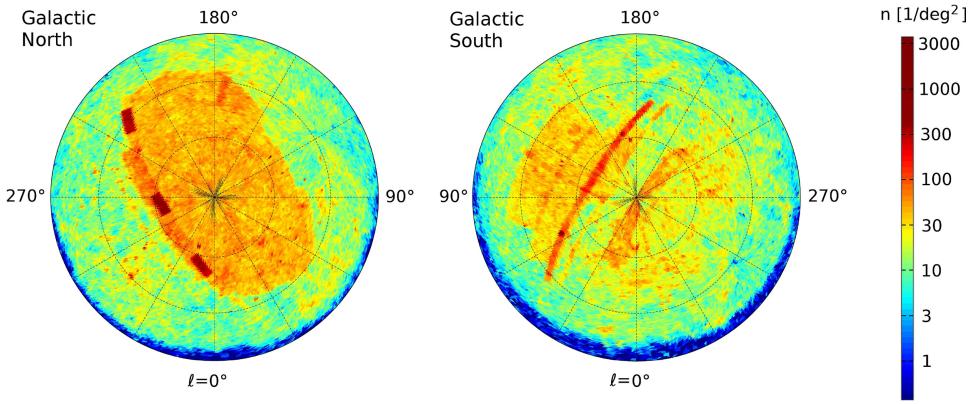

Figure 4.4: The number density of objects in the GLADE catalogue. The galactic plane obscures areas at the borders of the plots. The plots were taken from Ref. [44].

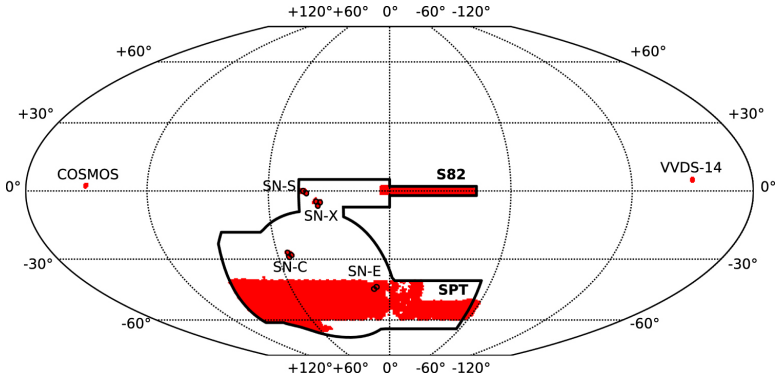

Figure 4.5: The sky area covered by the DES Year 1 galaxy catalogue depicted as a red shaded area over the sky. The plot was taken from Ref. [61].

are derived using the bayesian photometric redshift (BPZ) template fitting method [67]. It is worth noting that a similar analysis for GW170814 has been carried out at Ref. [43]. The authors have used DES Year 3 survey which encloses the full sky area of GW170814.

We use the methodology that was described in Sec. 3.3.1 and focus on the Hubble constant, while using a flat-ΛCDM cosmology model and fixing Ω_m to the value measured by Planck. All the galaxies from the galaxy catalogue that lie inside each event's estimated sky area are being used to get a statistical estimation for the redshift of the event. The sky areas of the events can be seen in Fig. 4.6. From the GLADE catalogue we selected the reported B-band luminosities to be used for luminosity weighting. The B-band luminosity Schechter function parameters that we used in this case are $\alpha = -1.07$ and $M^*(H_0) = -19.7 + 5\log_{10}(H_0/100)$ [68]. For GW170814 where DES was used, we converted the DES grizY magnitudes to the SDSS ugriz system using the photometric

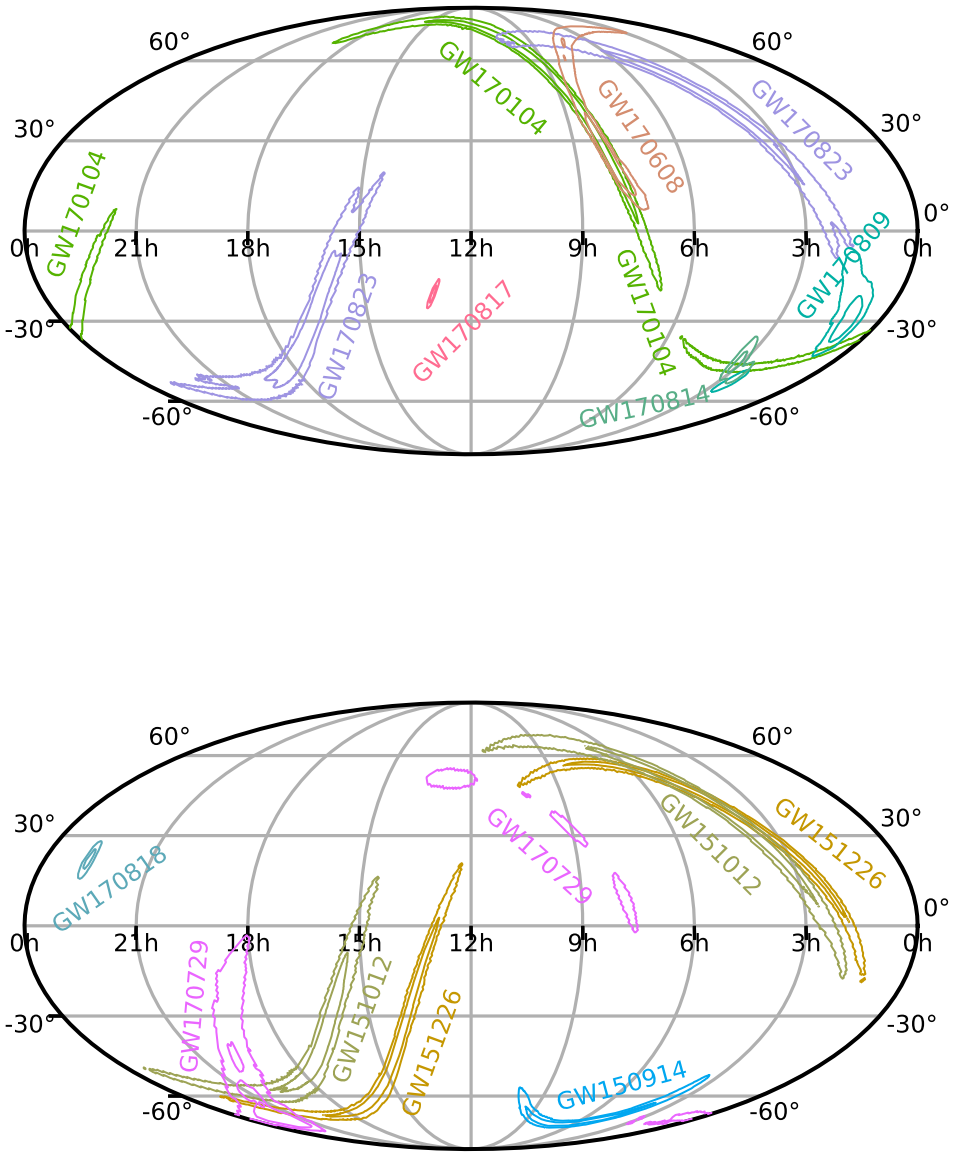

Figure 4.6: The estimated sky area of GWTC-1 events projected on the sky. The plots were taken from Ref. [49].

transformations provided in Ref. [60] and used the SDSS G-band magnitudes, as these are closest to B-band. G band is another part of the visible spectrum with a filter with an effective wavelength midpoint of $\lambda_{\text{eff}} = 464$ nm. The Schechter parameters of our

Event	SNR	$\Delta\Omega$	d_L/Mpc	$z_{\rm event}$	Catalog	$N_{\rm galaxies}$	$m_{\rm th}$	$p(G\|z, D_{\rm GW})$
GW150914	24.4	182	440^{+150}_{-170}	$0.09^{+0.03}_{-0.03}$	GLADE	3910	17.92	0.42
GW151012	10.0	1523	1080^{+550}_{-490}	$0.21^{+0.09}_{-0.09}$	GLADE	78195	17.97	0.01
GW151226	13.1	1033	450^{+180}_{-190}	$0.09^{+0.04}_{-0.04}$	GLADE	27677	17.93	0.41
GW170104	13.0	921	990^{+440}_{-430}	$0.20^{+0.08}_{-0.08}$	GLADE	42221	17.76	0.01
GW170608	15.4	392	320^{+120}_{-110}	$0.07^{+0.02}_{-0.02}$	GLADE	6267	17.84	0.60
GW170729	10.8	1041	2840^{+1400}_{-1360}	$0.49^{+0.19}_{-0.21}$	GLADE	77727	17.82	< 0.01
GW170809	12.4	308	1030^{+320}_{-390}	$0.20^{+0.05}_{-0.07}$	GLADE	18749	17.62	< 0.01
GW170814	16.3	87	600^{+150}_{-220}	$0.12^{+0.03}_{-0.04}$	DES-Y1	31554	23.84	> 0.99
GW170817	33.0	16	40^{+7}_{-15}	$0.01^{+0.00}_{-0.00}$	–	–	–	–
GW170818	11.3	39	1060^{+420}_{-380}	$0.21^{+0.07}_{-0.07}$	GLADE	1059	17.51	< 0.01
GW170823	11.5	1666	1940^{+970}_{-900}	$0.35^{+0.15}_{-0.15}$	GLADE	117680	17.98	< 0.01

Table 4.1: GWTC-1 events' parameters: network signal-to-noise ratio (SNR), 90% sky localization region $\Delta\Omega$ (deg^2), luminosity distance $d_{\rm L}$ (Mpc, median with 90% credible intervals), and estimated redshift $z_{\rm event}$ (median with 90% range assuming Planck cosmology). In the remaining columns we report the number of galaxies within each volume for the used galaxy catalogue, and the apparent magnitude threshold, $m_{\rm th}$, of the galaxy catalogue associated with the corresponding sky region. The final column gives the probability that the host galaxy is inside the galaxy catalogue for each event, $p(G|z_{\rm event}, D_{\rm GW})$, also evaluated at the median redshift for each event.

analysis were selected to be $\alpha = -0.89$ and $M^*(H_0) = -19.39 + 5\log_{10}(H_0/100)$. We

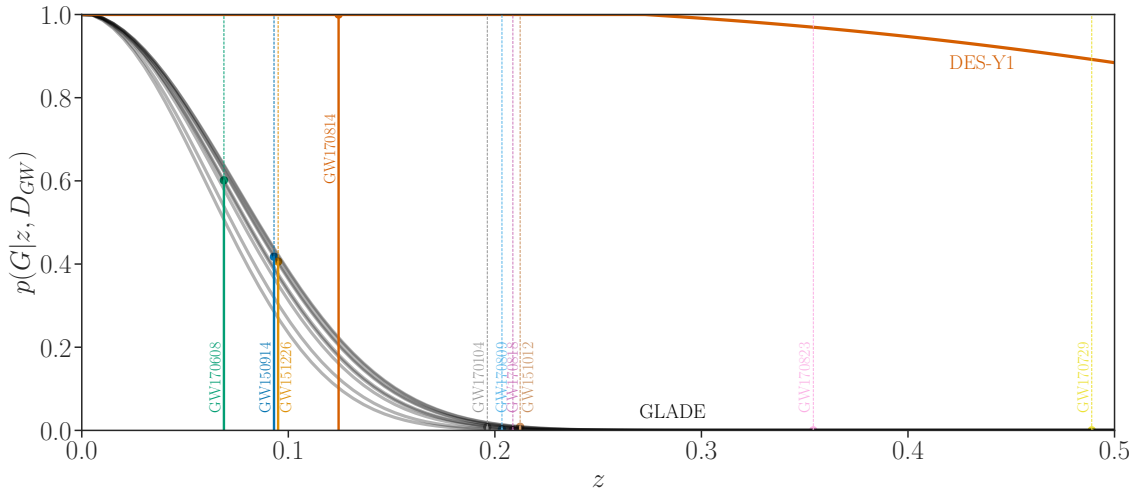

Figure 4.7: The probability of the host galaxy being inside the galaxy catalogue as a function of redshift [46]. For GW170814 the DES Year 1 catalogue (orange curve) has been used, while for the rest of the event we used the GLADE catalogue (gray curves). The vertical lines show the median redshift (assuming Planck cosmology) for each event as in Tab. 4.1.

calculated the apparent magnitude threshold that corresponds to each GW event's sky area and the probability that the host galaxy is inside the galaxy catalogue as described in the previous chapter. For each event, those can be seen in the last two columns of

Tab. 4.1, along with some other information for the events. In the last column, the probability that the host galaxy is inside the galaxy catalogue is evaluated at the median redshift of each event, whereas it can be seen as a function of redshift in Fig. 4.7.

The results from this analysis are shown in Ref. [46]. For the main result, in the case of BBHs, we chose a power law mass distribution for the calculation of the probability of detection $p(m_1) \propto m_1^{-\alpha}$, with a power law index of $\alpha = 1.6$ between 5 $M_\odot$ < m_1 < 100 $M_\odot$ in the source frame [69]. For the secondary mass we chose a uniform distribution within 5 $M_\odot$ < m_2 < m1. For the BNS, we used a Gaussian mass distribution with a mean of 1.35 $M_\odot$. The remaining GW parameters are marginalized over their natural distributions: uniform in the sky, uniform on the sphere for orientation, uniform in polarization, a distribution of merger rates that does not evolve with redshift $R(z)$ = constant, and an SNR larger than 12. We assigned a probability for each galaxy to be the host of a GW event that is proportional to their luminosity. The

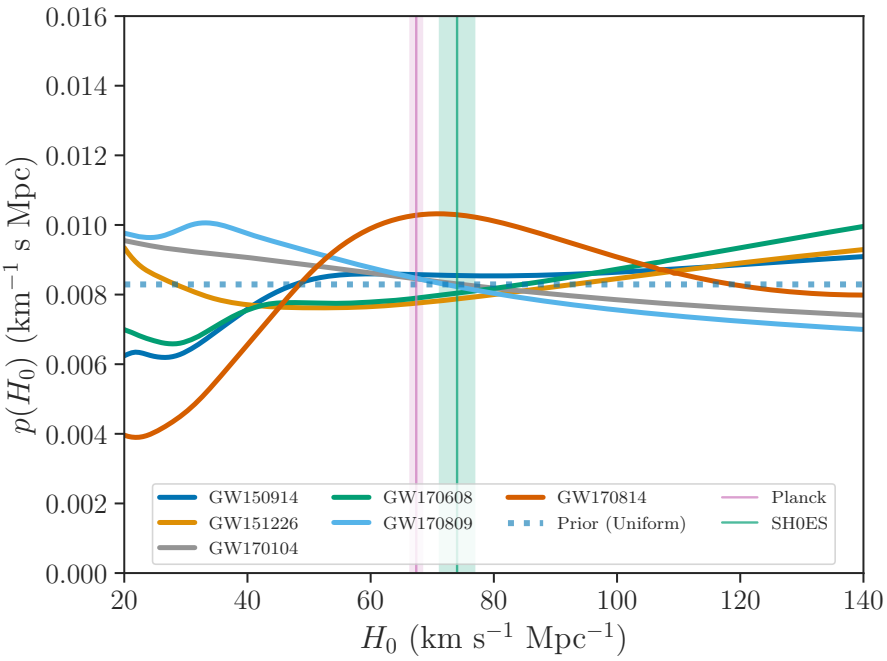

Figure 4.8: The H_0 posteriors from individual GWTC-1 events with SNR>12 [46]. Here we assumed a fixed power law for the distribution of $m_1^{-\alpha}$ with $\alpha = 1.6$ and a merger rate model that does not evolve with redshift. The vertical green and pink lines and shaded regions indicate the measurements from Planck and SHOES, along with their 1 and 2σ uncertainties.

individual posteriors of each event can be seen in Fig. 4.8, where a uniform H_0 prior

between $[20, 140]$ km/s/Mpc was selected. As expected, the most informative event is GW170814 where a more complete galaxy catalogue has been used. Combing all the individual posteriors we get the solid orange curve in Fig. 4.9. This gives an estimation of $H_0 = 69.6^{+20.4}_{-8.6}$ km/s/Mpc. The final result was produced by combining the contribution of the dark sirens with the result from GW170817. Our final combined result is shown in Fig. 4.9 as a solid blue curve, and gives an estimation of $H_0 = 68.7^{+17.0}_{-7.8}$ km/s/Mpc (the stated uncertainties refer to the 68.3% highest density posterior interval).

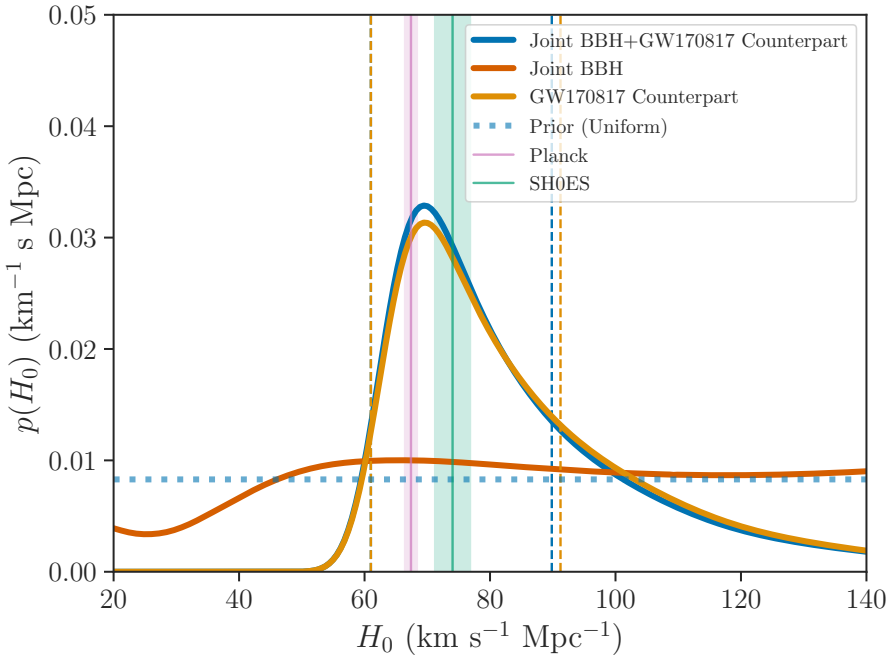

Figure 4.9: The combined H_0 posterior from GWTC-1 events with SNR>12 [46]. The solid red curve corresponds the dark sirens only posterior and gives an estimation of $H_0 = 69.6^{+20.4}_{-8.6}$ km/s/Mpc (68.3% highest density posterior interval). The solid orange curve is the result from GW170817 with the counterpart detection. The solid blue curve is the combination of the dark sirens and GW170817 and gives $H_0 = 68.7^{+17.0}_{-7.8}$ km/s/Mpc (68.3% highest density posterior interval). The 68% maximum a-posteriori intervals are indicated with the vertical dashed lines. The vertical green and pink lines and shaded regions indicate the measurements from Planck and SHOES, along with their 1 and 2σ uncertainties.

Fixing the mass distribution parameters brings a source of systematic uncertainties in the analysis. In Ref. [46] we explored the effects of varying the maximum allowed mass of the BHs, the $p(m_1)$ power law index, the merger rate model, the luminosity weighting of the galaxies and the SNR cut on the combined posterior. All of these can

be seen in Figs. 4.10 and 4.11. As it can be seen from the plots, the variations of the combined posterior in some cases are noticeable. This is an indication that population

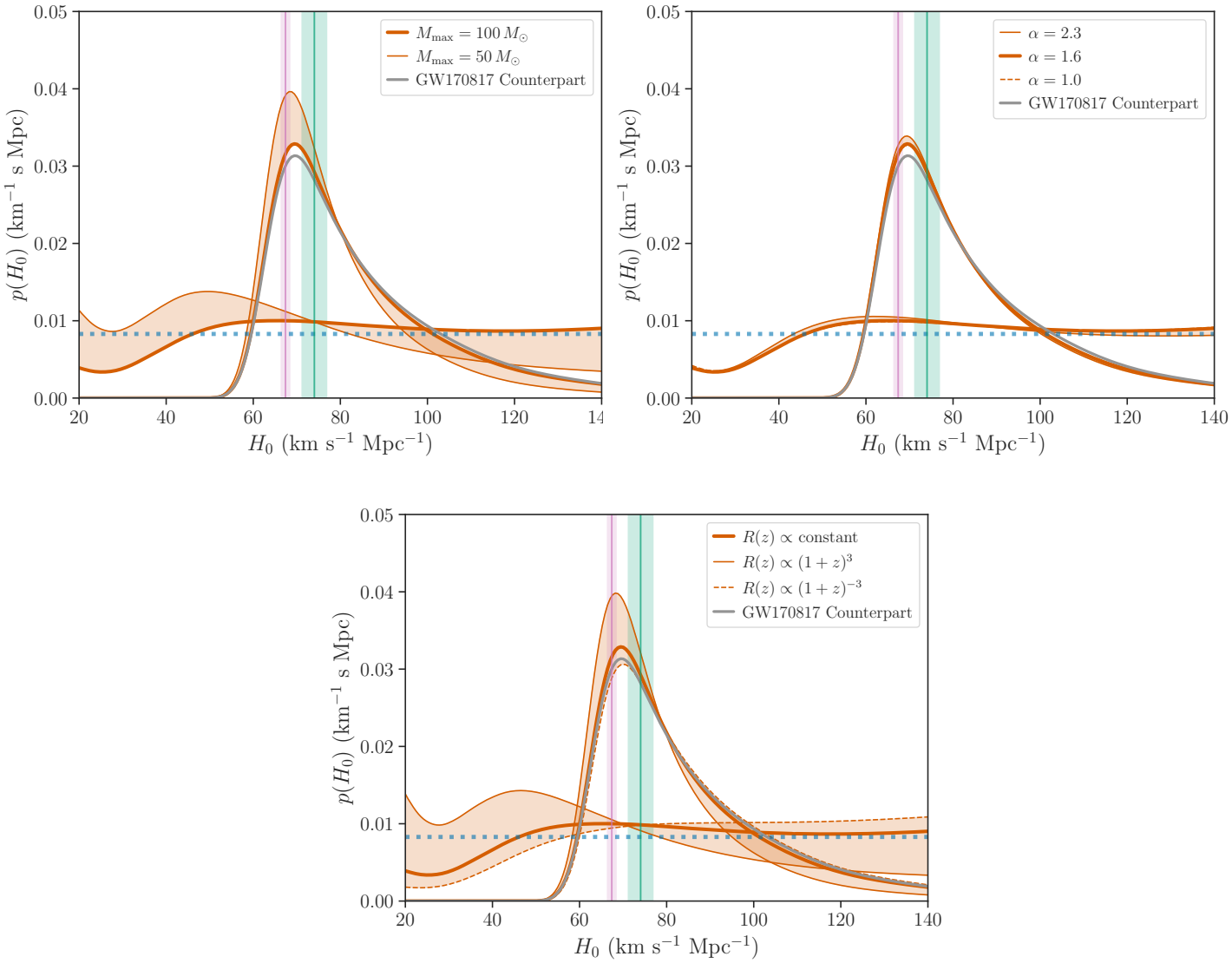

Figure 4.10: Exploring the systematic uncertainties for the GWTC-1 analysis [46]. Top left: Changing the maximum allowed mass of the BHs to $M_{max} = 50\ M_\odot$. This has a noticeable effect on the H_0 posterior. Top right: Varying the powelaw index of the m_1 distribution. Minimal changes in the posterior can bee seen in this case. Bottom: Changing the merger rate model. This has a noticeable effect on the H_0 posterior.

parameters affect the cosmology estimation and thus should be estimated conjointly. However, for the analysis of GWTC-1 events that was not yet very important. This is due to the fact that our combined posterior is driven mostly by GW170817's posterior, as do not have enough BBH events for the population parameters to affect the final

combined posterior significantly. This changed with the O3 run of LIGO-Virgo and, as we will see in the following sections, population parameters affect the estimation of cosmological parameters.

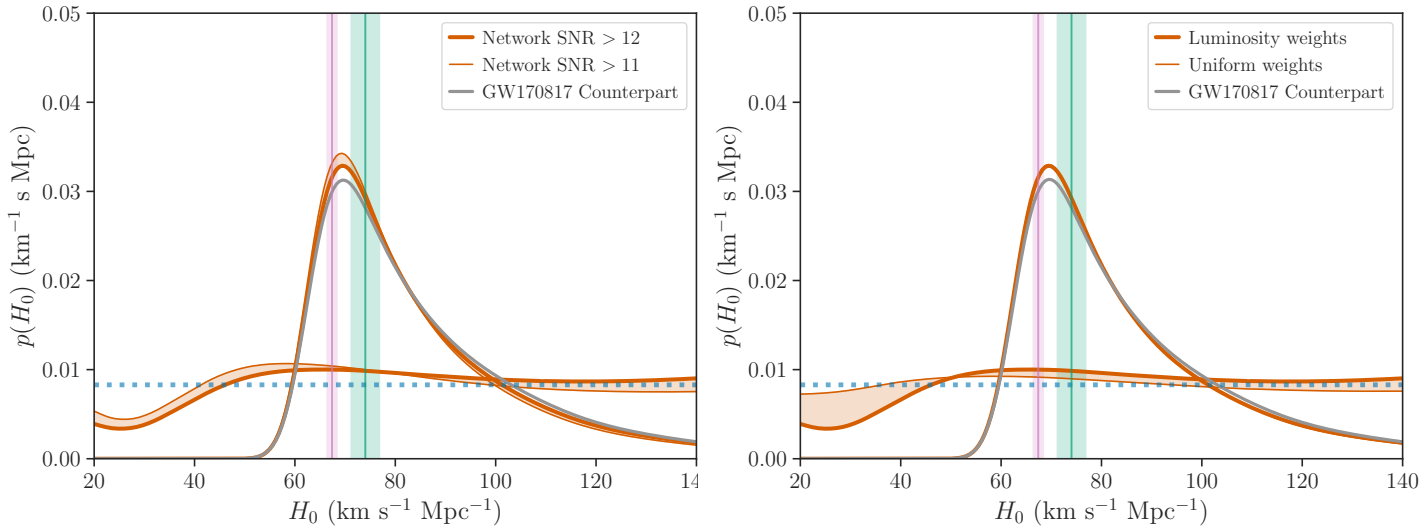

Figure 4.11: Exploring the systematic uncertainties for the GWTC-1 analysis [46]. Left: Varying the SNR cut. This has a small effect on the H_0 posterior. Right: removing the luminosity weighting of the galaxies. This has a minimal effect on the H_0 posterior.

4.1.3 Using Solely Gravitational Waves Data

As we have seen in the previous section, there are population parameters that affect the estimation of cosmological parameters. This is due to the fact that galaxy catalogues become empty relatively fast at the redshifts where GW events are detected. In the methodology of the previous section, this translates to the out-of-catalogue term becoming more significant than the in-catalogue term. The out-of-catalogue term carries information about the population assumptions that we have made. Ideally, population parameters and cosmological parameters should be estimated conjointly, as was described in Sec. 3.2.

A new methodology for the joint estimation was developed in Ref. [28] where events from GWTC-1 were reanalyzed. We focused on the H_0 tension region and used a uniform H_0 prior between $[67, 74]$ km/s/Mpc. We used again a merger model that does not evolve with redshift and a uniform distribution for m_2. We chose the same model for the

mass distribution of the heavy component m_1 (a power law), but allowed the power law index, the maximum M_{max} and the minimum M_{min} allowed masses to vary. With these settings, the maximum likelihood is reached at $H_0 = 69$ km/s/Mpc with the parameters $M_{min} = 8.6$ M$_\odot$, $M_{max} = 37.5$ M$_\odot$ and $\alpha = 2.2$.

The analysis of the previous section was repeated using those values for the population parameters. The results can be seen in Fig. 4.12. The dashed curves are the results from the previous sections. Fixing the population parameters to their most probable values

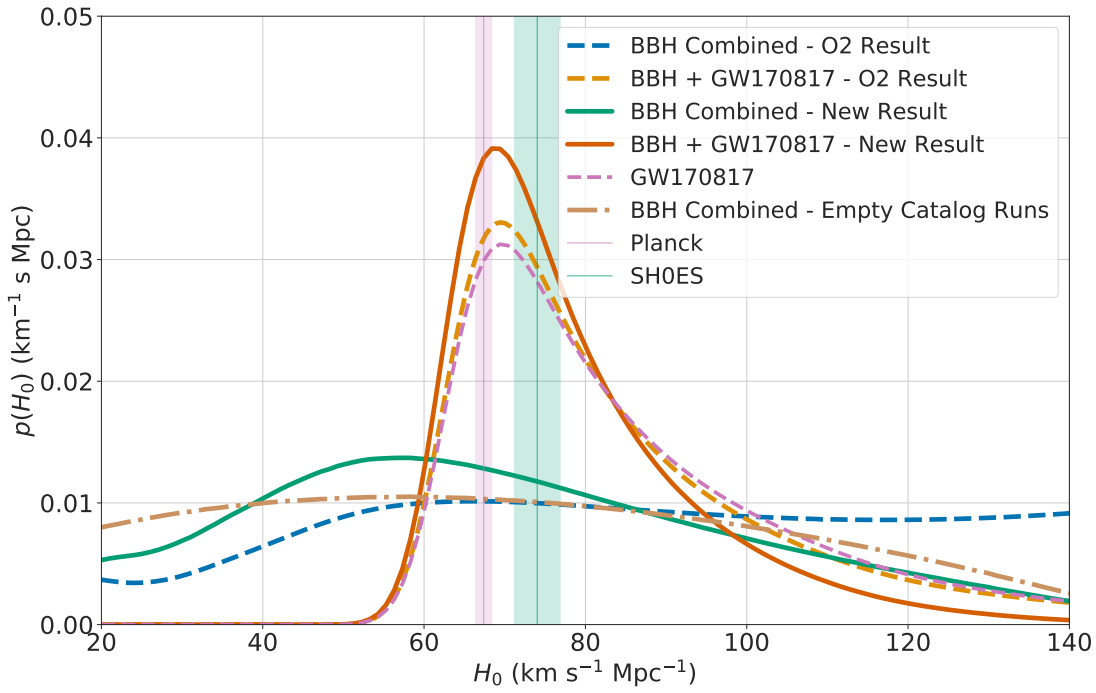

Figure 4.12: The reanalysis of GWTC-1 events with SNR>12 [28]. In this we again assumed a fixed power law for $m_1^{-\alpha}$ with $M_{min} < m_1 < M_{max}$, but we found the values of α, M_{max}, M_{min} that best fit the data. We used those values to reanalyze the events using the method described in Sec. 4.1.2. Dashed curves correspond to previous results. Solid curves are the new posteriors obtained by fixing the population parameters to the most probable values.

previously estimated changes the posteriors, with respect to the previous estimations. The new posteriors are shown in the plot as solid curves. The green solid curve corresponds to the dark sirens only result, whereas the orange solid curve corresponds to the final combined with GW170817 posterior. We get an estimation of $H_0 = 68^{+13}_{-7}$ km/s/Mpc whereas the previous result was $H_0 = 69.6^{+20.4}_{-8.6}$ km/s/Mpc. The new width is about 15% narrower; the H0 estimate is thus more informative in the tension region. In Fig. 4.12 the

posterior tails appear considerably reduced with the new choice of population parameters; this is not surprising, as the population parameters are chosen to maximize the likelihood in the central H_0 tension region.

4.2 Cosmological Inference From the Third GW Catalogue

The third observing run, O3, took place from 04/02/2019 up to 03/27/2020 with a break in between from 10/01/2019 to 01/11/2019. During this period, LIGO-Virgo detected a significant amount of CBC GW events [70, 71, 72], which along with the events from GWTC-1, constitute the third gravitational wave transient catalogue (GWTC-3). In this section we will use events from GWTC-3 and present the best cosmological constraints obtained from GW data analysis so far.

4.2.1 Third Gravitational Wave Transient Catalogue

GWTC-3 [72] is the latest and most updated catalogue with GW events. It contains in total 90 GW events originating from CBC. The majority of the events are BBHs, but GWTC-3 also contains some BNS and NSBH events. The 90% credible contours of estimated mass ratios versus estimated total masses of the final BHs can be seen in Fig. 4.13. In these plots the dotted lines distinguish between regions in the parameter space of the individual masses of the events. The first is the $m_1 = 3\ \mathrm{M}_\odot$. Events that are to the left of this line have $m_1 < 3\ \mathrm{M}_\odot$, so they are possibly neutron star binaries. The second is the line $m_2 = 3\ \mathrm{M}_\odot$. Events that are below this line have $m_2 < 3\ \mathrm{M}_\odot$, so the light component of the binary is possibly a neutron star.

4.2.2 Using Solely Gravitational Waves Data

We use the same methodology as in the previous section to infer the mass distribution and merger rate parameters that best fit the data. As mass distributions for m_1, we tested various models, following Ref. [73], trying to identify the one that best fit the data while varying cosmological parameters. The first distribution that we considered was a simple truncated power law model between M_{min} and M_{max} with power index α.

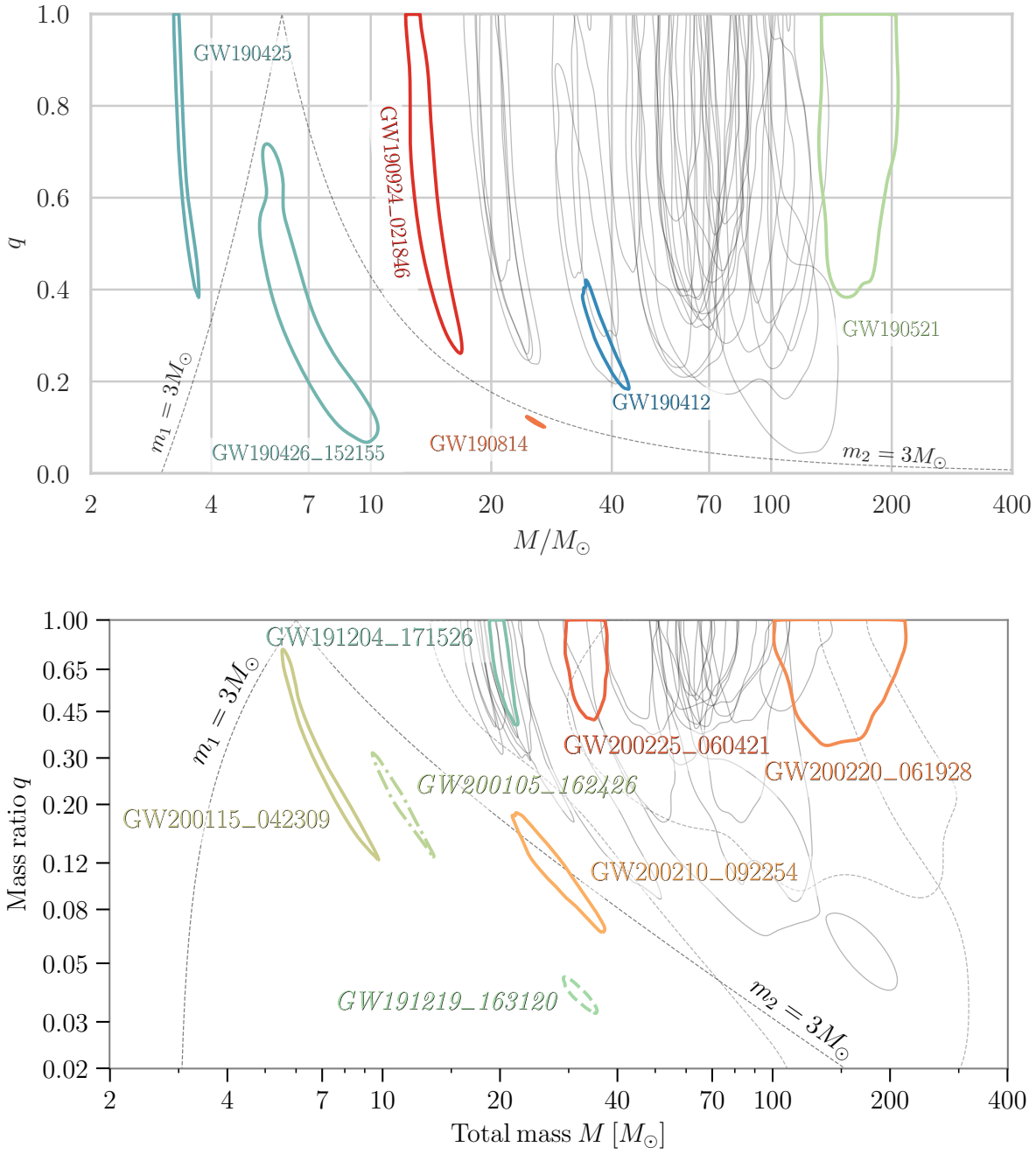

Figure 4.13: The 90% credible contours of estimated mass ratios versus the estimated total masses of the final BHs. The top plot includes the events of the O3a run (first half of the O3 run) and the bottom plot includes events of the O3b run (second half of the O3 run). Events that are to the left of the dotted $m_1 = 3$ M$_\odot$ line have $m_1 < 3$ M$_\odot$, so they are possibly neutron star binaries. Events that are below the dotted $m_2 = 3$ M$_\odot$ line have $m_2 < 3$ M$_\odot$, so the light component of the binary is possibly a neutron star. The plots were taken from Refs. [70, 72].

In this case the set of mass distribution parameters is $\Lambda_{m_1} = \{M_{min}, M_{max}, \alpha\}$ and:

$$p_{PL}(m_1|M_{max}, M_{min}, \alpha)_{\propto} \begin{cases} m_1^{-\alpha} & M_{min} < m_1 < M_{max} \\ 0 & \text{otherwise} \end{cases} . \tag{4.1}$$

The second distribution that we selected to test was a broken power law distribution with two power law indexes a_1, a_2 and a breaking point at some value $m_{break} = M_{min} + b(M_{max} - M_{min})$. We also introduced a tapering factor δ_m that smooths the lower end of the distribution. In this case we have $\Lambda_{m_1} = \{M_{min}, M_{max}, \alpha_1, \alpha_2, b, \delta_m\}$ and:

$$p_{BPL}(m_1|M_{max}, M_{min}, \alpha_1, \alpha_2, b, \delta_m) \propto S(m_1|M_{min}, \delta_m) \times \begin{cases} m_1^{-\alpha_1} & M_{min} < m_1 < m_{break} \\ m_1^{-\alpha_2} & m_{break} < m_1 < M_{max} \\ 0 & \text{otherwise} \end{cases} , \tag{4.2}$$

where:

$$S(m_1|M_{min}, \delta) = \begin{cases} 0 & m_1 < M_{min} \\ f(m_1 - M_{min}, \delta_m) & M_{min} < m_1 < M_{min} + \delta_m \\ 1 & m_1 > M_{min} + \delta_m \end{cases} , \tag{4.3}$$

is the smoothing function with $f(m, \delta_m) = [1 + \exp(\frac{\delta}{m} + \frac{\delta}{m - \delta})]^{-1}$. The last model that we tested was a distribution of a power law superimposed with a Gaussian peak distribution with mean μ_g and width σ_g. Here we need an additional parameter that controls the fraction of the Gaussian peak with respect to the power law λ_g. We use again the tapering factor and in this case we have $\Lambda_{m_1} = \{M_{min}, M_{max}, \alpha, \mu_g, \sigma_g, \lambda_g, \delta_m\}$

and:

$$p_{PLG}(m_1|M_{min}, M_{max}, \alpha, \mu_g, \sigma_g, \lambda_g, \delta_m) \propto$$
$$S(m_1|M_{min}, \delta_m) \times \begin{cases} (1-\lambda_g)p_{PL}(m_1|M_{max}, M_{min}, \alpha) + \lambda_g G(m_1|\mu_g, \sigma_g) & M_{min} < m_1 < M_{max} \\ 0 & \text{otherwise} \end{cases}, \tag{4.4}$$

where:

$$G(m_1|\mu_g, \sigma_g) = \frac{1}{\sigma_g\sqrt{2\pi}} \exp(-\frac{(m_1-\mu_g)^2}{2\sigma_g^2}). \tag{4.5}$$

The mass distribution for m_2 was always set to a power law with power index β for $M_{min} < m_2 < m_1$. So $\Lambda_{m_2} = \{\beta\}$ and the full set of mass distribution parameters is $\Lambda_m = \Lambda_{m_1} \cup \Lambda_{m_2}$. For the merger rate model we used the distribution of Eq. 3.11. Consequently, the merger rate parameters are $\Lambda_R = \{z_p, \gamma, \kappa, R_0\}$. For cosmology models we considered two cases. The first is a flat-ΛCDM model with a Hubble constant prior focused on the tension region [65, 77] km/s/Mpc and a fixed Ω_m to the value measured by Planck. The second is a flat-w_0CDM model in which the density of the dark energy is allowed to evolve with redshift with $\Omega_{DE}(z) = \Omega_{\Lambda,0}(1+z)^{3(1+w_0)}$ with wide priors on $H_0,\ \Omega_m,\ w_0$. Notice here that the ΛCDM is retrieved from the w_0CDM when $w_0 = -1$. Therefore, the set of cosmological parameters is $\Lambda_c = \{H_0,\ \Omega_m,\ w_0\}$. The priors used for each model can be seen in Tabs. 4.2, 4.3 and 4.4. For this analysis we used all BBH events with SNR>11 (42 in total). The observed detector frame distribution of masses and distances can be seen in Fig. 4.14. In the same plots the mass distributions in the source frame of the events assuming a Planck cosmology are shown.

The Bayesian methodology described in Sec. 3.2 allows for the calculation of the Bayes factor, which can be used for the identification of the most favorable model supported by the data. That way, by running with different combinations of the mass and cosmology models that were described above we can find the combination that best fits the data. The results can be seen in Tabs. 4.5 and 4.6.

The first table shows the logarithms of the Bayes factors for the various mass models but assuming the different cosmological models that were described above (ΛCDM with

Truncated power law

Parameter	Description	Prior
α	Spectral index for the power law of the primary mass distribution.	$\mathcal{U}(1.5, 12)$
β	Spectral index for the power law of the mass ratio distribution.	$\mathcal{U}(-4, 12)$
M_{min}	Minimum mass of the power law component of the primary mass distribution.	$\mathcal{U}(2\,M_\odot, 10\,M_\odot)$
M_{max}	Maximum mass of the power law component of the primary mass distribution.	$\mathcal{U}(50, M_\odot, 200, M_\odot)$

Power law+Gaussian

Parameter	Description	Prior
α	Spectral index for the power law of the primary mass distribution.	$\mathcal{U}(1.5, 12)$
β	Spectral index for the power law of the mass ratio distribution.	$\mathcal{U}(-4, 12)$
M_{min}	Minimum mass of the power law component of the primary mass distribution.	$\mathcal{U}(2\,M_\odot, 10\,M_\odot)$
M_{max}	Maximum mass of the power law component of the primary mass distribution.	$\mathcal{U}(50\,M_\odot, 200\,M_\odot)$
$\lambda_{\rm g}$	Fraction of the Gaussian component in the model.	$\mathcal{U}(0, 1)$
$\mu_{\rm g}$	Mean of the Gaussian component in the primary mass distribution.	$\mathcal{U}(20\,M_\odot, 50\,M_\odot)$
$\sigma_{\rm g}$	Width of the Gaussian component in the primary mass distribution.	$\mathcal{U}(0.4\,M_\odot, 10\,M_\odot)$
δ_m	Range of mass tapering at the lower end of the mass distribution.	$\mathcal{U}(0\,M_\odot, 10\,M_\odot)$

Broken power law

Parameter	Description	Prior
α_1	Power law slope of the primary mass distribution for masses below m_{break}.	$\mathcal{U}(1.5, 12)$
α_2	Power law slope for the primary mass distribution for masses above m_{break}.	$\mathcal{U}(1.5, 12)$
β	Spectral index for the power law of the mass ratio distribution.	$\mathcal{U}(-4, 12)$
M_{min}	Minimum mass of the power law component of the primary mass distribution.	$\mathcal{U}(2\,M_\odot, 10\,M_\odot)$
M_{max}	Maximum mass of the primary mass distribution.	$\mathcal{U}(50\,M_\odot, 200\,M_\odot)$
b	The fraction of the way between M_{min} and M_{max} at which the primary mass distribution breaks.	$\mathcal{U}(0,1)$
δ_m	Range of mass tapering on the lower end of the mass distribution.	$\mathcal{U}(0\,M_\odot, 10\,M_\odot)$

Table 4.2: The mass parameters considered and the priors used for each of them. The symbol $\mathcal{U}$ indicates a uniform prior between the specified range.

Parameter	Description	Prior
R_0	BBH merger rate today in $\mathrm{Gpc}^{-3}\ \mathrm{yr}^{-1}$	$\mathcal{U}(0, 100)$
γ	Slope of the powerlaw regime for the rate evolution before the point z_p	$\mathcal{U}(0, 12)$
k	Slope of the powerlaw regime for the rate evolution after the point z_p	$\mathcal{U}(0, 6)$
z_p	Redshift turning point between the powerlaw regimes with γ and k	$\mathcal{U}(0, 4)$

Table 4.3: The rate parameters considered and the priors used for them. The symbol $\mathcal{U}$ indicates a uniform prior between the specified range.

Restricted priors (H_0-tension)

Parameter	Description	Prior
H_0	Hubble constant expressed in $\mathrm{km\,s^{-1}\,Mpc^{-1}}$ in the H_0-tension region.	$\mathcal{U}(65, 77)$
$\Omega_{\mathrm{m},0}$	Present-day matter density of the Universe fixed to the mean value inferred from measurements of the CMB.	0.3065
w_0	Dark energy equation of state parameter fixed to the value that corresponds to a constant density.	-1

Wide priors

Parameter	Description	Prior
H_0	Hubble constant expressed in $\mathrm{km\,s^{-1}\,Mpc^{-1}}$	$\mathcal{U}(10, 200)$
$\Omega_{\mathrm{m},0}$	Present-day matter density of the Universe.	$\mathcal{U}(0, 1)$
w_0	Dark energy equation of state parameter.	$\mathcal{U}(-3, 0)$

Table 4.4: The cosmological parameters considered and the priors used for them. The symbol $\mathcal{U}$ indicates a uniform prior between the specified range.

Mass model	$\log_{10}\mathcal{B}$
Truncated power law	0.2
Power law+Gaussian	-0.3
Broken power law	-0.4

Table 4.5: Logarithm of the Bayes factor comparing runs for which the same mass model distribution was assumed but different cosmological parameters priors. The cosmological priors that we chose were two different sets: a set of wide priors (for a general w_0CDM cosmology) versus a set of restricted priors (centered around the H_0 tension region).

restricted priors vs w_0CDM with wide priors). As it can be seen, the data do not show any preference in supporting any of the cosmological models considered in the analysis. As we will see later, this is because the posteriors on Ω_m and w_0 are not constrained by the GW observations and the error on the H_0 estimation extends beyond

Mass model	$\log_{10}\mathcal{B}$
Truncated power law	-1.9
Power law+Gaussian	0.0
Broken power law	-0.5

Table 4.6: Logarithm of the Bayes factor between the different mass models and the power law+Gaussian model preferred by the data, for the case of a w_0CDM cosmology with wide priors.

the tension region. The second table shows the logarithms of the Bayes factors for the same cosmological model (w_0CDM) but different mass models, with respect to the preferred model which is the power law+Gaussian. We find that, even if we allow the cosmological parameters to vary with wide priors, the truncated model is still strongly disfavored with respect to the power law+Gaussian and broken power law models, by a factor of 100. This result is consistent with the fact that, as indicated in Fig. 4.14, the source mass distribution contains more structure than a simple truncated power law model. We do not find any strong evidence to prefer the power law+Gaussian model over the broken power law model. However, there is a mild preference that makes the power law+Gaussian model the model that can fit the data best.

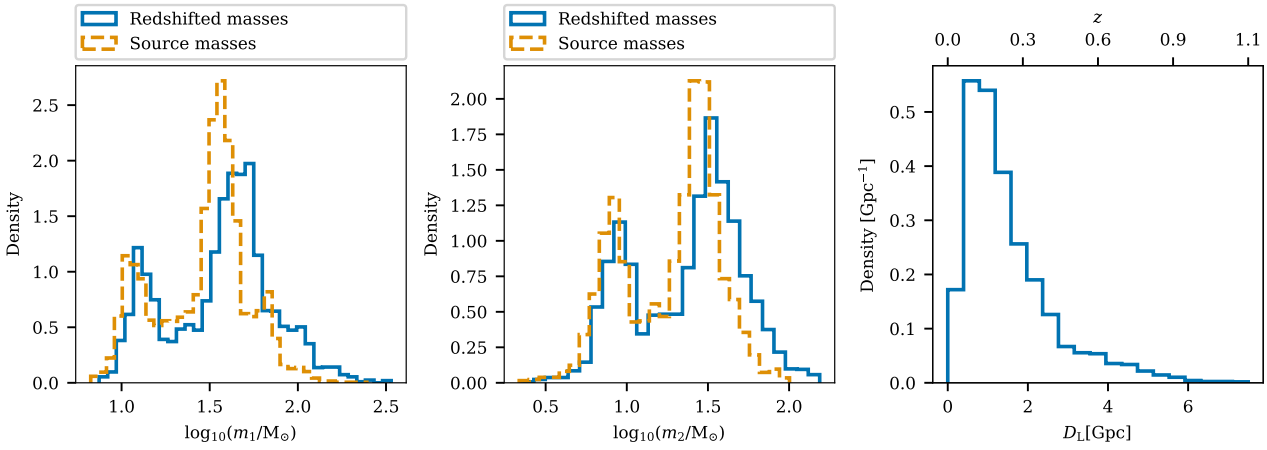

Figure 4.14: The observed detector distribution of masses and distances of the 42 BBH events with SNR>11 [74]. The mass distributions in source frame and the redshifts of the events assuming a Planck cosmology can be seen.

The marginal cosmological parameters posteriors that we obtained in the case of the wide prior cosmological model, for the three mass models considered, can be seen in Fig. 4.15. As it evident from the plots, the current BBH GW events can not sufficiently

constrain the values of the cosmological parameters, as we retrieved broad and/or uninformative posteriors. More specifically, in the case of the Hubble constant, for the

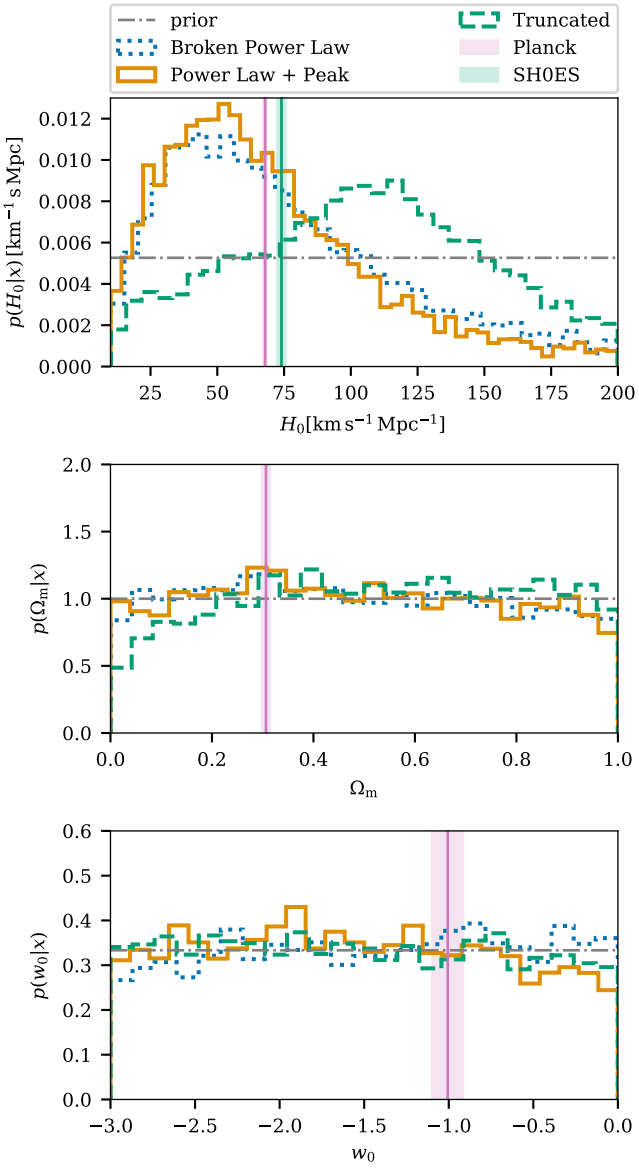

Figure 4.15: Top: The H_0 posterior. Middle: The Ω_m posterior. Bottom: The w_0 posterior. In each panel the different curves indicate the three mass models [74]. The solid orange line identifies the preferred power law+Gaussian model.

power law+Gaussian model we estimated $H_0 = 50^{+37}_{-30}$ km/s/Mpc, while for the broken power law model $H_0 = 44^{+52}_{-24}$ km/s/Mpc. The constraints on H_0 arise from the fact that these models are capable of fitting an excess of BBHs with masses around 35 $M_\odot$, which sets a scale for the redshift distribution of BBHs. This excess in mass distribution

of BHs sets a characteristic source mass scale, which informs $H(z)$ and excludes higher values of H_0. This effect can be also seen in Fig. 4.16, where we present the posterior of H_0 in the case of the most preferred mass model, along with the posteriors of the parameters found to correlate the most with the H_0 estimation. Those parameters are the mean of the Gaussian peak μ_g, the maximum allowed mass M_{max} and the power index γ of the merger rate model. As it can be seen, the H_0 estimation is driven from the μ_g parameter position. Here we retrieve $\mu_g = 32^{+6}_{-8}\ M_\odot$.

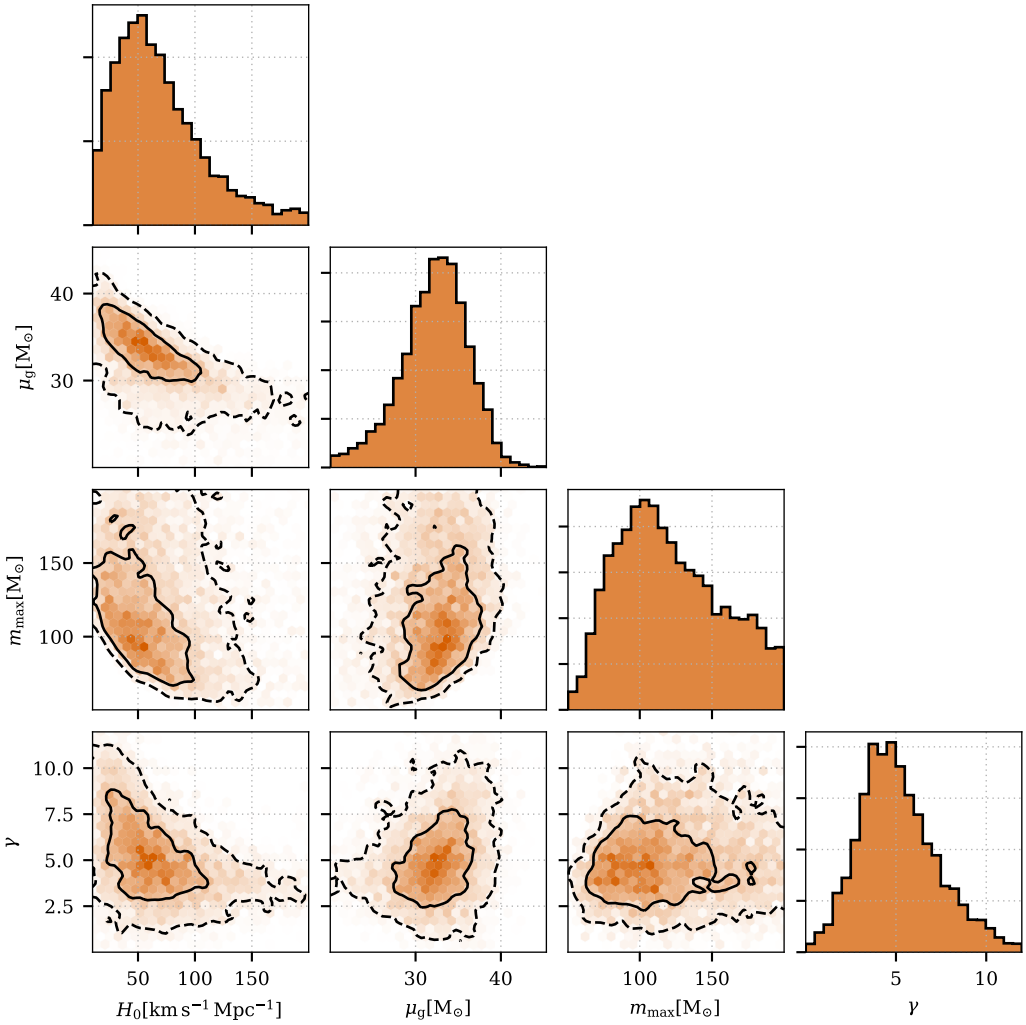

Figure 4.16: Posteriors of H_0 and the population parameters μ_g, M_{max}, and γ, as we found those to be the ones that correlate the most with H_0. The population parameters mentioned are the position of the Gaussian peak, the upper end of the mass distribution and the merger rate evolution power law index, respectively [74]. The solid and dashed black lines indicate the 50% and 90% credible levels contours.

On the other hand, the disfavoured truncated power law model supports higher H_0 values. This result is due to the fact that the truncated power law model is not able to adequately fit the presence of massive binaries while producing an excess of BBHs with masses around $40M_\odot$ in the detector frame. For this reason, higher H_0 values are more supported since those values place events at higher redshifts, thus reducing their source masses.

In Fig. 4.17 we combine the H_0 posteriors that we calculated from the three mass models with the GW170817 posterior. From there we find a value of $H_0 = 68^{+12}_{-8}$ km/s/Mpc for the power law+Gaussian model and $H_0 = 68^{+13}_{-8}$ km/s/Mpc for the broken power law model, which represent an improvement of 17% and 12%, respectively with respect to the result presented in the previous section. For the truncated power law model, we obtain $H_0 = 69^{+21}_{-8}$ km/s/Mpc.

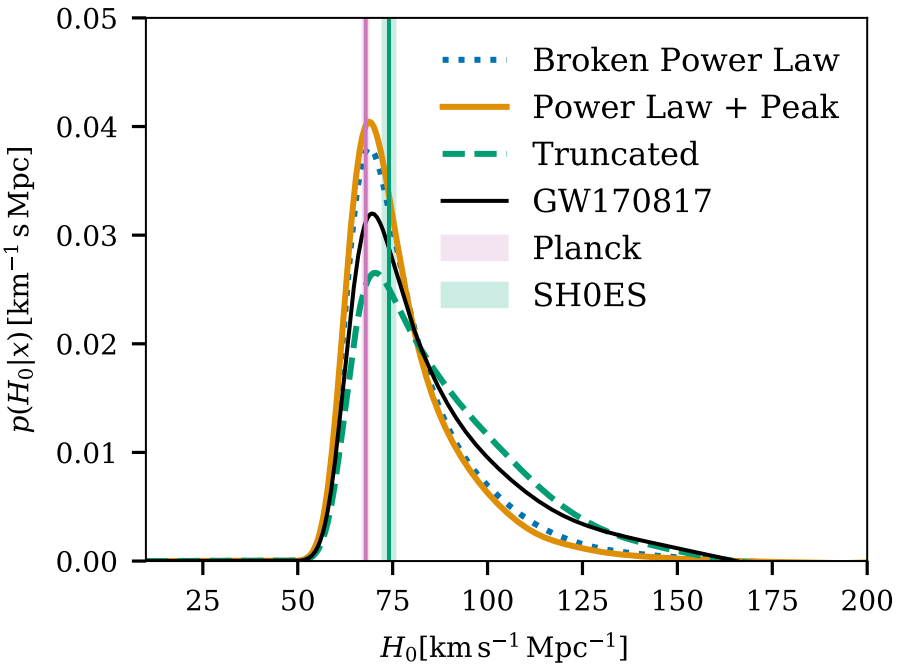

Figure 4.17: Posteriors of H_0 obtained by combining the H_0 posteriors from the 42 events for the different mass model distributions considered with the H0 posterior inferred from GW170817 [74].

4.2.3 Using Galaxy Catalogue Information

We will present here results following the methodology described in Sec. 3.3.3, which can be found in Ref. [74]. We used the GLADE+ galaxy catalogue [75] which is an extended version of the GLADE galaxy catalogue. In addition to GLADEv2.4, GLADE+ incorporates also WISExSCOSPZ [76] and a more advanced version of SDSS-DR16Q [77]. It contains about 22 million galaxies and its number density of objects over the sky can be seen in Fig. 4.18. GLADE+ is complete up to luminosity distances of around 47 Mpc in terms of the total expected B-band luminosity of galaxies. It contains all the brightest galaxies giving 90% of the total B-band and K-band luminosity up to 130 Mpc. In Fig. 4.19 the completeness of GLADE+ in terms of the normalized integrated B-band luminosity of galaxies compared to the that of GLADEv2.4 and WISExSCOSPZ can be seen as a function of luminosity distance. As it is apparent, GLADE+ is more complete with respect to the previous version GLADEv2.4 due to the inclusion of WISExSCOSPZ. For the main result of the analysis, we used all galaxies with measured

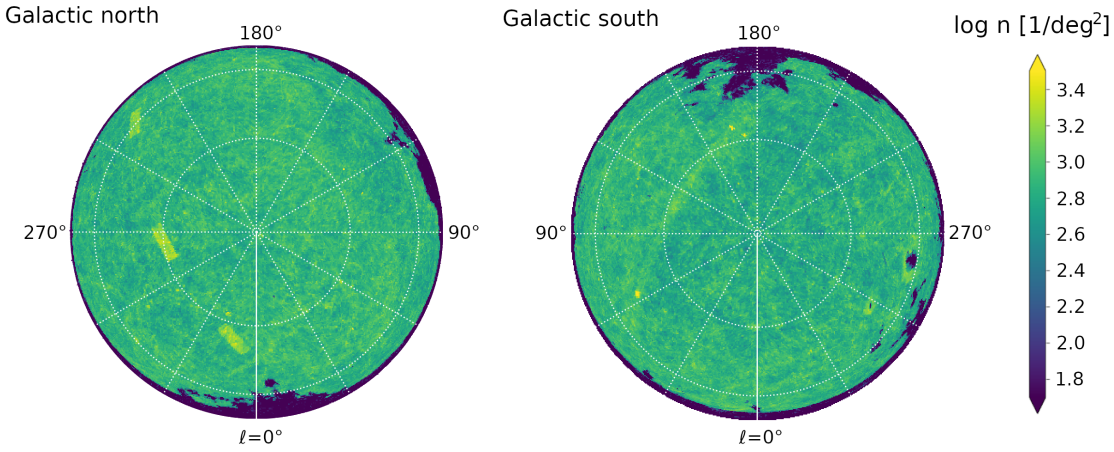

Figure 4.18: The base-10 logarithm of the number density of objects in GLADE+ over the sky. The plot was taken from Ref. [75].

K_s–band (denoted as K–band henceforth) luminosity, which is in the infrared region of the electromagnetic spectrum, and assigned a probability for each galaxy to host a GW event that is proportional to its K-band luminosity. However, we also explored the variation of the results when we change band and use the B_J-band instead. We

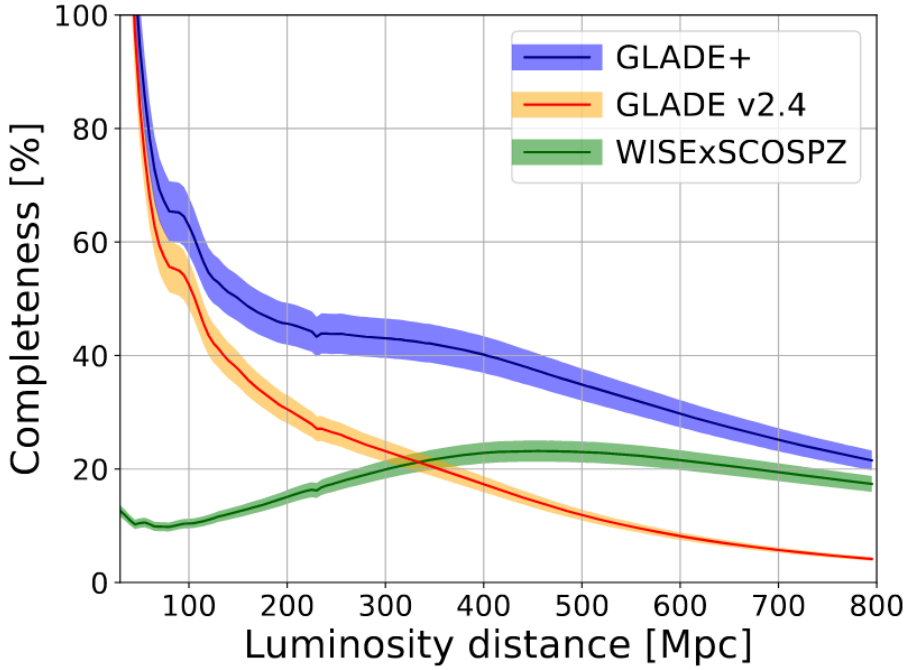

Figure 4.19: The calculated completeness of GLADE+ (blue curve) integrated in the B-band luminosity of galaxies. The completeness of GLADEv2.4 (orange curve) and WISExSCOSPZ (green curve) can also be seen. It is apparent from this plot that GLADE+ is more complete in larger distances than GLADEv2.4 due to the inclusion of WISExSCOSPZ. The plot was taken from Ref. [75].

assumed that the K–band absolute magnitude distribution for GLADE+ galaxies is well described by a Schechter function with parameters (reported for $H_0 = 100$ km/s/Mpc) $M_{*,K} = -23.39$ and $a_K = -1.09$ [78], while for the B_J–band we used $M_{*,B_J} = -19.66$ and $a_{B_J} = -1.21$ [79]. We set a bright cut-off high enough to include all the bright galaxies supported by the Schechter function: $M_{min,K} = -27.00$ and $M_{min,B_J} = -22.00$. Finally, we consider all the galaxies no fainter than $M_{max,K} = -19.0, M_{max,B_J} = -16.5$.

As we discussed, the methodology that we used here is a pixel based analysis. For all events, apart from GW190814, we carried out the analysis using a pixel size of 3.35 deg^2, while for GW190814 we used a pixel size of 0.2 deg^2 since the sky localization for this event was 10 times smaller than most of the others. In each pixel the apparent magnitude threshold m_{thr} was calculated as the median of the apparent magnitudes of all galaxies inside that pixel. In Fig. 4.20 the estimated sky areas of all events considered in this analysis can be seen, as well as the directional dependence of the K–band m_{thr}

for the GLADE+ galaxies. The apparent magnitude threshold calculated for each pixel is shown with a colorbar. Outside of the galactic plane, $m_{thr} \sim 13.5$ on average for the K–band, while within the galactic plane region m_{thr} is significantly lower. The completeness fraction, which is the probability that the galaxy catalogue contains the host galaxy of the GW event, $P(G|z, H0)$, is defined as the fraction of galaxies with absolute magnitudes brighter than the absolute magnitude threshold:

$$P(G|z, H_0) = \frac{\int_{L_{\rm thr}(m_{\rm thr},z,H_0)}^{L_{\rm max}} \phi(L) L \mathrm{d}L}{\int_{L_{\rm min}}^{L_{\rm max}} \phi(L) L \mathrm{d}L}, \tag{4.6}$$

where $\phi(L)$ is the Schechter function and $L_{min},\ L_{max}$ are the luminosities that correspond to absolute magnitude limits $M_{min},\ M_{max}$. The K-band and $\mathrm{B_J}$-band completeness fraction for GLADE+ can be seen in Fig. 4.21 as a function of redshift. The GLADE+ catalog is less complete in the K–band than in the B_J–band, but we decided to use the K–band data for our main results as they are better described by the Schechter function assumed.

In this analysis we used the 42 BBH detections used also in the previous section, but additionally we used GW190814 [80], the two BNS events GW170817 and GW190425 [81], and the two NSBH events GW200105 and GW200115 [82]. The mass distribution for the BHs was fixed to the one found to be the most preferred result of the previous section, the power law+Gaussian. The values for the parameters of the mass model and the merger rate model were kept fixed at the median values obtained from the previous analysis. More specifically, for the rate evolution we used $\gamma = 4.59,\ \kappa = 2.86,\ z_p = 2.47$ and for the mass model parameters we used $\alpha = 3.78,\ \beta = 0.81,\ M_{max} = 112.5M_\odot,\ M_{min} = 4.98M_\odot,\ \delta_m = 4.8M_\odot,\ \mu_g = 32.27M_\odot,\ \sigma_g = 3.88M_\odot$ and $\lambda_g = 0.03$. For the NS source mass model we considered again a uniform distribution between $M_{min} = 1M_\odot$ and $M_{max} = 3M_\odot$. We focused on H_0 and fixed the rest of the cosmological parameters to the values measured by Planck.

For many of the O3 events, the out-of-catalog term dominates the H_0 posterior. This is because most of the GW sources are placed at redshifts at which the completeness fraction of GLADE+ is low, as can also be seen in Fig. 4.22 where the H_0 posteriors

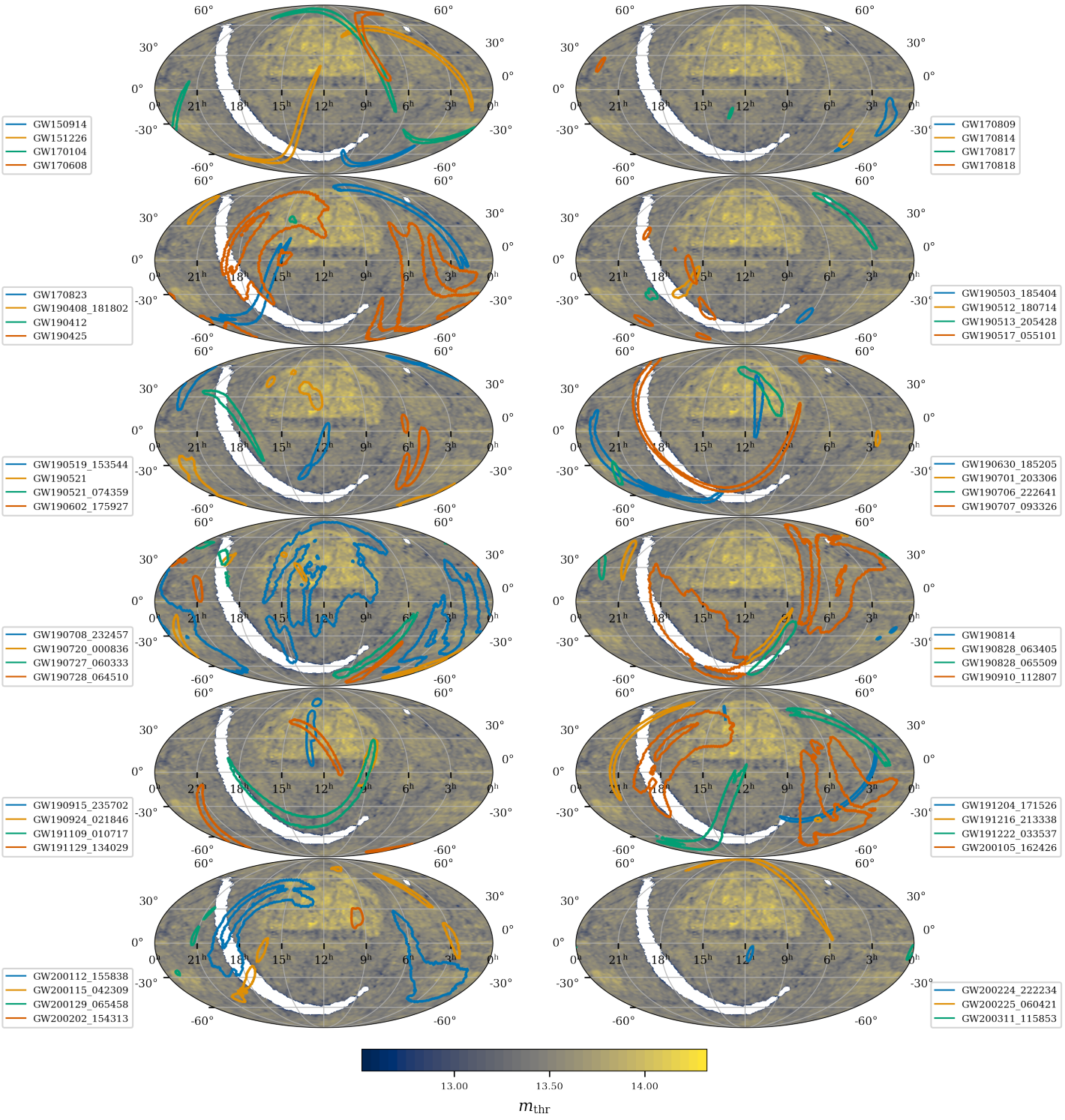

Figure 4.20: Skymaps of the 47 events with $SNR > 11$ from GWTC-3 within the 90% credible level. On the plots we also show the GLADE+ K–band apparent magnitude threshold m_{thr}, generated by dividing the sky into pixels [74]. A mask was applied that removed from the figures all pixels with $m_{thr} < 12.5$ (white pixels).

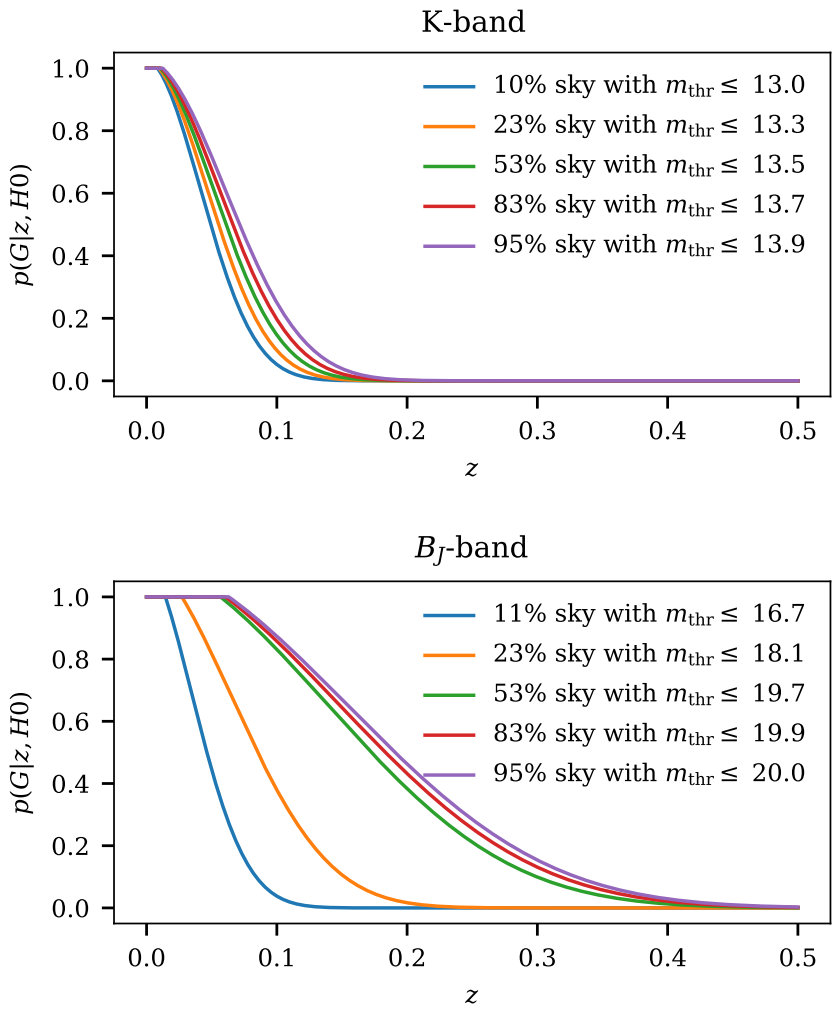

Figure 4.21: Top: Completeness fraction of GLADE+ using the K–band. This gives the probability that the host galaxy of a GW event being inside the galaxy catalog, as a function of redshift. To calculate this we have used a flat ΛCDM cosmology with $H_0 = 67.9$ km/s/Mpc and $\Omega_m = 0.3065$. The various curves indicate how this probability changes for different apparent magnitude thresholds (m_{thr}). The legend reports the fraction of the sky for which the m_{thr} is brighter than the reported one in each curve's legend. Bottom: Same but for B_J-band [74].

for all the events are presented. An interesting trend observed is that, for low values of H_0, the in-catalog likelihood terms tend to dominate. This happens because for low values of H_0 the estimated redshifts of the GW events are smaller and this means that the galaxy catalog is more complete. One can also see that GW190814 is the most informative GW dark siren event. This is because there is a sufficiently small number of galaxies in its sky localization area, which is about 18 deg^2. Combining

No. of events	Galaxy catalog	BBH mass model	H_0 [km s^{-1} Mpc^{-1}]
42 events	No galaxy catalog	Truncated power law	109^{+43}_{-54} (69^{+21}_{-8})
	No galaxy catalog	Power law+Gaussian	50^{+37}_{-30} (68^{+12}_{-8})
	No galaxy catalog	Broken power law	44^{+52}_{-24} (68^{+13}_{-8})
47 events	GLADE+ K–band	Power law+Gaussian	67^{+13}_{-12} (68^{+8}_{-6})
	GLADE+ B_J–band	Power law+Gaussian	67^{+14}_{-12} (68^{+9}_{-6})

Table 4.7: Values of the Hubble constant obtained in this study using different data sets and analysis methods. The columns present from left to right: short description of the sources used in the study with SNR>11; galaxy catalog used (where appropriate); BBH mass model used and the 68.3% credible level H_0 value. The values in the parenthesis are obtained after combining with the GW170817 EM counterpart posterior.

all the dark siren posteriors together with K-band information from GLADE+ we got $H_0 = 67^{+13}_{-12}$ km/s/Mpc. The H_0 value obtained from population assumptions alone (empty catalog case) is $H_0 = 67^{+14}_{-13}$ km/s/Mpc. Finally, combining the posteriors with the K-band information with GW170817 we got $H_0 = 68^{+8}_{-6}$ km/s/Mpc. All of those posteriors can be seen in Fig. 4.23.

Similar to before, we also explored systematic uncertainties that come from the population and the galaxy catalogue assumptions. For the population systematic uncertainties we varied the parameters that we found correlate the most with H_0, namely $\mu_g,\ \gamma,\ M_{max}$. The results can be seen in Fig. 4.24. As expected, populations assumptions affect the H_0 estimation significantly. The most striking variation comes from varying the μ_g value, which is expected since μ_g sets a redshift scale in the mass distribution. For the systematic uncertainties coming from the galaxy catalogue we used the B$_J$-band instead of the K-band for the luminosity weighting and repeated the analysis to see how the results change. We also used the galaxies with K-band but did not weight them by their luminosities (unweighted curve). The results can be seen in Fig. 4.24. In both cases, the H_0 posterior is not significantly affected by this choice and it is, again, dominated by the population assumptions. The H_0 measurements without any galaxy catalogue information for the three mass models considered can be seen in Tab. 4.7 together with results obtained using galaxy catalogues with K-band and B$_J$-band are also presented.

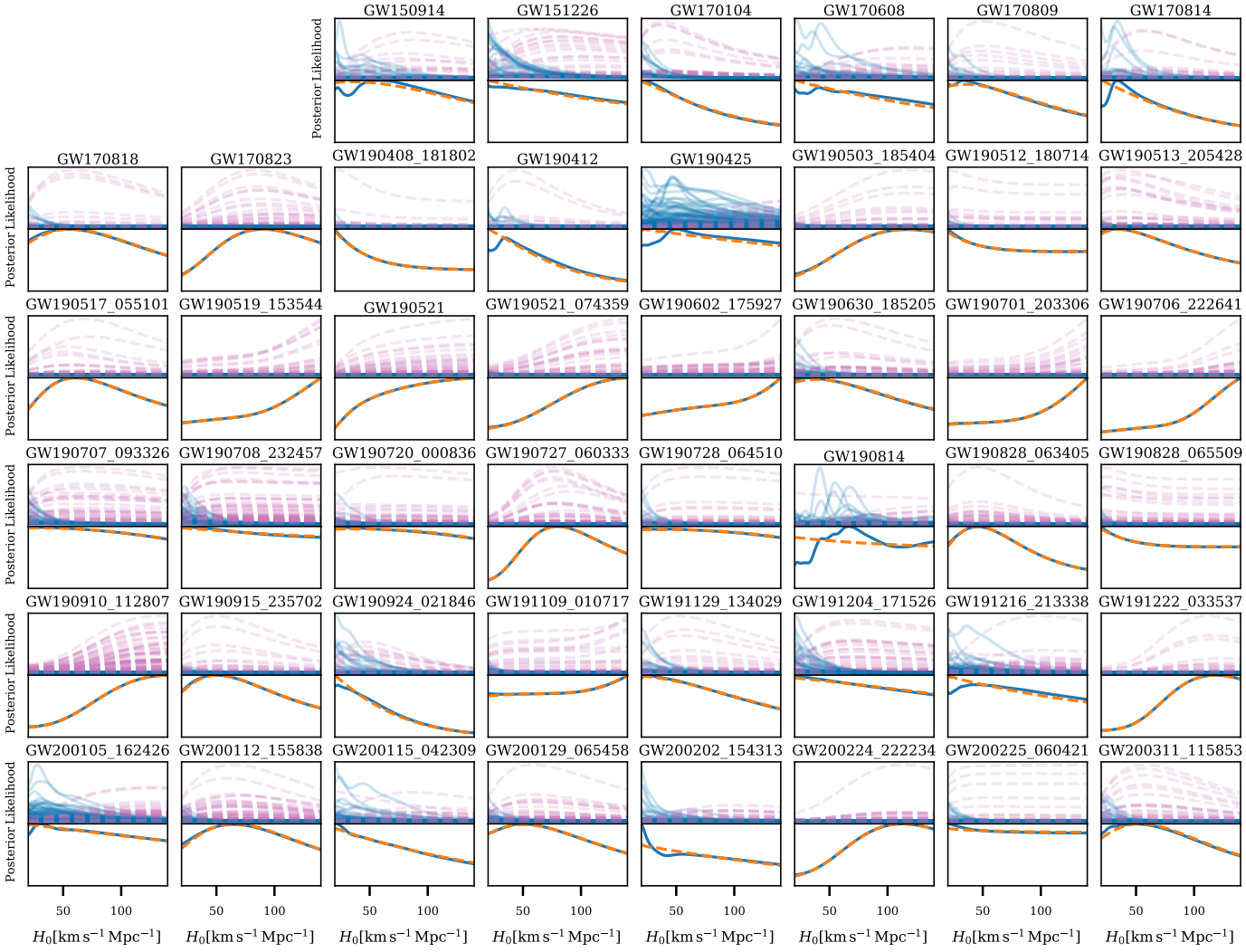

Figure 4.22: Plots of the H_0 posteriors for each event using the GLADE+ K-band and applying luminosity weighting [74]. For each plot: Top panels: The likelihoods obtained assuming that the host galaxy is in the catalog (blue solid curves), which is represented by the hypothesis G, and assuming that the host galaxy is not in the catalog (pink dashed curves), which is represented by the hypothesis $\tilde{G}$. The various curves shown in each panel correspond to different pixels within the sky localization area of each event. Bottom panels: The posteriors obtained by combining the in-catalog and out-of-catalog terms (blue solid curves). The orange dashed curves show the posterior obtained by assuming an empty galaxy catalog. In this case the information on H_0 comes entirely from the population assumptions.

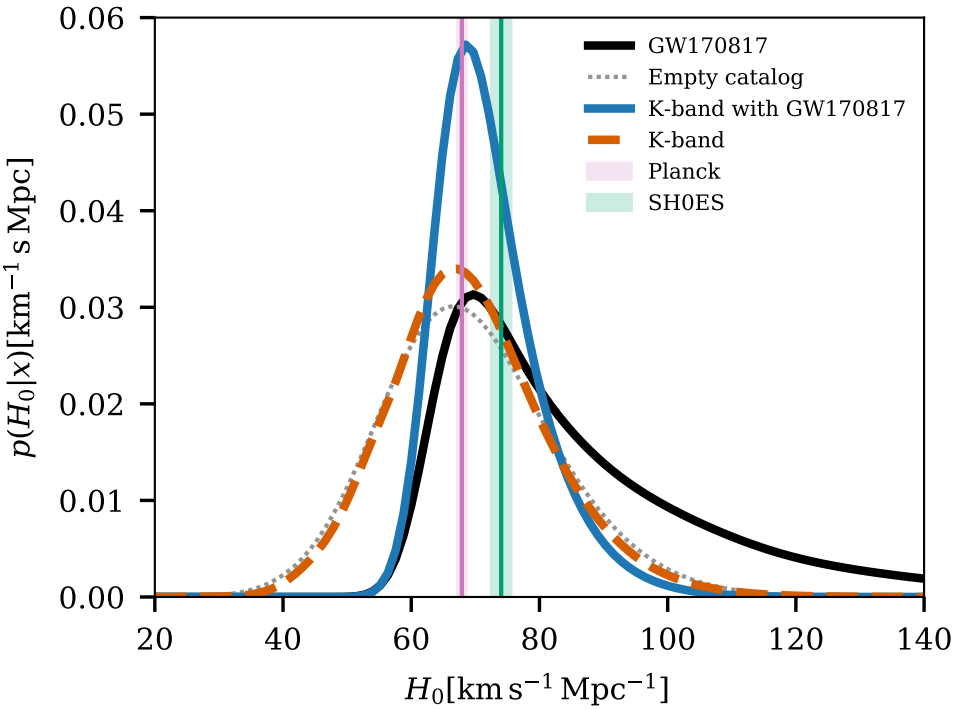

Figure 4.23: Hubble constant posterior for different cases using GWTC-3 [74]. Gray dotted curve: posterior obtained fixing the BBH population model to most preferred one and without using any galaxy catalog information. The posterior becomes informative on H_0 due to our population assumptions. Orange dashed curve: posterior obtained using GLADE+ K–band galaxy catalog information and the same fixed population assumptions as the gray curve. Black solid curve: posterior from GW170817 and its EM counterpart. Blue solid curve: posterior obtained combining dark standard sirens and GLADE+ K–band catalog information (orange dashed curve) with GW170817 and its EM counterpart (black solid curve).

4.3 Constraints on Modified Theories of Gravity

As we have seen, assuming a mass distribution for the BHs gives information about the redshift of the events. Since GW directly provide the luminosity distance, we can combine the two and estimate cosmological parameters. However, as described in Sec. 1.5, we can consider beyond GR models that modify the luminosity distance travelled by GW and put constraints on the parameters of those models. We performed this analysis in Ref. [8].

The methodology to construct the likelihood will be the same as in Sec. 3.2. However, taking into consideration beyond GR models means that in addition to the population

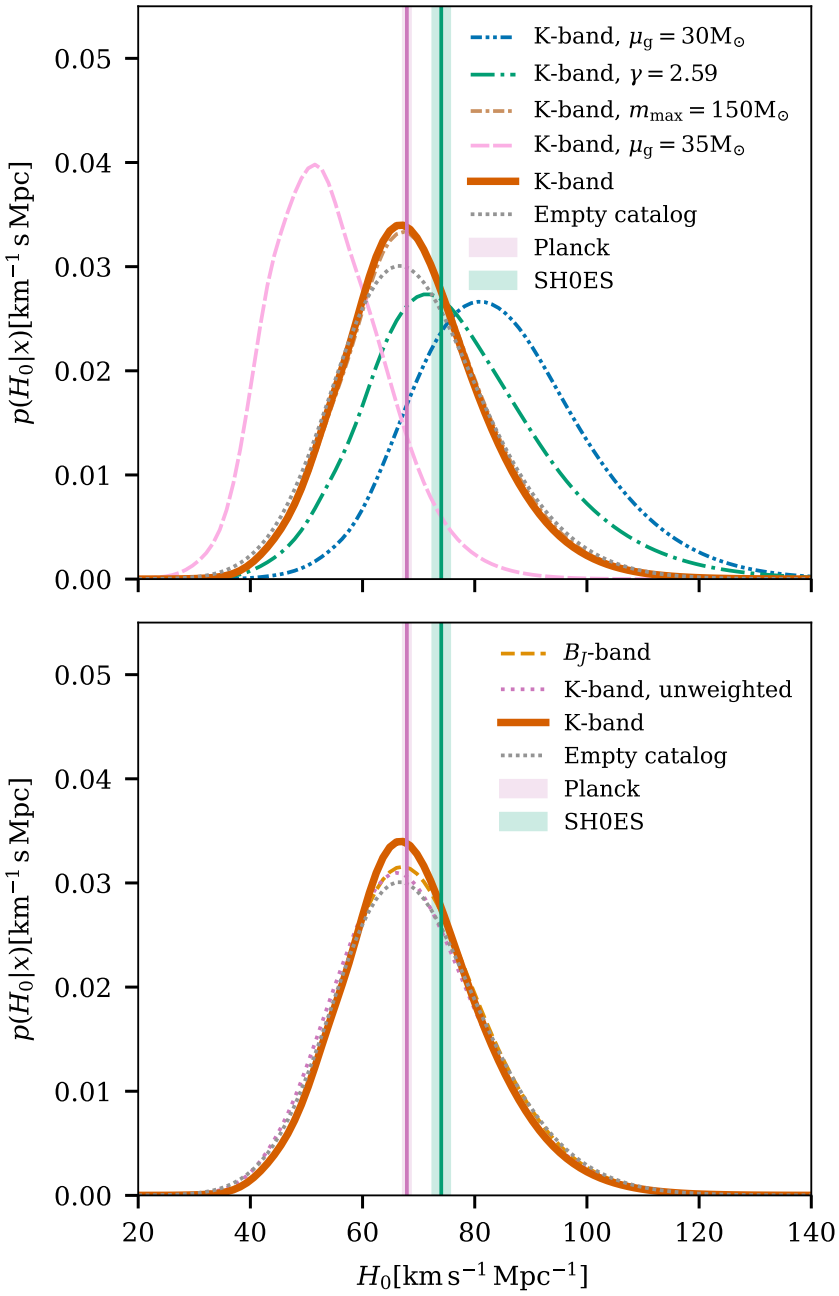

Figure 4.24: Exploring the systematic effects on the Hubble constant posterior that come from (top plot) varying the values of the population model parameters and (bottom plot) changing the choices for the luminosity band and luminosity weighting scheme adopted for the GLADE+ galaxy catalog [74].

parameters that were described before, we now also need to estimate the parameters that govern each beyond GR model. Thus, the set of parameters that we need to estimate now is $\Lambda = \{\Lambda_c, \Lambda_m, \Lambda_R, \Lambda_{BGR}\}$, where Λ_{BGR} is the set of the beyond GR parameters

of each model.

We considered the three beyond GR models described in Sec. 1.5. The parameters for each of those are: for the Ξ_0 parametrization we have $\Lambda_{BGR} = \{\Xi_0, n\}$, for the running Planck mass we have $\Lambda_{BGR} = \{c_M\}$, and for the extra dimensions we have $\Lambda_{BGR} = \{D, R_c, n\}$ (see Tab. 4.8). The merger rate model was again assumed to have the form of Eq. 3.11 with $\Lambda_R = \{z_p, \kappa, \gamma, R_0\}$. For the cosmology we considered a flat ΛCDM model with $\Lambda_c = \{H_0, \Omega_m, \omega_0\}$. Finally, to model m_1 we considered the three models (truncated power law, broken power law, power law+Gaussian) described in the previous section and in addition a fourth model called multi peak model. The multi peak model describes a power law distribution superimposed with two Gaussian peaks. The distribution is given by:

$$p_{MP}(m_1|M_{min}, M_{max}, \alpha, \mu_{g,high}, \sigma_{g,high}, \lambda_g, \delta_m, \mu_{g,low}, \sigma_{g,low}, \lambda_{g,low}) \propto$$
$$S(m_1|M_{min}, \delta_m) \times \begin{cases} (1-\lambda_g)p_{PL}(m_1|M_{max}, M_{min}, \alpha) + \\ \lambda_g(1-\lambda_{g,low})G(m_1|\mu_g, \sigma_g) + \\ \lambda_g\lambda_{g,low}G(m_1|\mu_{g,low}, \sigma_{g,low}) & M_{min} < m_1 < M_{max} \\ 0 & \text{otherwise} \end{cases}, \tag{4.7}$$

where the parameter λ_g is the fraction of events in the two Gaussian components, while the $\lambda_{g,low}$ is the fraction of events in the lower Gaussian component. The mass distribution for the second component is set to the same power law as in the previous section. The priors that we used for the beyond GR parameters that govern each model can be seen in Tab. 4.8. For the cosmological parameters we selected the restricted priors described in Sec. 4.4. The priors for the rate model parameters are the same as in Tab. 4.3, with the exception of the R_0 prior, where here we used a wider uniform prior $\mathcal{U}(0, 1000)$ Gpc^{-3}yr^{-1}. Finally, for the three mass models that were used also before, the priors were set to the same as in Tab. 4.2. For the extra multi peak model used here, the priors can be seen in Tab. 4.9.

We ran the analysis for various SNR thresholds. The logarithm of Bayes factors

Ξ_0 parametrization

Parameter	Description	Prior
Ξ_0	Ξ_0 parameter, see Eq. 1.85.	$\mathcal{U}(0.3, 20)$
n	The power law parameter, see Eq. 1.85.	$\mathcal{U}(1, 5)$

Running Planck mass

Parameter	Description	Prior
c_M	Friction term parametrization constant, see Eq. 1.84.	$\mathcal{U}$(-10, 50)

Extra dimensions

Parameter	Description	Prior
D	Dimensions of spacetime, see Eq. 1.87.	$\mathcal{U}$(3.8,8)
R_c	Screening scale of the model in Mpc, see Eq. 1.87.	Log$\mathcal{U}$(10,10^5)
n	Stiffness parameter, see Eq. 1.87.	Log$\mathcal{U}$(0.1,100)

Table 4.8: The beyond GR parameters considered and the priors used for them. The symbol $\mathcal{U}$ indicates a uniform prior between the specified range and the Log$\mathcal{U}$ indicates a logarithmic uniform prior between the specified range.

Multi peak

Parameter	Description	Prior
α	Spectral index for the power law of the primary mass distribution.	$\mathcal{U}(1.5, 12)$
β	Spectral index for the power law of the mass ratio distribution.	$\mathcal{U}(-4, 12)$
M_{min}	Minimum mass of the power law component of the primary mass distribution.	$\mathcal{U}(2\,M_\odot, 10\,M_\odot)$
M_{max}	Maximum mass of the power law component of the primary mass distribution.	$\mathcal{U}(50\,M_\odot, 200\,M_\odot)$
$\lambda_{\rm g}$	Fraction of the two Gaussian components in the model.	$\mathcal{U}(0, 1)$
$\mu_{\rm g}$	Mean of the high Gaussian component in the primary mass distribution.	$\mathcal{U}(20\,M_\odot, 50\,M_\odot)$
$\sigma_{\rm g}$	Width of the high Gaussian component in the primary mass distribution.	$\mathcal{U}(0.4\,M_\odot, 10\,M_\odot)$
$\lambda_{\rm g,low}$	Fraction of the low Gaussian component in the model.	$\mathcal{U}(0, 1)$
$\mu_{\rm g,low}$	Mean of the low Gaussian component in the primary mass distribution.	$\mathcal{U}(7\,M_\odot, 15\,M_\odot)$
$\sigma_{\rm g,low}$	Width of the low Gaussian component in the primary mass distribution.	$\mathcal{U}(0.4\,M_\odot, 5\,M_\odot)$
δ_m	Range of mass tapering at the lower end of the mass distribution.	$\mathcal{U}(0\,M_\odot, 10\,M_\odot)$

Table 4.9: The mass parameters considered and the priors used for each of them. The symbol $\mathcal{U}$ indicates a uniform prior between the specified range.

of the different models with respect to the Bayes factor of the most preferred model for different SNR thresholds can be seen in Tab. 4.10. Once again, the truncated power law model is highly disfavoured, where in all of the cases the model that best fit

60 BBH events, SNR > 10				
	Broken power law	**Multi peak**	Power law + Gaussian	Truncated power law
GR	−2.4	0.0	−1.2	−6.3
D	−2.0	−0.2	−1.7	−6.4
Ξ_0	−3.2	−0.9	−2.1	−6.8
c_M	−3.0	−1.0	−2.1	−6.5
42 BBH events, SNR > 11				
	Broken power law	**Multi peak**	Power law + Gaussian	Truncated power law
GR	−1.5	0.0	−0.8	−3.2
D	−1.5	−0.0	−0.9	−3.4
Ξ_0	−1.9	−0.6	−1.4	−3.9
c_M	−1.9	−0.9	−1.7	−3.4
35 BBH events, SNR > 12				
	Broken power law	**Multi peak**	Power law + Gaussian	Truncated power law
GR	−1.2	0.0	−1.1	−2.6
D	−1.1	−0.4	−1.2	−2.8
Ξ_0	−2.1	−1.0	−1.9	−3.3
c_M	−1.9	−1.2	−1.9	−3.1

Table 4.10: The logarithm of the Bayes factors for all models and SNR_{thr} considered normalized to the Bayes factor of the most preferred model. The most preferred model combination, depicted in bold, is GR and multi peak mass distribution.

60 BBH events, SNR > 10				
	Broken power law	**Multi peak**	Power law + Gaussian	Truncated power law
D	6^{+2}_{-2}	5^{+3}_{-1}	5^{+3}_{-1}	$4.5^{+3.1}_{-0.8}$
Ξ_0	$1.6^{+1.3}_{-0.8}$	$1.4^{+1.1}_{-0.7}$	$1.3^{+1.2}_{-0.7}$	$0.6^{+1.4}_{-0.2}$
c_M	$1.0^{+2.3}_{-2.6}$	$0.5^{+2.5}_{-2.4}$	$0.1^{+2.7}_{-2.1}$	-2^{+3}_{-1}
42 BBH events, SNR > 11				
	Broken power law	**Multi peak**	Power law + Gaussian	Truncated power law
D	$4.7^{+2.9}_{-0.9}$	$4.6^{+2.6}_{-0.8}$	$4.7^{+2.7}_{-0.9}$	5^{+3}_{-1}
Ξ_0	2^{+3}_{-1}	2^{+4}_{-1}	2^{+3}_{-1}	$0.7^{+3.0}_{-0.4}$
c_M	$0.5^{+4.1}_{-4.2}$	1^{+4}_{-5}	1^{+4}_{-4}	-3^{+5}_{-2}
35 BBH events, SNR > 12				
	Broken power law	**Multi peak**	Power law + Gaussian	Truncated power law
D	5^{+3}_{-1}	$4.6^{+2.9}_{-0.9}$	$4.8^{+2.9}_{-1.0}$	5^{+3}_{-1}
Ξ_0	$1.2^{+1.4}_{-0.7}$	$1.4^{+1.8}_{-0.8}$	$1.4^{+1.8}_{-0.8}$	$0.8^{+2.0}_{-0.5}$
c_M	$-0.1^{+2.8}_{-3.0}$	$0.3^{+3.2}_{-3.3}$	$0.4^{+3.2}_{-3.0}$	-2^{+5}_{-3}

Table 4.11: The median and 90% confidence level estimations for different beyond GR parameters for various SNR thresholds and mass models.

the data is the combination of GR only with the assumption of the multi peak mass model. This is indicative of the two accumulation points around 10 $M_\odot$ and 35 $M_\odot$ in the BBH mass spectrum. It is also apparent the fact that there is no need for additional modified GR parameters in order to fit the observed BBH distribution. In Tab. 4.11 the medians along with the 90% confidence level estimations of beyond GR parameters for various combinations of models and SNR thresholds are presented. For the case of $\mathrm{SNR}_{thr} = 11$, which was considered as the main result of the previous section, and a source frame multi peak mass model, we found that the number of spacetime dimensions is constrained to $D = 4.6^{+2.6}_{-0.8}$, the phenomenological to $\Xi_0 = 2^{+4}_{-1}$ and the running Planck mass to $c_M = 1^{+4}_{-5}$. The posteriors of the beyond GR parameters for all the cases and mass models can be seen in Fig. 4.25. The GR values for each parameter are presented with bold dashed lines. The different SNR_{thr} posteriors are depicted as green dotted (SNR>10), blue solid (SNR>11) and orange dashed (SNR>12) curves. As it can be seen from the plots we find no deviation from GR with the current sensitivity of LIGO-Virgo. The GR predicted values of the beyond GR parameters are all within the 90% confidence levels of our posteriors.

4.4 Redshift Depended Mass Distributions

One of the assumptions that we made in the previous analyses was that the mass distribution of BHs is not redshift dependent. However, since the masses of the formed BHs in each epoch depend on the metallicity of the stars [83, 84, 85, 86, 87], BHs originating from stars of different epochs will have different mass distributions, leading to a redshift dependence BBH mass distribution observed by GW detectors.

By modelling the metallicity of stars as a function of redshift and taking into account the time delay between the forming of the stars and the merger of the BHs we can model the redshift dependence of BHs mass distribution [88, 89]. This methodology leads to a redshift dependence of the mass distribution that is due to i) the pair instability supernovae (PISN) mass scale dependence from the metallicity, (ii) the dependence of the stellar metallicity from the redshift, (iii) a different than zero value of the delay time

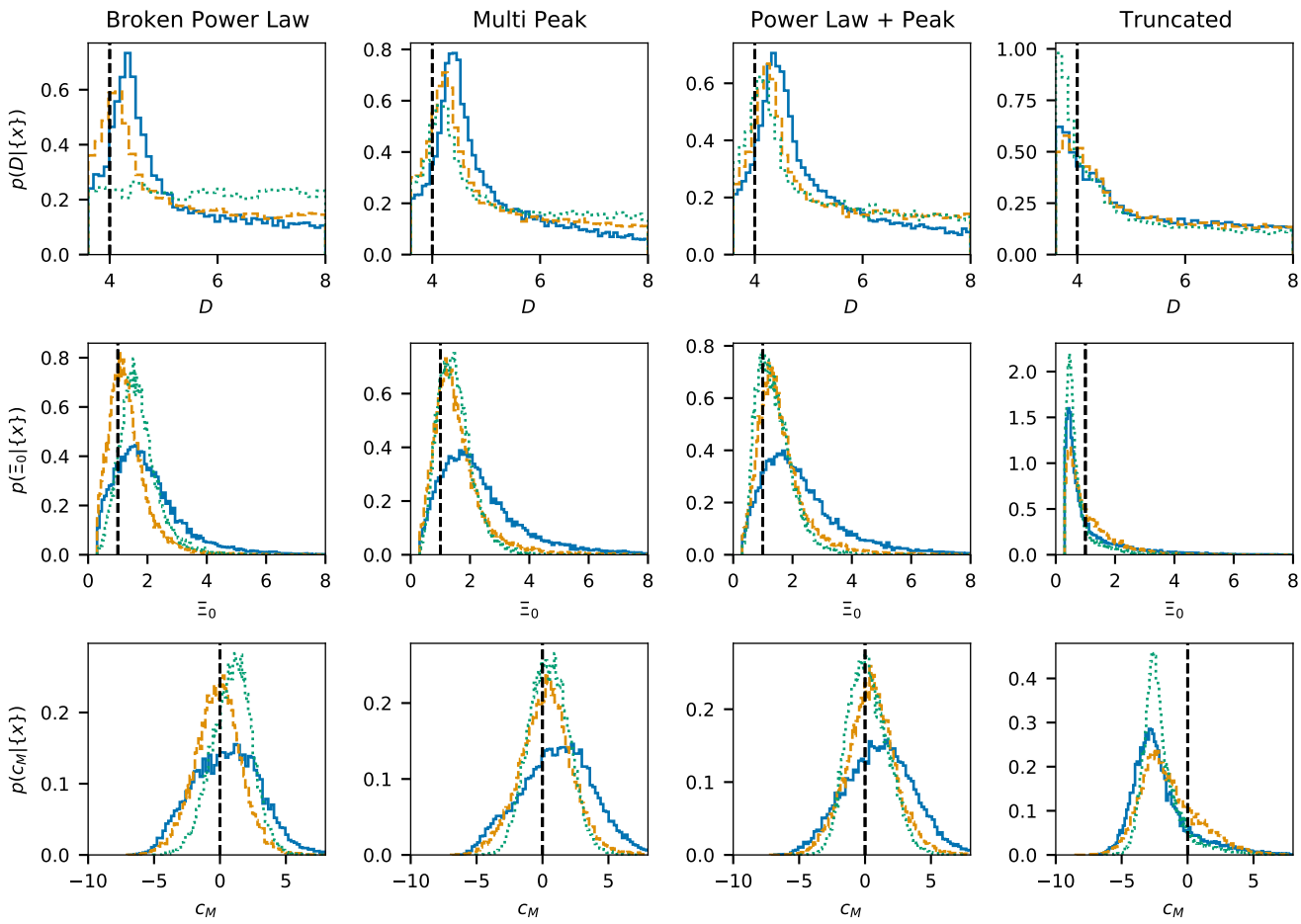

Figure 4.25: Posteriors of beyond GR parameters for various mass models and SNR thresholds [74]. Blue solid curve: posterior with all BBH events with SNR > 11. Orange dashed curve: posterior with all BBH events with SNR > 12. Green dotted curve: posterior with all BBH events with SNR > 10. The GR values of the parameters are plotted in dashed black vertical lines. The posteriors obtained are in accordance with the GR values of the parameters.

between the formation of the stars that will later become BHs, and the merging of the BHs originating from those stars.

We analyze the three effects mentioned above in more detail here: i) The PISN is a type of supernova predicted to happen in stars with high masses (more than 130 $M_\odot$) [90, 91]. During the PISN the internal radiation of a star, that supports the stars core from collapsing due to its own gravitational pull, gets reduced due to pair production (the production of free electrons and positrons in the collision between atomic nuclei and energetic gamma rays). This leads to the star exploding leaving no remnant behind. Due

to this effect, a mass gap in the mass distribution of stellar BHs is expected to exist [92, 87, 93]. The lower limit of the mass gap is predicted to be at around $M_{\rm PISN} = 45M_{\odot}$. However, $M_{\rm PISN}$ is also closely related to the stellar metallicity. The stars with higher metallicity feature a more significant mass loss due to stellar winds, which leads to a lower value of the PISN mass scale with respect to stars formed with a lower metallicity. ii) Metallicity varies with redshift. The evolution of the stellar metallicity indicates that stars at high redshift have poorer metallicity than those at low redshifts [94, 95, 96, 97, 98, 99, 100]. iii) For a star to reach the end of its life and form a BH only a few Myrs are required. However much more time is needed for the BH to form a binary with another BH and merge. The merging BHs that we observe with GW detectors are formed from stars at different redshifts. We take this into account with a time delay distribution that allows the mixing of BHs originating from stars formed at different epochs. We only consider first generation BH, meaning BH that originate directly from stars. Higher generation BHs that originate from the merging of first generation BHs require additional modifications and are out of the scope of this analysis. As a result of the above discussion, the value of the $M_{\rm PISN}$ will vary with redshift.

Following the analysis that was presented in Refs. [88, 89] the mass distribution of first generation BHs at a merging redshift z_m is given by:

$$P(m; z_m) = P_s(m) W_{t_d}(m; z_m), \tag{4.8}$$

where m are the masses in the source frame, $P_s(m)$ is the probability distribution of the stellar objects, which sources the formation of BHs and is related to the initial mass function, and $W_{t_d}(m; z_m)$ is the window function that takes into account the delay time of the mergers. The window function is calculated using:

$$W_{t_d}(m; z_m) = N \int_{z_m}^{\infty} P_t(t_d | t_d^{min}, t_d^{\rm max}, d) \frac{dt}{dz_f} W(m; z_f) dz_f, \tag{4.9}$$

where N is a normalization factor, P_t is the delay time distribution, $W[m(z)]$ is a Heaviside step function $W(m; z_f) = \Theta(M_{\rm PISN}(z_f) - m)$ and z_f is the redshift of the formation of a BH. The W_{t_d} function brings a breaking point $M_{\rm break}$ at the mass

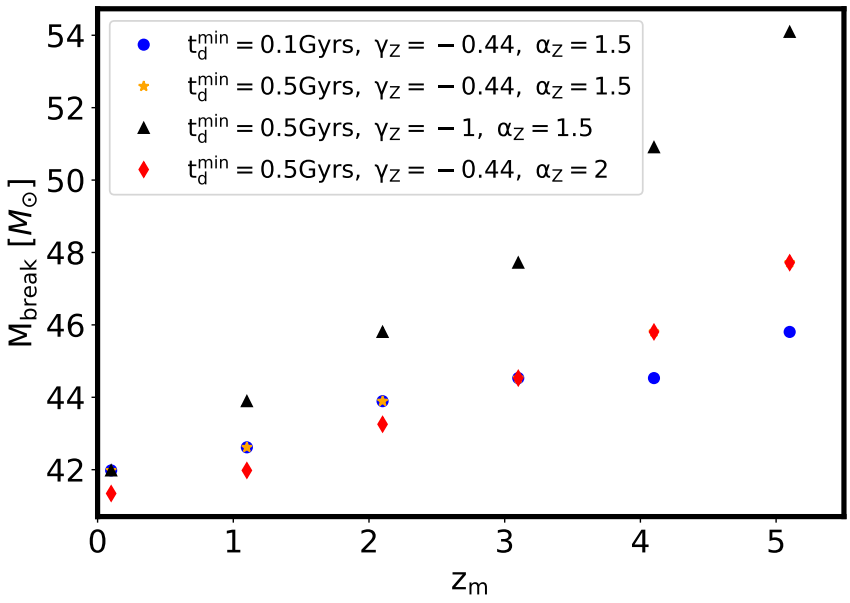

Figure 4.26: The position of $M_{\rm break}$ as a function of redshift varying different parameters. The plot was created with fixed $d = -1$, $H_0 = 70$ km/s/Mpc and $\Omega_m = 0.3$. Varying d does not affect the position of $M_{\rm break}$.

distribution, after which the mass distribution is suppressed depending on the form of the delay time distribution, the dependence of the PISN mass scale on stellar metallicity and the redshift evolution of the stellar metallicity. This break-point depends on the population parameters of the BBHs. It is evaluated from the combination of different $\rm M_{PISN}$ values which are governed by the minimum delay time $t_{\rm d}^{\rm min}$, metallicity evolution $\gamma_{\rm Z}$ and dependence of PISN mass scale on metallicity $\alpha_{\rm Z}$. The evolution of the $M_{\rm break}$ for different choices of these parameters can be seen in Fig. 4.26. The delay time distribution is taken to be a simple power law function of the delay time t_d:

$$P_t(t_d|t_d^{min}, t_d^{\rm max}, d) \propto \begin{cases} (t_d)^d & \text{for } t_d^{min} < t_d < t_d^{\rm max} \\ 0 & \text{otherwise} \end{cases}, \tag{4.10}$$

and the delay time is given by $t_d = t_m - t_f$, with the notation $t_m = t(z_m), t_f = t(z_f)$ to be the time of merger and time of formation, respectively. We model the dependence of the PISN mass scale on metallicity $M_{\rm PISN}(Z)$ using a parameter α_Z as:

$$M_{\rm PISN}(Z) = M_{\rm PISN}(Z_*) - \alpha_Z \log(Z/Z_*), \tag{4.11}$$

and for a power law redshift evolution of the stellar metallicity, we can write the redshift dependence of metallicity as $\log Z(z) = \gamma_Z z + \zeta$. Consequently, the previous equation can be written as:

$$M_{\rm PISN}(z) = M_{\rm PISN}(Z_*) - \alpha_Z[\gamma_Z z + \zeta - \log(Z_*)], \tag{4.12}$$

where ζ is taken to be a constant to match the low redshift measurement of the stellar metallicity $Z(z=0) \approx 10^{-2}$.

We use the same methodology described in Sec. 3.2 and we construct the following model to describe distribution of BBHs in terms of their source frame masses m_1, m_2 and merger redshift z_m:

$$p(m_1, m_2, z_m|\Lambda) = p(m_1, m_2|z_m, \Lambda_m, \Lambda_d, \Lambda_{\rm nuis})p(z_m|\Lambda_d, \Lambda_c, \Lambda_R). \tag{4.13}$$

where $\Lambda = \{\Lambda_{\rm m}, \Lambda_{\rm c}, \Lambda_{\rm d}, \Lambda_{\rm nuis}, \Lambda_R\}$ are a set of population parameters governing the mass model ($\Lambda_{\rm m}$), cosmology ($\Lambda_{\rm c}$), time delay ($\Lambda_{\rm d}$), rate model (Λ_R) and a set of nuisance parameters ($\Lambda_{\rm nuis}$). In order to capture the mass distribution of BBHs that originate from the BHs mass distribution of Eq. 4.8, we consider the following:

$$p(m_1|z_m, \Lambda_{m_1}, \Lambda_d, \Lambda_{nuis}) = p(m_1|z_m, \Lambda_{m_1})W_{t_d}(m_1; z_m). \tag{4.14}$$

We model the distribution of BBHs in terms of their source frame masses m_1, m_2 and merger redshift z_m of the binary as

$$p(m_1, m_2|z_m, \Lambda_m, \Lambda_d, \Lambda_{nuis}) = p(m_1|z_m, \Lambda_{m_1}, \Lambda_d, \Lambda_{nuis})p(m_2|m_1, \Lambda_{m_2})S_1S_2, \tag{4.15}$$

The distribution of m_1 in the source frame $p(m_1|z_m, \Phi_{m_1})$ is considered to be given by a power law distribution superpositioned with the distribution of a Gaussian peak:

$$p(m_1|z_m, \Lambda_{m_1}) = (1-\lambda_g)P(m_1|M_{\rm min}, M_{\rm max}, -\alpha) + \lambda_g G(m_1|M_{break}(z_m), \sigma_g), \tag{4.16}$$

where $\Lambda_{m_1} = \{M_{\rm min}, M_{\rm max}, \alpha, \lambda_g, M_{break}(z_m), \sigma_g\}$, $G(m_1|M_{break}(z_m), \sigma_g)$ is a Gaussian

distribution with $\mu = M_{break}(z_m)$ and $\sigma = \sigma_g$ and $P(m_1|M_{\rm min}, M_{\rm max}, -\alpha)$ is a power law distribution with slope $-\alpha$ between $M_{\rm min}$ and $M_{\rm max}$. In this model the power law part of the mass distribution is motivated by the power law form of the initial mass function [101] and Gaussian part of the mass distribution is motivated from the PISN mass scale. The sources merging at redshift z_m due to the contribution from all the higher redshift will lead to an excess near the value of $\rm M_{break}$ and then a decline in the mass distribution due to the window function. The position of the Gaussian peak μ is considered at the break of the window function at that redshift which depends on the metallicity dependence of the PISN mass scale and delay time distribution. The value of the PISN mass scale is inferred for the metallicity value at $Z_* = 10^{-4}$ (for which the results are obtained by Ref. [102]). The Gaussian peak modelled in this analysis gets a physical motivation expected from PISN mass scale, but is also expected to evolve as a function of the redshift of BBHs mergers.

The distribution of m_2 in the source frame is considered to be given by a power law distribution with maximum value m_1:

$$p(m_2|\Lambda_{m_2}) = P(m_2|M_{\rm min}, m_1, \beta). \tag{4.17}$$

Since m_2 is conditional to m_1, the window function W_{t_d} is being applied also to m_2 indirectly. Finally, the functions $S_{(1,2)} = S(m_{(1,2)}|\delta_m, M_{\rm min})$ are again sigmoid-like window functions to smooth the lower end of the distributions.

The distribution $p(z_m|\Lambda_d, \Lambda_c)$ takes into account the BBH merger rate as a function of redshift and it is built as:

$$p(z_m|\Lambda_d, \Lambda_c) = C\frac{R(z_m)}{1+z}\frac{dV_c}{dz_m}|_{\Lambda_c}, \tag{4.18}$$

where C is a normalization constant, $\frac{dV_c}{dz_m}$ the differential of the comoving volume and $R(z_m)$ the BBH merger rate as function of redshift. The BBH merger rate is given by:

$$R(z_m) = R_0\frac{\int_{z_m}^{\infty} P_t(t_d|t_d^{min}, t_d^{\rm max}, d)R_{SFR}(z_f)\frac{dt}{dz_f}dz_f}{\int_0^{\infty} P_t(t_d|t_d^{min}, t_d^{\rm max}, d)R_{SFR}(z_f)\frac{dt}{dz_f}dz_f}, \tag{4.19}$$

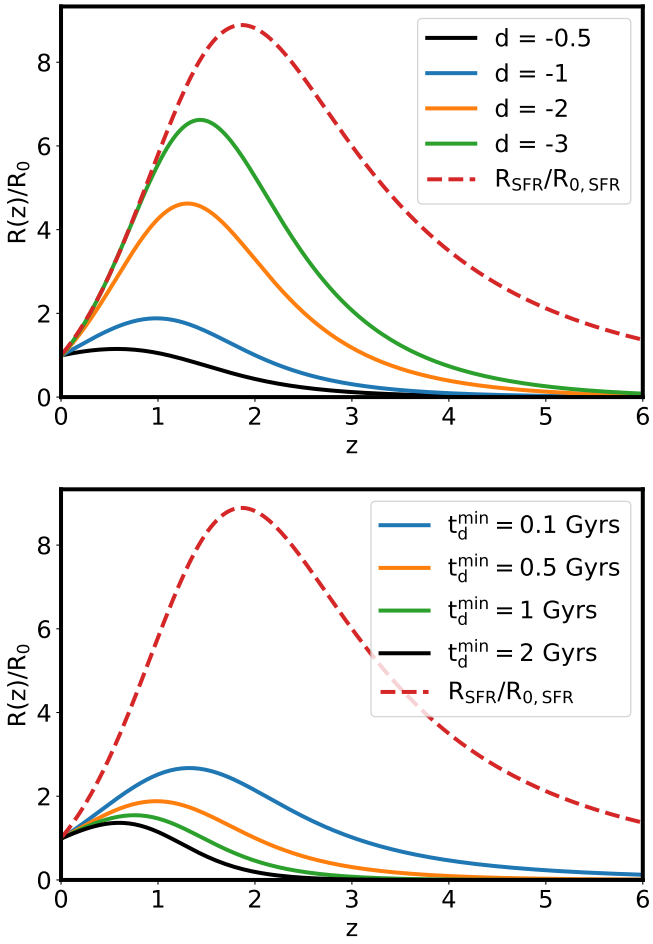

Figure 4.27: The merger rate function $R(z)$ for various values of the parameters d, $t_d^{\min}$ and for a fiducial flat ΛCDM cosmology with a constant energy density for dark energy and $H_0 = 70$ km/s/Mpc and $\Omega_m = 0.3$ [89]. Top: Fixing $t_d^{\min} = 0.5$ Gyrs and varying d. Bottom: Fixing $d = -1$ and varying $t_d^{\min}$. On the same plot we can also see the star formation rate $R_{SFR}/R_{0,SFR}$.

where $R_0 \equiv R(z = 0)$ is defined as the merger rate at $z = 0$. $R_{SFR}(z)$ is given by Eq. 3.11 for $\gamma = 2.7$, $z_p = 1.9$, $\kappa = 2.9$. The merger rate model now depends on the time delay model and its parameters. In Fig. 4.27 we show how varying time delay parameters affect the merger rate model. In this model, the merger rate and the mass distribution are both affected by the time delay distribution. To summarize, the hyper-parameters in this model are $\Lambda = \{\Lambda_m, \Lambda_{delay}, \Lambda_{nuis}, \Lambda_R, \Lambda_c\}$, instead of $\Lambda = \{\Lambda_m, \Lambda_R, \Lambda_c\}$ that were used in the previous section. Λ_m is the set of the mass model parameters $\Lambda_m = \{M_{\min}, M_{\max}, \alpha, \beta, \lambda_g, M_{break}(z_m), \sigma_g, \delta_m\}$, Λ_{delay} is the set of the time delay parameters $\Lambda_{delay} = \{d, t_d^{min}\}$, Λ_R is the set of merger rate parameters

$\Lambda_R = \{R_0\}$, Λ_{nuis} is the set of the nuisance parameters of the model $\Lambda_{nuis} = \{\alpha_Z, \gamma_Z\}$ and Λ_c is the set of cosmological parameters. In this analysis we consider a flat ΛCDM model for which $\Lambda_c = \{H_0, \Omega_m\}$. The priors we used for of all those parameters can be seen in Tab. 4.12.

Delay time + Merger rate parameters

Parameter	Description	Prior
d	Spectral index for the power-law of the delay time distribution.	$\mathcal{U}$(-4,0)
$t_d^{\min}$	Minimum time for the power-law of the delay time distribution in Gyrs.	$\mathcal{U}$(0.01,13)
R_0	Value of the merger rate at $z = 0$ in $\mathrm{Gpc}^{-3}\ \mathrm{yr}^{-1}$.	$\mathcal{U}$(0,1000)

Mass distribution parameters

Parameter	Description	Prior
α	Spectral index for the power-law of the primary mass distribution.	$\mathcal{U}$(-4,12)
β	Spectral index for the power-law of the mass ratio distribution.	$\mathcal{U}$(-4,12)
$M_{\min}$	Minimum mass of the power-law component of the primary mass distribution in $M_\odot$.	$\mathcal{U}$(2,10)
$M_{\max}$	Maximum mass of the power-law component of the primary mass distribution in $M_\odot$.	$\mathcal{U}$(50,200)
λ_{g}	Fraction of the Gaussian component in the model.	$\mathcal{U}$(0,1)
$M_{\mathrm{PISN}}(Z_*)$	The value of M_{PISN} at for the metallicity value Z_* in $M_\odot$.	$\mathcal{U}$(20,60)
σ_{g}	Width of the Gaussian component in the primary mass distribution in $M_\odot$.	$\mathcal{U}$(0.4,10)
δ_m	Range of mass tapering at the lower end of the mass distribution in $M_\odot$.	$\mathcal{U}$(0,10)

Cosmological parameters (Flat ΛCDM model)

Parameter	Description	Prior
H_0	The Hubble constant parameter in km/s/Mpc.	67.4, $\mathcal{U}$(20,150)
Ω_m	Present-day matter density of the Universe.	0.315 (fixed)

Nuisance parameters

Parameter	Description	Prior
α_{Z}	The parameter that captures a weak logarithmic dependence of M_{PISN} on the metallicity.	$\mathcal{U}$(0,15)
γ_{Z}	The parameter that captures the redshift dependence of the metallicity.	$\mathcal{U}$(-5,0)

Table 4.12: Summary of the hyper parameters and the priors used. The distribution $\mathcal{U}(min, max)$ is just a uniform distribution between min and max for each parameter.

We ran using all BBH events from GWTC-3 with SNR> 12, without GW190521 and performed various runs with different configurations. The reason for excluding

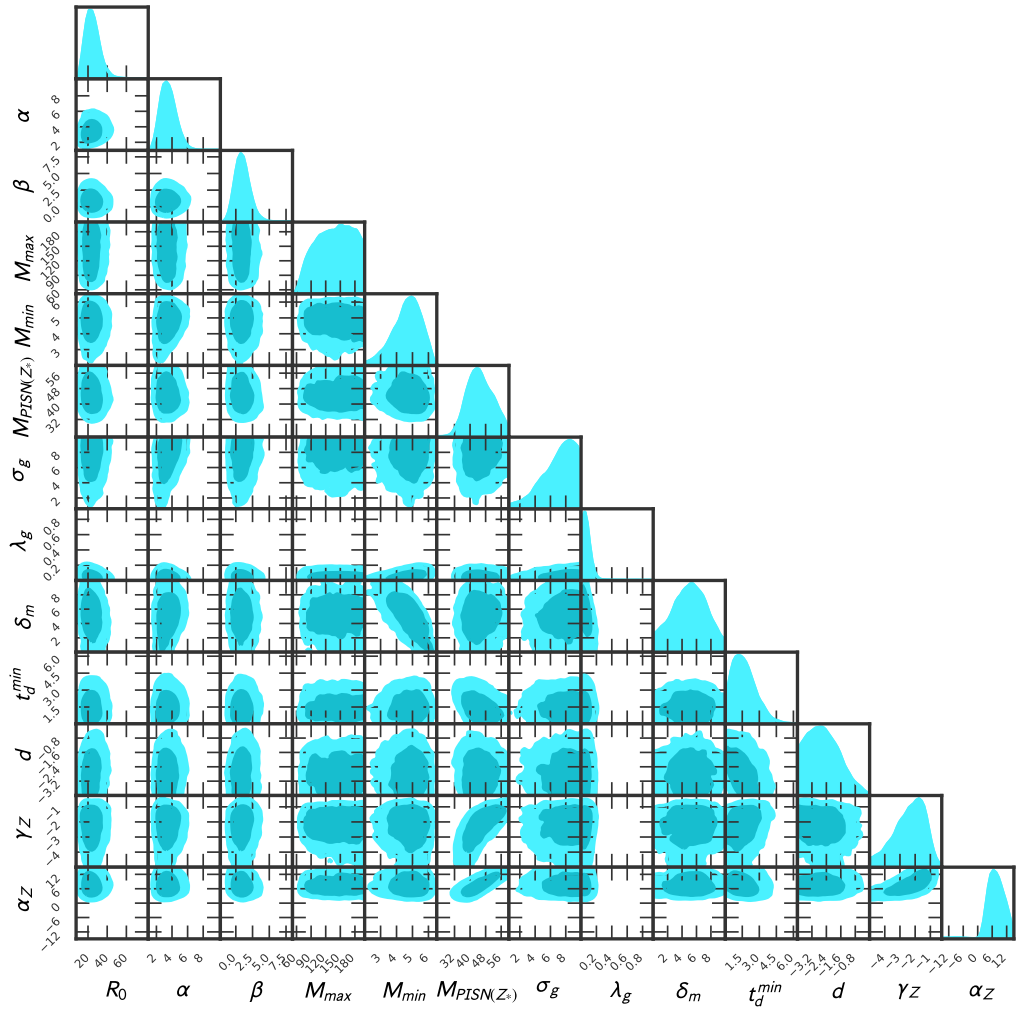

Figure 4.28: Posterior distributions for all the hyper parameters while fixing all cosmological parameters to the Planck-2018 cosmology. We have used all GW events with $SNR \geq 12$ [89].

GW190521 was that the masses of its BHs components are rather heavy. This means that they are likely second generation BHs and not of astrophysical origin. To model secondary generation BHs requires the inclusion of an additional term in the mass distribution. The setup that we found as the most preferred is the one where we fixed cosmology to the values measured from Planck and estimate conjointly the rest of the parameters (referred to as Pop). The posteriors obtained in this case can be seen in Fig. 4.28. The estimation that we obtain for $M_{\rm PISN}(Z_*)$ is $M_{\rm PISN}(Z_*) = 44.79^{+7.39}_{-6.05}$ $\rm M_\odot$ and is in accordance with the theoretically predicted position of the PISN mass scale between 45-60 $\rm M_\odot$. Next we performed a run fixing H_0 and the power law of the time

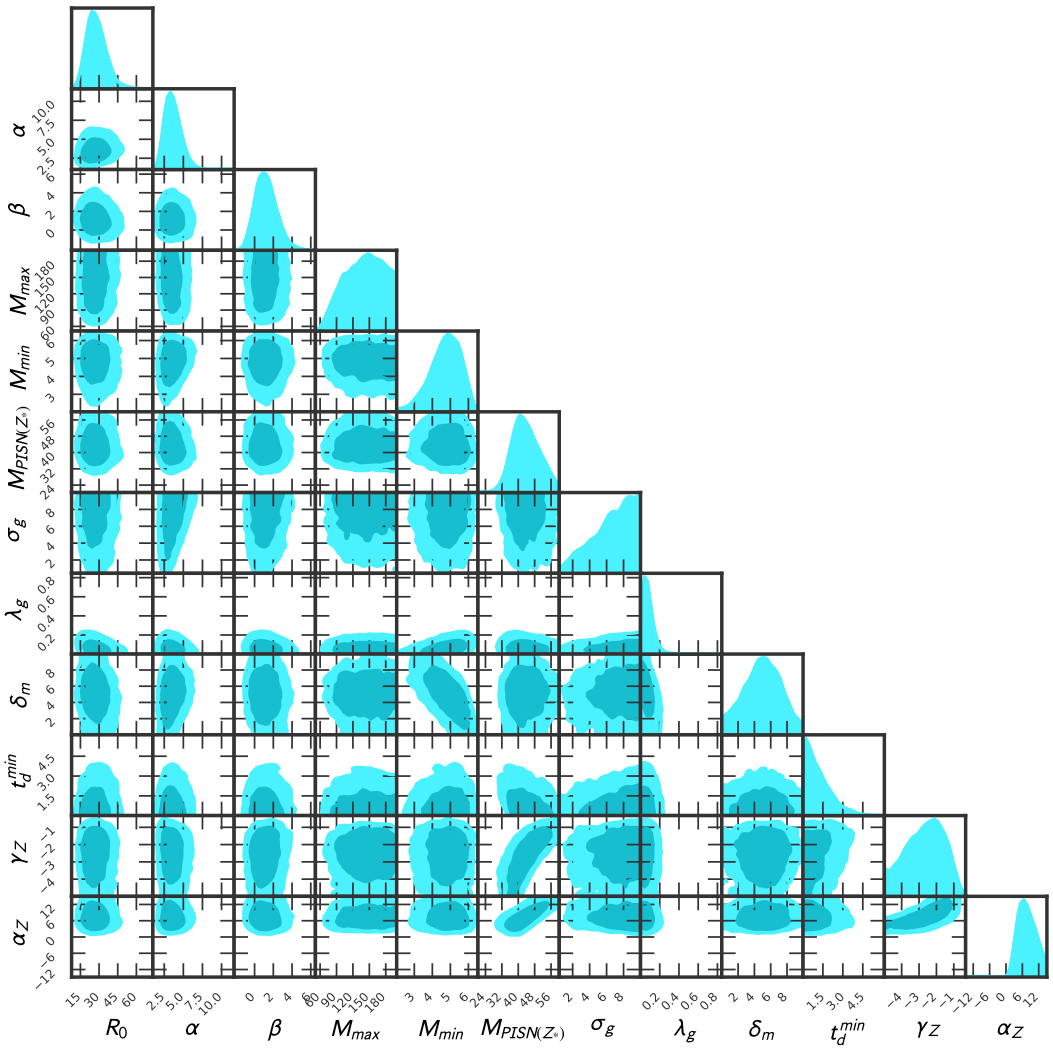

Figure 4.29: Posterior distributions for all the hyper parameters while fixing all cosmological parameters to the Planck-2018 cosmology and fixing $d = -1$. We have used all GW events with $SNR \geq 12$ [89].

delay distribution $d = -1$ (referred to as Pop(d $= -1$)). This value is usually assumed as a fiducial scenario for flat in the log-space distribution of the separation between the binaries. The posteriors for this case can be seen in Fig. 4.29. Finally, we perform a run allowing both H_0 and d to vary (referred to as Pop $+ H_0$). The posteriors can be seen in Fig. 4.30.

For the three different runs that we performed, the posteriors of t_d^{min} and can be found in Fig. 4.31 and the posteriors for $M_{\rm PISN}(Z_*)$ in Fig. 4.32. As it can be seen, the constraints for t_d^{min} are more stringent in the case of $d = -1$. However, when we

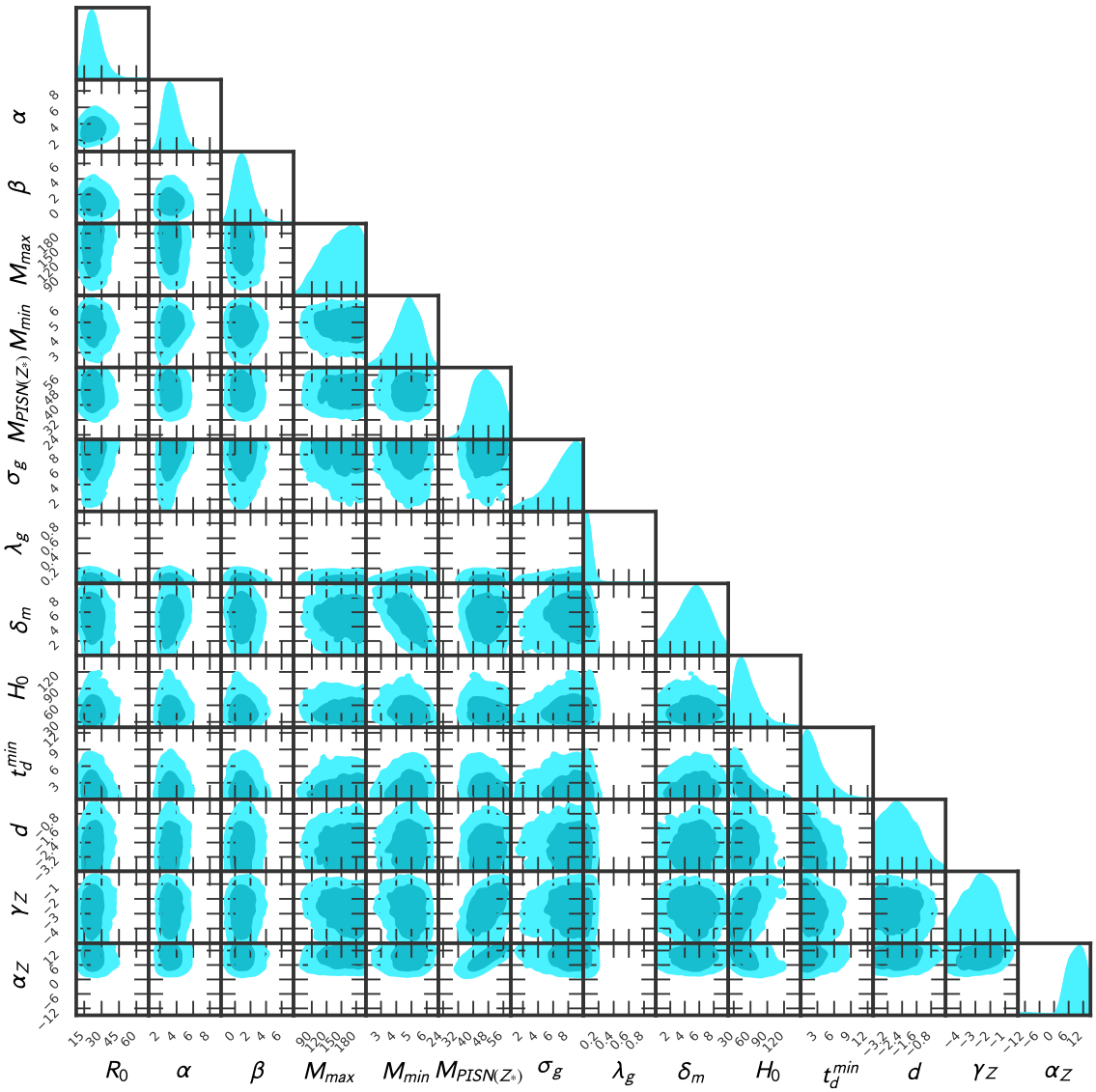

Figure 4.30: Posterior distributions for all the hyper parameters while fixing all cosmological parameters besides H_0 to the Planck-2018 cosmology. We have used all GW events with $SNR \geq 12$ [89].

allow d to vary, we obtain posteriors that do not favor the value $d = -1$. Specifically, we find that $-d = 2.63^{+0.86}_{-0.98}$ for the Pop case and $-d = 2.56^{+0.9}_{-1.01}$ for the Pop+H_0 case. The M_{PISN} redshift evolution obtained from the posterior samples (cyan curves) for the case Pop can be seen in Fig. 4.33. In the same plot the median of the distribution (red curve) along with the 68% credible levels (dashed purple lines) are presented. We retrieve a weak evidence of $\mathrm{M_{PISN}}$ with redshift as it spans from around 30 $\mathrm{M_\odot}$ for $z = 0$ up to around 40 $\mathrm{M_\odot}$ for $z = 1$ which is not very statistically significant yet. Finally, the

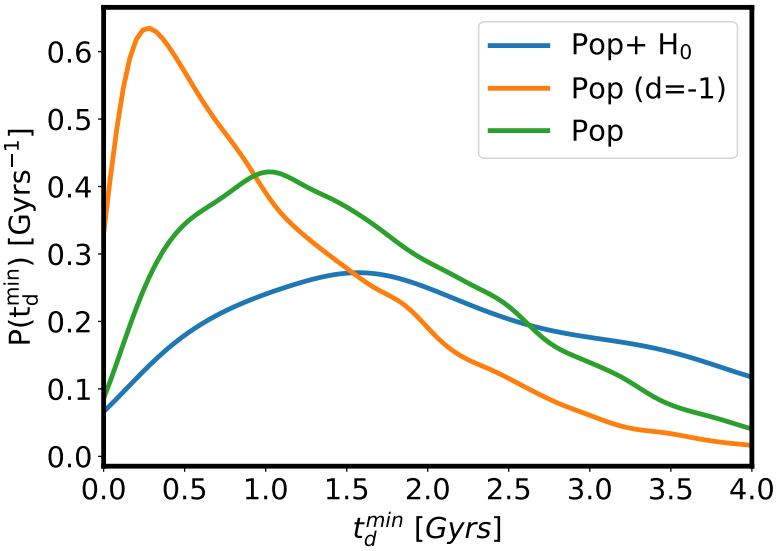

Figure 4.31: Posteriors of t_d^{min} for the three cases considered [89]. The orange curve is the estimation when fixing $d = -1$. The green curve is the one obtained when fixing H_0 to the value measured by the Planck collaboration. Finally, the blue curve is obtained when allowing H_0 and d to vary [89].

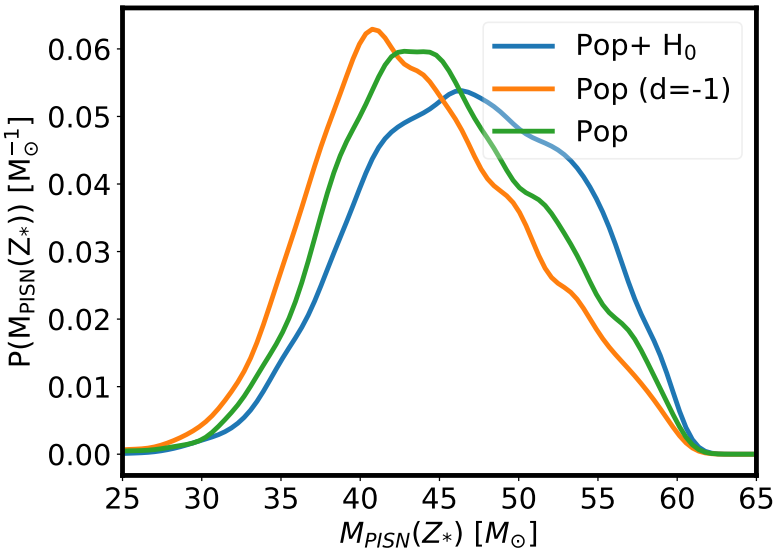

Figure 4.32: Posteriors of μ_g for the three cases considered[89]. The orange curve is the estimation when fixing $d = -1$. The green curve is the one obtained when fixing H_0 to the value measured by the Planck collaboration. Finally, the blue curve is obtained when allowing H_0 and d to vary [89].

merger rate obtained for different posterior samples (cyan curves) for the case Pop can be seen in Fig. 4.34 along with the median of the distribution (red curve) and the 68% credible levels (dashed purple lines).

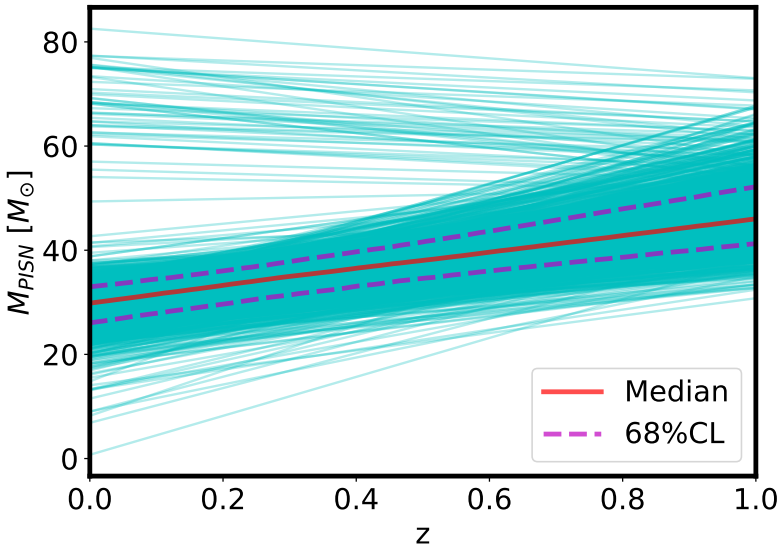

Figure 4.33: The M_{PISN} position as a function of redshift for different posterior samples (cyan curves). In the same plot the median (red solid curve) and the 68% credible levels (purple dashed curves) can also be seen [89].

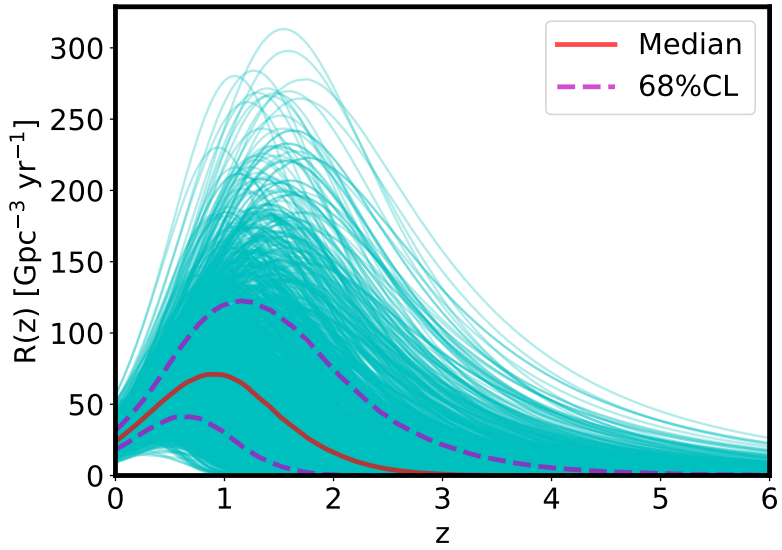

Figure 4.34: The merger rate evolution as a function of redshift for different posterior samples (cyan curves). In the same plot the median (red solid curve) and the 68% credible levels (purple dashed curves) can also be seen. The cases with a fixed value are shown with the fixed mean value and zero uncertainty [89].

The BBHs merger rate as a function of m_1 for different redshifts drawn from the posterior samples distributions can be seen in Fig. 4.35. The solid curves are the medians for each redshift value, whereas the shaded regions are the 68% credible intervals for

each curve. As it can be seen, there is a clear redshift dependence of the Gaussian peak of the distribution. As redshift increases, the Gaussian peak moves to higher values.

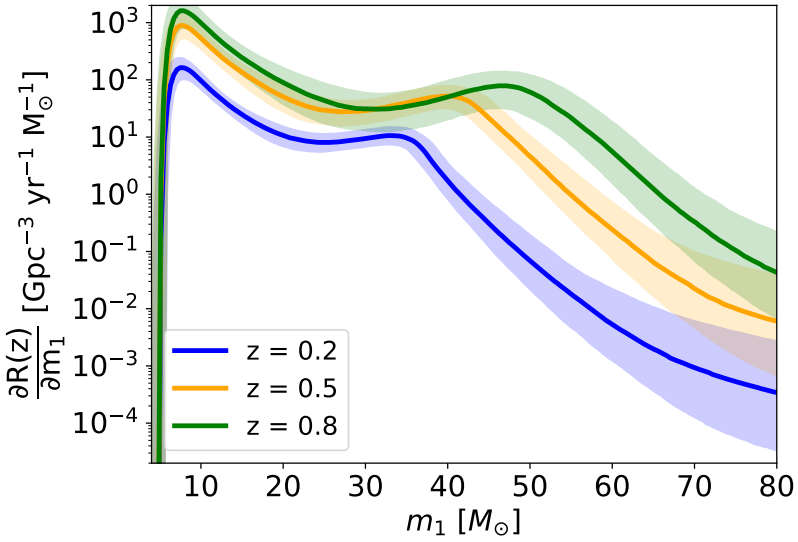

Figure 4.35: BBHs merger rate as a function of redshift for the primary BBHs mass [89]. The different colors indicate the merger rates at different redshifts. Solid lines show the median of the distribution, whereas the shades indicate the 68% credible levels.

Chapter 5

GWSim: A Python Package for Simulated Gravitational Waves Catalogues

GW events offer a unique opportunity to perform cosmological analyses. In previous chapters we have seen the methods and codes that we have developed in order to obtain cosmological estimations using GW data. However, estimations of parameters often suffer from known or unknown systematic uncertainties that can lead to biased results. To tackle this problem, it is required to run our codes on known data sets that were created with certain known values of the parameters of interest, and try to estimate back the input values. In this chapter we present a code that we developed and can produce simulated GW data sets meant for validating estimation codes.

5.1 Description of GWSim Code

In order to understand if our analyses are biased towards any of the estimated parameters, we developed a code, called GWSim [103], able to create GWTC simulated data, while using different rate, mass and cosmological models.

The logical steps behind GWSim are the following:

- Select galaxies to host GW events based on the selected merger rate model.

- Select the GW events source frame parameters based on the chosen mass and spin distributions.
- Use the selected cosmological model and the redshift of the host galaxies to calculate the luminosity distances of the events.
- Infer the detected events by calculating the SNR of the events taking into account detector noise and duty cycles.

Following those logical steps, GWSim is able to simulate GW transient catalogues (GWTCs) with various mass, spin, and cosmological models (see next section). The galaxies can either be selected from a real galaxy catalogue, like GLADE, or a simulated one, like MISECAT [104, 105, 106]. The code in this case loads all galaxies present in the catalogue and select some of them to be the hosts of GW events, based on the merger rate model as a function of redshift and the redshift of each galaxy. Furthermore, there is another choice for this step, instead of a real galaxy catalogue the user can produce what we call a universe file, by assuming a given cosmology. In this case, the code creates a file containing galaxies that are distributed in redshift following a uniform in comoving volume distribution and uniformly over the sky, so there is no clustering present. Luminosities of galaxies are being selected from a Schechter function distribution with parameters that are given by the user. This file can be later loaded into the module that selects the host galaxies of events.

GW events are assigned into the chosen galaxies and the events parameters are sampled from distributions selected by the user. The user is also able to select the duty factors of the detectors and the total observation time of the simulated observing run. The code then calculates the SNR of all GW events and deduces the detected ones based on the SNR threshold given by the user. All events with $\mathrm{SNR} > \mathrm{SNR}_{\mathrm{thres}}$ are considered detected and constitute the GWTC. Finally, the events that are considered detected undergo parameter estimation process using the python package BILBY ([107]). The parameters of each GW event are getting estimated during the parameter estimation step and the output is a set of GW posteriors that can be used in every GW code working with GWTCs. A flowchart of the code can be seen in Fig. 5.1.

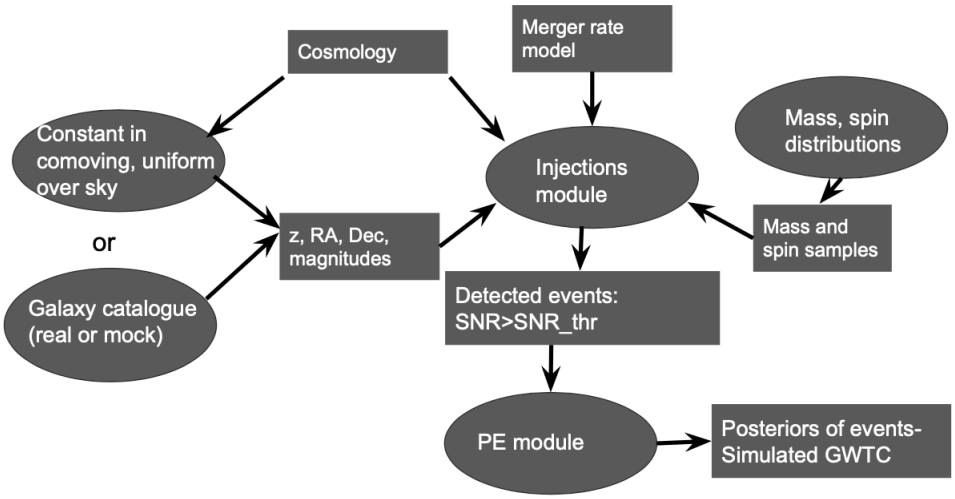

Figure 5.1: Flowchart of the GWSim code [103].

5.2 Models Available

As discussed before, there are various distribution models implemented inside the GWSim code. In this section we describe the available distributions for cosmological, mass, spin and merger rate models.

5.2.1 Cosmological Models

We implemented various cosmological models in GWSim, all assuming zero energy density of curvature, i.e. flat models, non flat models will be implemented in the future. We focused on the most common cosmological models to start with and implemented those. We currently have at our disposal flat ΛCDM, w_0CDM, which includes a dark energy equation of state without redshift dependence, and $w_0 - w_a$CDM, which features a dark energy equation of state that evolves with redshift. The code is able to sample successfully the uniform in comoving volume distribution, as it can be seen in Fig. 5.2.

5.2.2 Mass Models

The mass models that are implemented into GWSim are divided into redshift independent and redshift dependent. The redshift independent mass models are the same as the ones described in Chapter 4, namely truncated power law, broken power law,

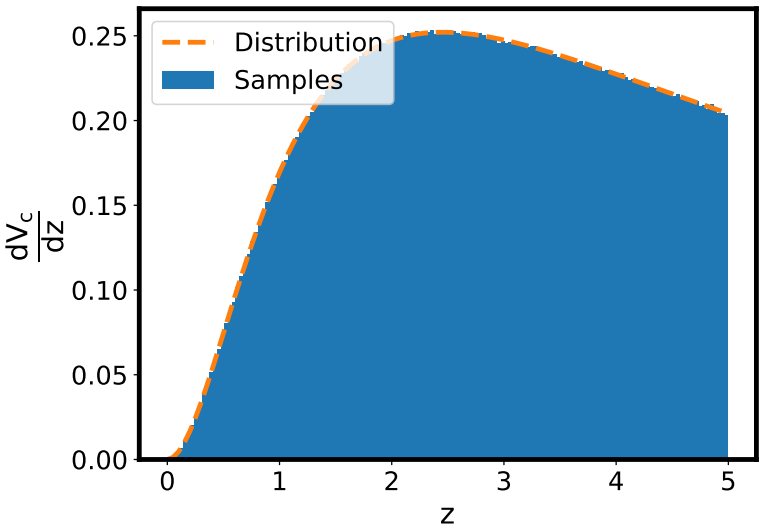

Figure 5.2: The samples drawn from the comoving volume distribution using GWSim for a fiducial flat ΛCDM cosmology with $H_0 = 70$ and $\Omega_m = 0.3$. The analytical form of the distribution is presented as a dashed orange curve and the samples drawn from it are histogrammed in blue [103].

power law+Gaussian peak and multi peak mass model. The analytical forms of those distributions and the samples that the code drew can be seen in Fig. 5.3. The analytical forms of the distributions are depicted as dashed orange curves and the samples the code drew are histogrammed in blue. As it can be seen, the samples follow nicely the analytical forms.

The redshift dependent mass models are following the redshift independent distributions but now every parameter that governs the mass model gets a redshift linear dependence. More specifically, the parameter x is evolving with the redshift following the relation:

$$x = x_0 + \epsilon_x z, \tag{5.1}$$

where x_0 is the value of the parameter at $z = 0$ and ϵ_x is the redshift evolution of the parameter. An example of one redshift dependent mass distribution can be seen in Fig. 5.4. Here we chose the power law+Gaussian peak and allowed only the position of the Gaussian peak to evolve with redshift, while fixing all the rest of the parameters to non evolving values. Besides those purely phenomenological models, the redshift dependent mass distribution that comes from taking into account the time delay between

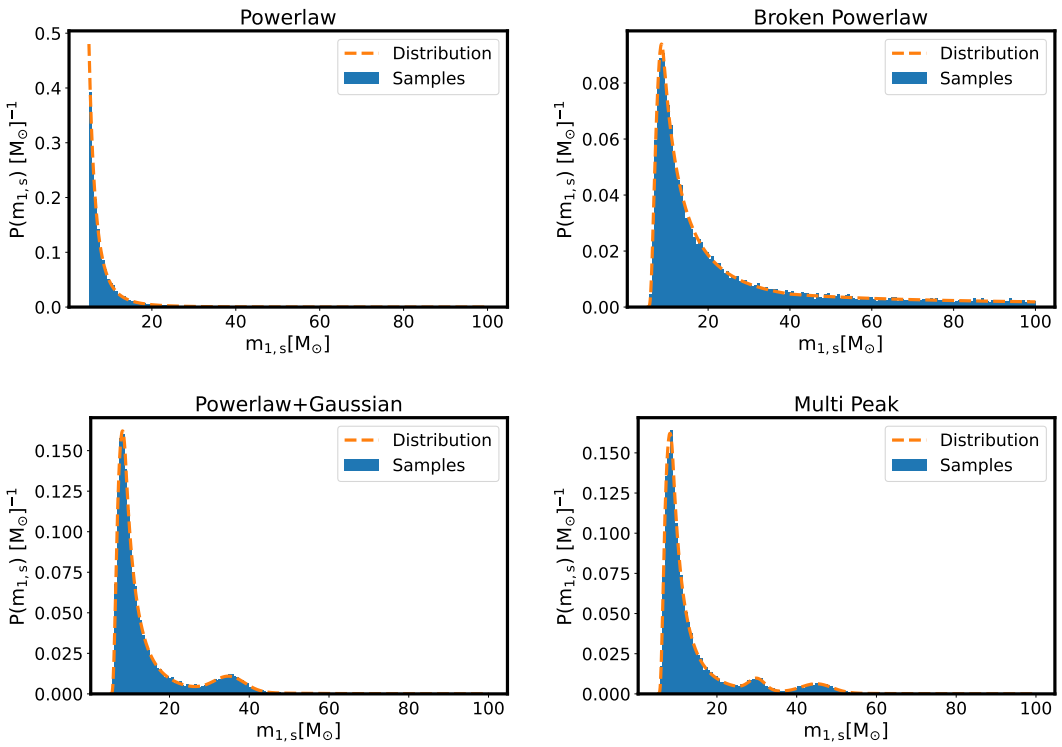

Figure 5.3: The various source frame mass models distributions implemented in GWSim [103]. The analytical forms are presented as orange dashed curves where the samples drawn from them are histogrammed in blue. Top left: A truncated power law model. Top right: A broken power law model with smoothing at the lower end of the distribution. Bottom left: A power law+Gaussian peak model with smoothing at the lower end of the distribution. Bottom right: A multi peak model with smoothing at the lower end of the distribution.

the formation of the stars and the merging of the BBHs, which was described in Sec. 4.4, is also implemented inside GWSim.

5.2.3 Merger Rate Models

Concerning the merger rate models, GWSim is able to successfully sample the model described in Eq. 3.11. In the left plot of Fig. 5.5 one can see that the samples drawn from the aforementioned merger rate distribution (histogrammed in blue) do match the analytical form of the distribution (orange dashed curve). The parameters of the distribution were fixed to the values inferred from the star formation rate. In the right plot of Fig. 5.5 we see the samples drawn from the merger rate model that was described in Sec. 4.4. Again the code can generate correctly the distribution and return samples

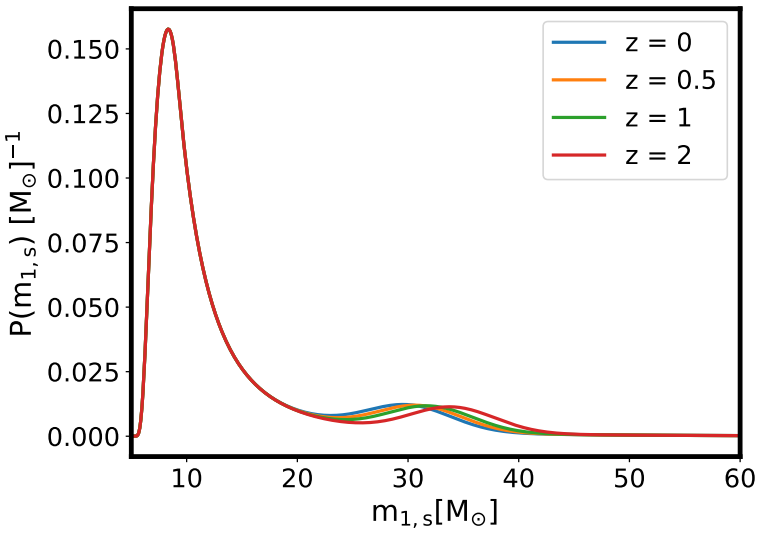

Figure 5.4: An example of the linear redshift dependent mass models that are implemented inside GWSim [103]. Here we chose the power law+Gaussian peak mass distribution and allowed only the position of the peak to vary with redshift, while keeping the rest of the model parameters fixed and non evolving. The evolution parameter was set to $\epsilon_{\mu_g} = 2\ M_\odot$.

that match the analytical form.

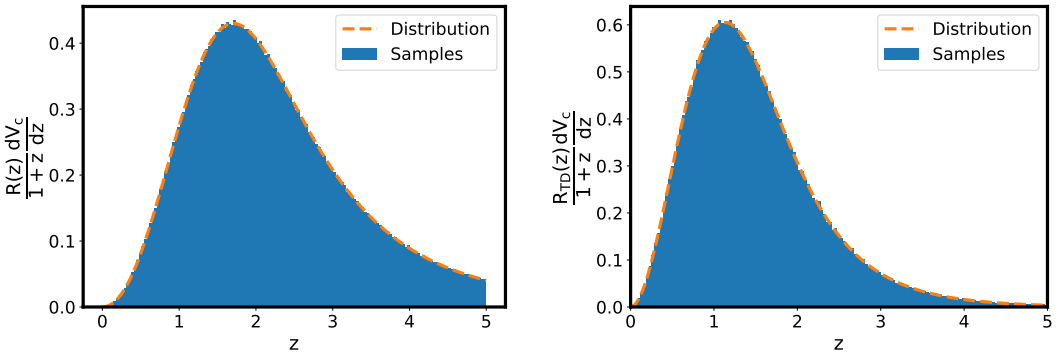

Figure 5.5: Redshift samples GWSim draws from the merger rate distributions [103]. Left: The merger rate model given by Eq.3.11. Right: The merger rate model given by Eq.4.19.

5.2.4 Spin Models

Up to this point we have ignored the rotations of BHs and the information we can get from them. Spins of BHs are expected to have a less significant effect on cosmological parameters estimations, with respect to, for example, the effect of the mass distribution

and the values of its parameters. However, for the next observing run they should be included in the analysis and contribute to the population and cosmological parameter estimation. Therefore, we have included some basic spin distribution models in GWSim, so it is able to create simulations of GWTCs that do include rotating BHs, if the user wants.

Spins of BHs are usually depicted as dimensionless parameters. A spinning BH of mass m and spin $\vec{S} = S\hat{S}$, where $|\hat{S}|$=1, can not spin faster than:

$$S \leq \frac{Gm^2}{c}. \tag{5.2}$$

Using this relation we can define the dimensionless spin parameter as:

$$\chi = \frac{cS}{Gm^2}. \tag{5.3}$$

Assuming that we have a BBH with BHs of masses m_1, m_2 and spins χ_1, χ_2, we can define an effective aligned-spin parameter χ_{eff} as:

$$\chi_{\text{eff}} = \frac{\chi_1 \cos\theta_1 + q\chi_2 \cos\theta_2}{1+q}, \tag{5.4}$$

where $q = \frac{m_2}{m_1}$, $\cos\theta_{(1,2)} = \hat{S_{(1,2)}}\hat{J}$ and $\hat{J}$ is the unit vector along the direction of the total angular momentum of the binary system. Now that we defined those useful parameters we can describe the spin models that are included currently in the GWSim code. The first model is a simple uniform distribution for χ_{eff}. The values for $\chi_{1,2}$ are selected accordingly in order for the χ_{eff} to follow a uniform distribution. The second model is a heavy mass focused model, spins are set to zero for all events with m_1 smaller than a mass threshold (selected by the user) and for the rest, $\chi_{1,2}$ are sampled from uniform distributions. Next is a Gaussian peak distribution for χ_{eff} where $\chi_{1,2}$ are selected accordingly. Finally, the last model correlates spins parameters with masses, as introduced in Ref. [108]. The χ_1, χ_2 and χ_{eff} distributions in the case of the mass correlated model can be seen in Fig. 5.6. All the available models of the code can be seen in Fig. 5.7 and the parameters that govern each model can be seen in Tabs. 5.1

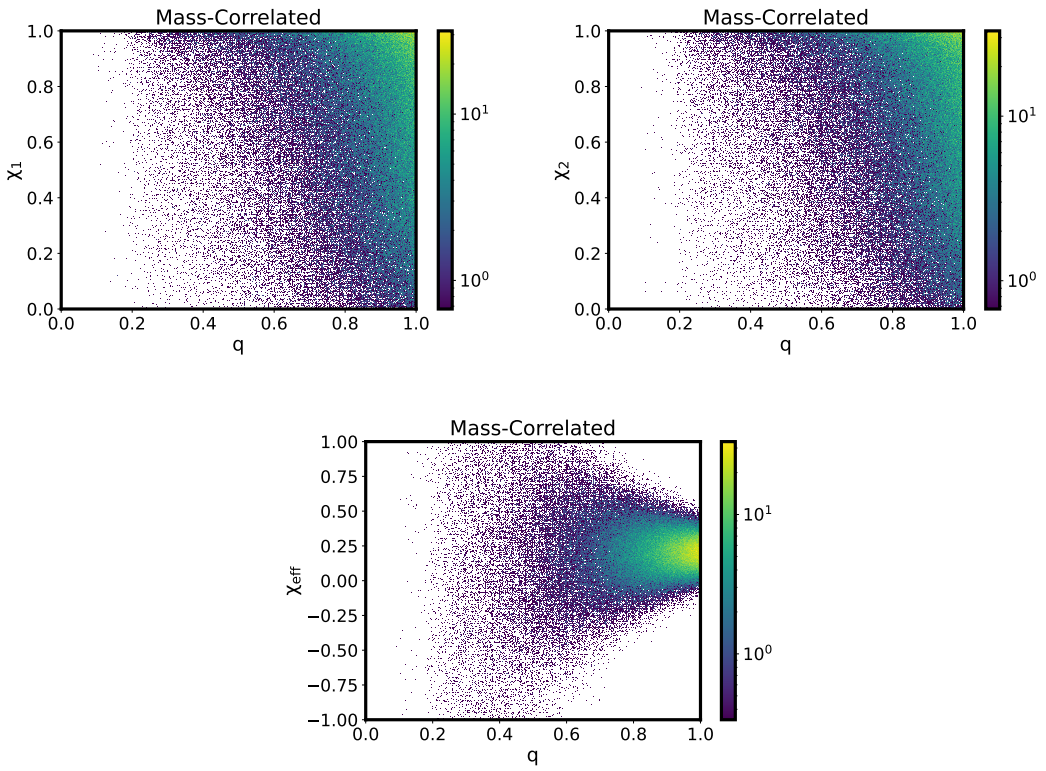

Figure 5.6: The spin sampling for the case of the mass correlated model [103]. Top left: Scatter plot of samples in χ_1-mass ratio space. Top right: Scatter plot of samples in χ_2-mass ratio space. Bottom: Scatter plot of samples in $\chi_{eff}-$mass ratio space. The distributions were calculated with $\alpha_s = 0.013, \beta_s = -1.53, \chi_0 = 0.2, \sigma_0 = 0.52$. The mass distribution was the power law+Gaussian distribution.

and 5.2.

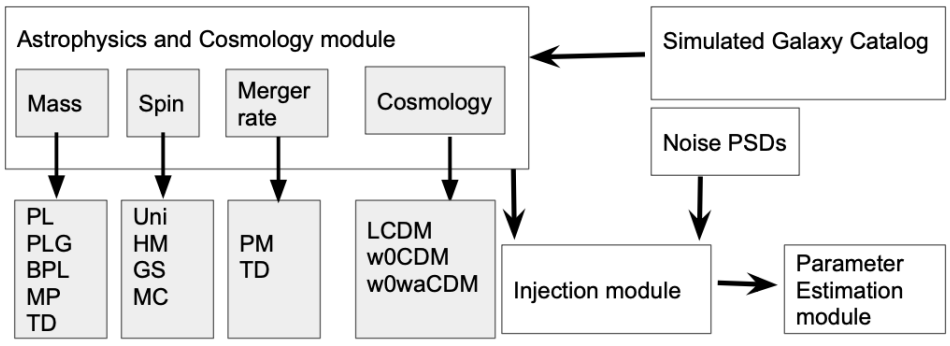

Figure 5.7: Flowchart of the GWSim code with the available models [103].

Models considered

Merger rate models

Model	Parameters
Redshift independent :	$R_0, \gamma = 0, \kappa = 0, z_p = 0$
Redshift dependent :	R_0, γ, κ, z_p

Mass models

Model	Parameters
Truncated powerlaw	$\alpha, \beta, M_{\rm min}, M_{\rm max}$
Broken powerlaw	$\alpha, \alpha_2, \beta, M_{\rm min}, M_{\rm max}, \delta_m, b$
Powerlaw+Gaussian	$\alpha, \beta, M_{\rm min}, M_{\rm max}, \delta_m, \mu_g, \sigma_g, \lambda_g$
Multi peak:	$\alpha, \beta, M_{\rm min}, M_{\rm max}, \delta_m, \mu_g, \sigma_g, \lambda_g, \mu_{\rm g,low}, \sigma_{\rm g,low}, \lambda_{\rm g,low}$
Redshift dependent	All parameters of the selected model+one ϵ for each parameter.

Spin models

Model	Parameters
Uniform	–
Gaussian	χ_0, σ_0
Heavy mass	m_{th}
Correlated	$\alpha_s, \beta_s, \chi_0, \sigma_0$

Time delay model

Model	Parameters
Time delay	$R_0, \gamma = 2.7, \kappa = 2.9, z_p = 1.9, \alpha, \beta, M_{\rm min}, M_{\rm max}, \delta_m,$ $M_{PISN}(Z_*), \sigma_g, \lambda_g, d, t_d^{min}, \alpha_Z, \gamma_Z$

Table 5.1: Description of the mass and spin models available and the parameters that govern them [103].

5.3 Simulated Gravitational Waves Transient Catalogue

We used GWSim to produce a simulated GWTC of three years of observation time using a universe file. This simulation is similar to what we should expect after the next LVK run (O4). The cosmology was selected to be a fiducial flat ΛCDM model with $H_0 = 67.8$ km/s/Mpc and $\Omega_m = 0.3$. The noise of the detectors was fixed to the real ones deduced from the O1, O2 and O3 observational runs and the expected one for O4. The merger rate model was selected to be that of Eq. 3.11 with parameters fixed to the star formation rate values and R_0 was selected to be $R_0 = 20$ Gpc^{-3} yr^{-1}. The mass distribution was selected to be a power law+Gaussian peak distribution with values for the parameters similar to those deduced in the analysis in the previous chapter. The spins of all events were kept fixed to zero. With these choices, the total number

Cosmology

Definition of the cosmological parameters

Parameter	Description
H_0	The Hubble constant in km/s/Mpc.
Ω_m	Present-day matter density of the Universe.
$w(z) = w_0 + w_a(\frac{z}{1+z})$	Dark energy equation of state and its redshift dependence.

Cosmological models considered

Model	Parameters
Flat ΛCDM :	H_0, Ω_m, $w_0 = -1$, $w_a = 0$
Flat w_0CDM :	H_0, Ω_m, w_0, $w_a = 0$
Flat w_0-w_aCDM :	H_0, Ω_m, w_0, w_a

Table 5.2: Description of the cosmological models available and the parameters that govern them [103].

of simulated events was more than 200 thousand, from which only around 150 events were detected, with an SNR threshold of $\text{SNR}_{thr} = 12$. The distributions of the masses m_1, m_2 and redshift z of all the simulated events can be seen in Fig. 5.8 as blue solid curves. In the same plots the distribution of only the detected events are also depicted as orange solid curves.

We use BILBY to perform parameter estimation for the detected events in order to obtain posterior distributions for the BHs parameters. The posteriors obtained from one of the events of the simulated GWTC can be seen in Fig. 5.9. In the plot the posterior we obtained for the masses of the BHs, m_1, m_2, the luminosity distance , D_L, the position in the sky, RA, Dec and the inclination θ_{JN}, are presented. The injected values for each parameter are shown as black dashed lines.

Having a set of posterior samples for all events in our simulated GWTC allows to test pipelines meant to estimate the cosmology. In the next chapter we will use one of the pipelines that was mentioned before for the O3 results to try and get back the injected values.

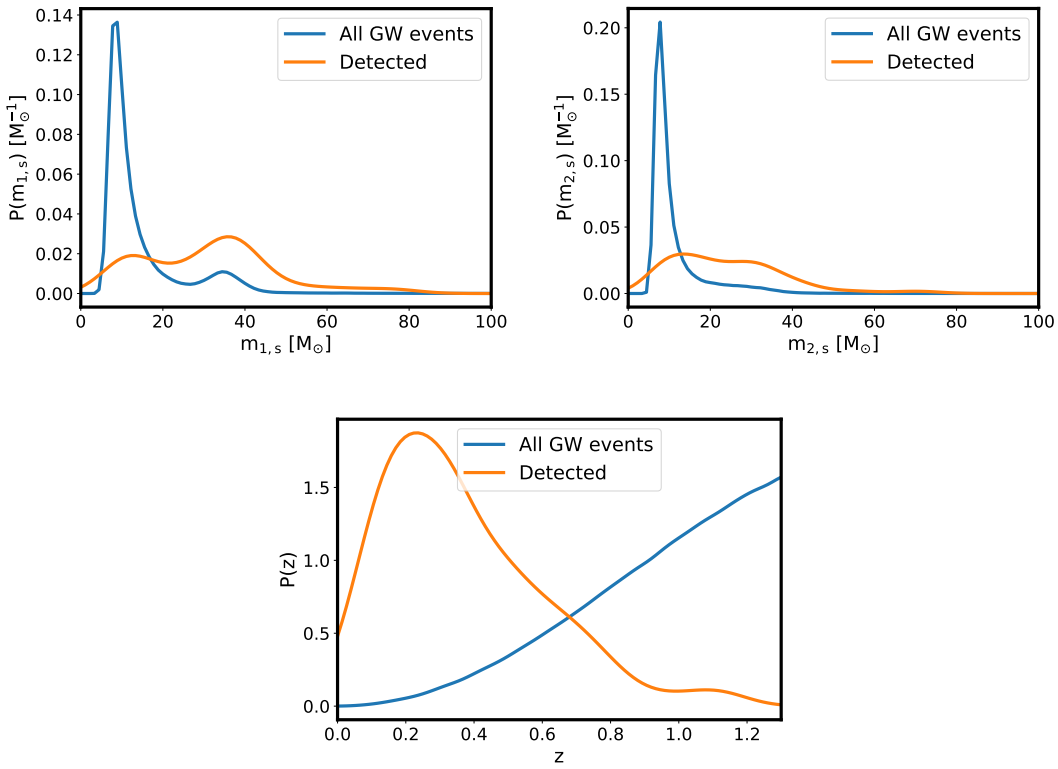

Figure 5.8: Primary component masses (top left) and lighter component masses (top right) distributions in the source frame of the detected events' parameters for a simulation of O1 to O4 with a total duration of three observational years. The redshifts (bottom) distribution of the events is also shown. The network SNR threshold was set to $\mathrm{SNR}_{thr} = 12$. In the same plots, the distribution of all the simulated (detected and not detected) events can be seen. The cosmology was selected to be a fiducial flat ΛCDM model with $H_0 = 67.8$ km/s/Mpc and $\Omega_m = 0.3$ [103].

5.3.1 Inference of Population and Cosmological Parameters

We will use the pipeline described in Sec. 3.2 and load the posteriors from our simulated GTWC and try to retrieve the injected values. The distribution of the posterior samples that we retrieved as well as the distributions of the true injected values for $m_{1,d}$, $m_{2,d}$ and D_L can be seen in Fig. 5.10 and in Fig. 5.11. We observe that the distributions are in agreement, modulo some statistical variations that originate from the PE process. We use now the pipeline that can estimate conjointly the population and cosmological parameters. We use a flat ΛCDM with a fixed density of matter to the value that was used for the injections, and we allow only H_0 to vary. We obtain the posteriors that can be seen in Fig. 5.12. As it can be seen, most of the parameters are within

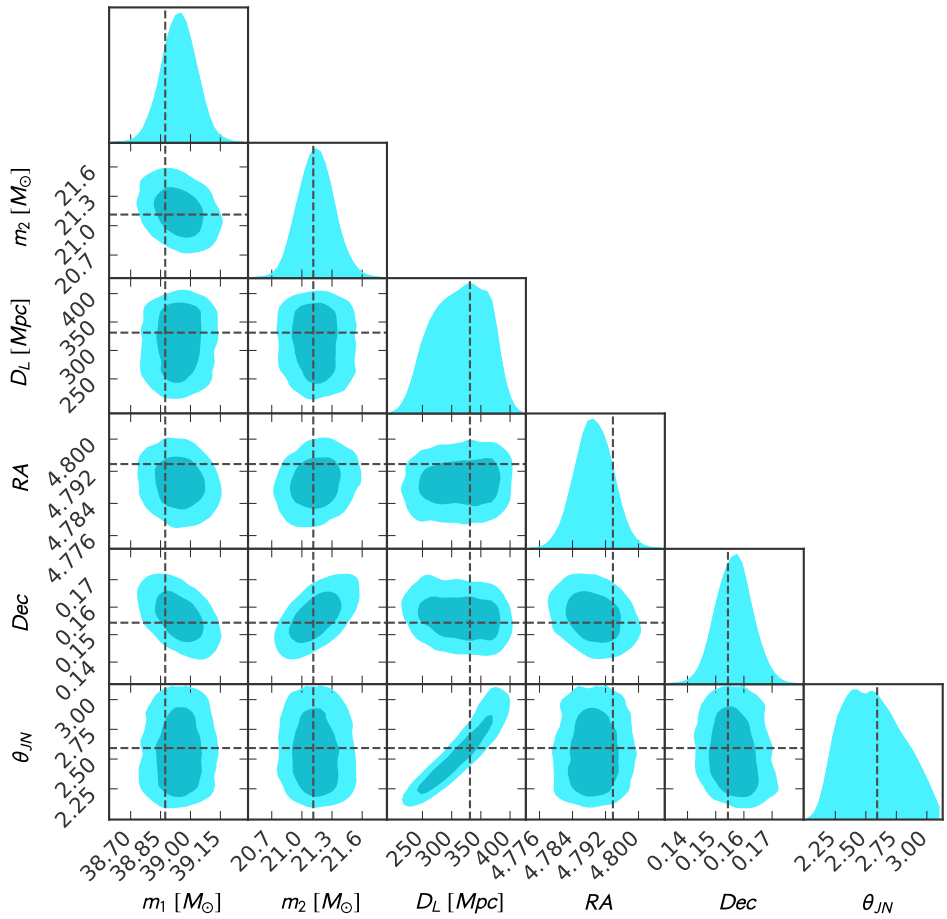

Figure 5.9: Parameter estimation posteriors of one randomly selected event using BILBY. The parameters from top to bottom are: $m_1, m_2, D_L, RA, Dec, \theta_{JN}$. The injected values for the parameters are presented with dashed black lines [103].

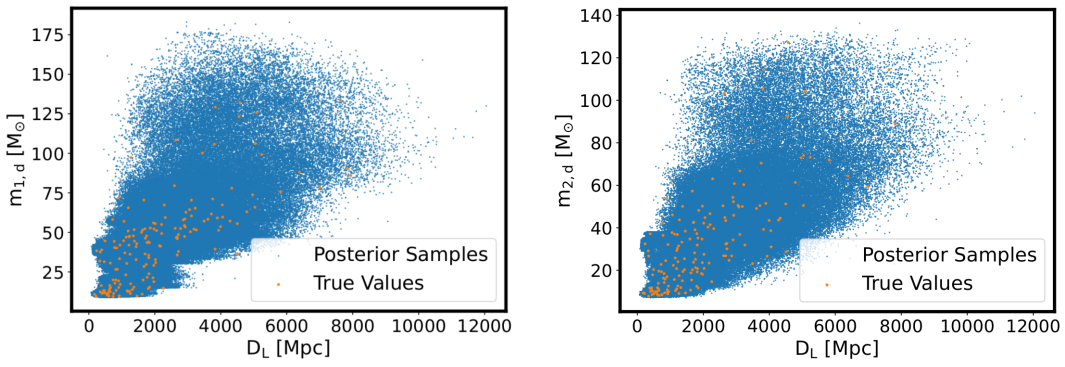

Figure 5.10: Posterior samples distributions for $m_{1,d}$ (left) and $m_{2,d}$ (right) for a simulation of O1 to O4 with a total duration of three observational years, as a function of luminosity distance [103]. The network SNR threshold was set to $\mathrm{SNR_{thr}} = 12$. In the same plots, the distribution of all the true values of the events can be seen.

the 2σ estimations. In reality, galaxy catalog information will also be used in the cosmological pipelines, so constraints on parameters will be better in O4. Here we have used only information that comes from our population assumptions solely. GWSim will be updated later in order to be able to handle real galaxy catalogues and deal with their incompleteness.

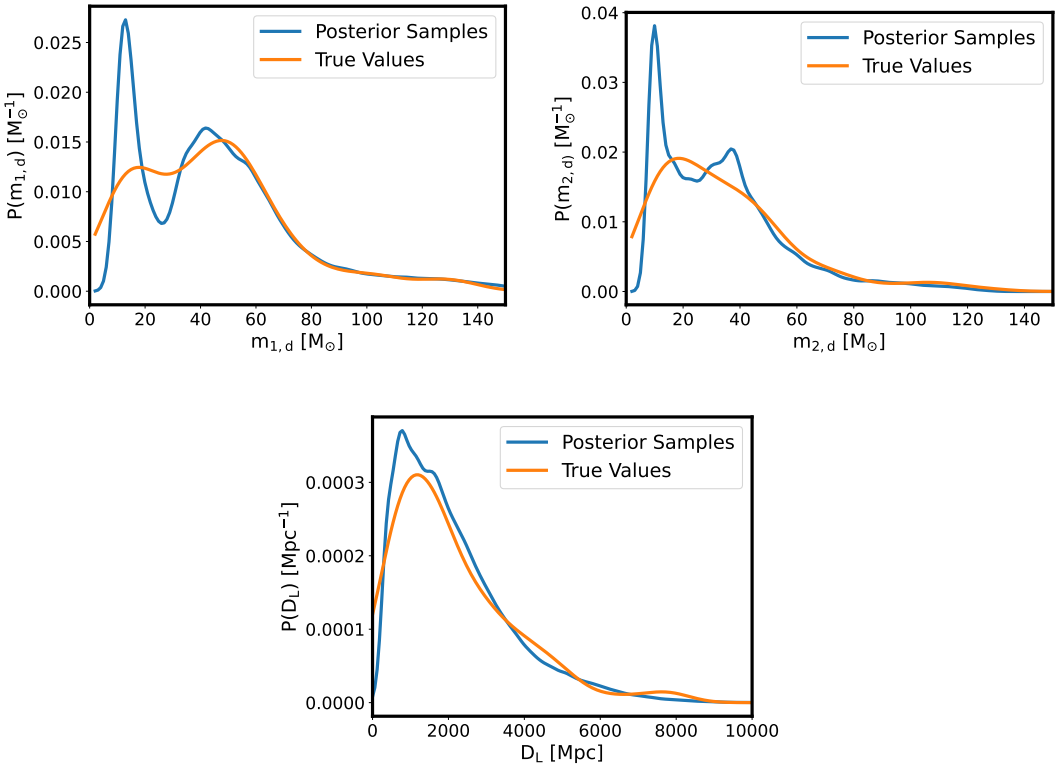

Figure 5.11: Primary component masses (top left) and lighter component masses (top right) posterior samples distributions in the detector frame of the detected events' parameters for a simulation of O1 to O4 with a total duration of three observational years [103]. The luminosity distance (bottom) distribution of the events is also shown. The network SNR threshold was set to $\mathrm{SNR}_{thr} = 12$. In the same plots, the distribution of all the injected (true) values of the events can be seen. The cosmology was selected to be a fiducial flat ΛCDM model with $H_0 = 67.8$ km/s/Mpc and $\Omega_m = 0.3$.

Estimations of parameters can still be outside the 1σ region (or even the 2σ in rare cases) since the many parameters are correlated and the number of events is small. In addition to variation coming from the PE process, there is an inherited randomness in the detected events that might cause deviations in the estimations of parameters. This can be seen in Fig. 5.13 which shows the distributions of m_1 (top) and m_2 (bottom) for

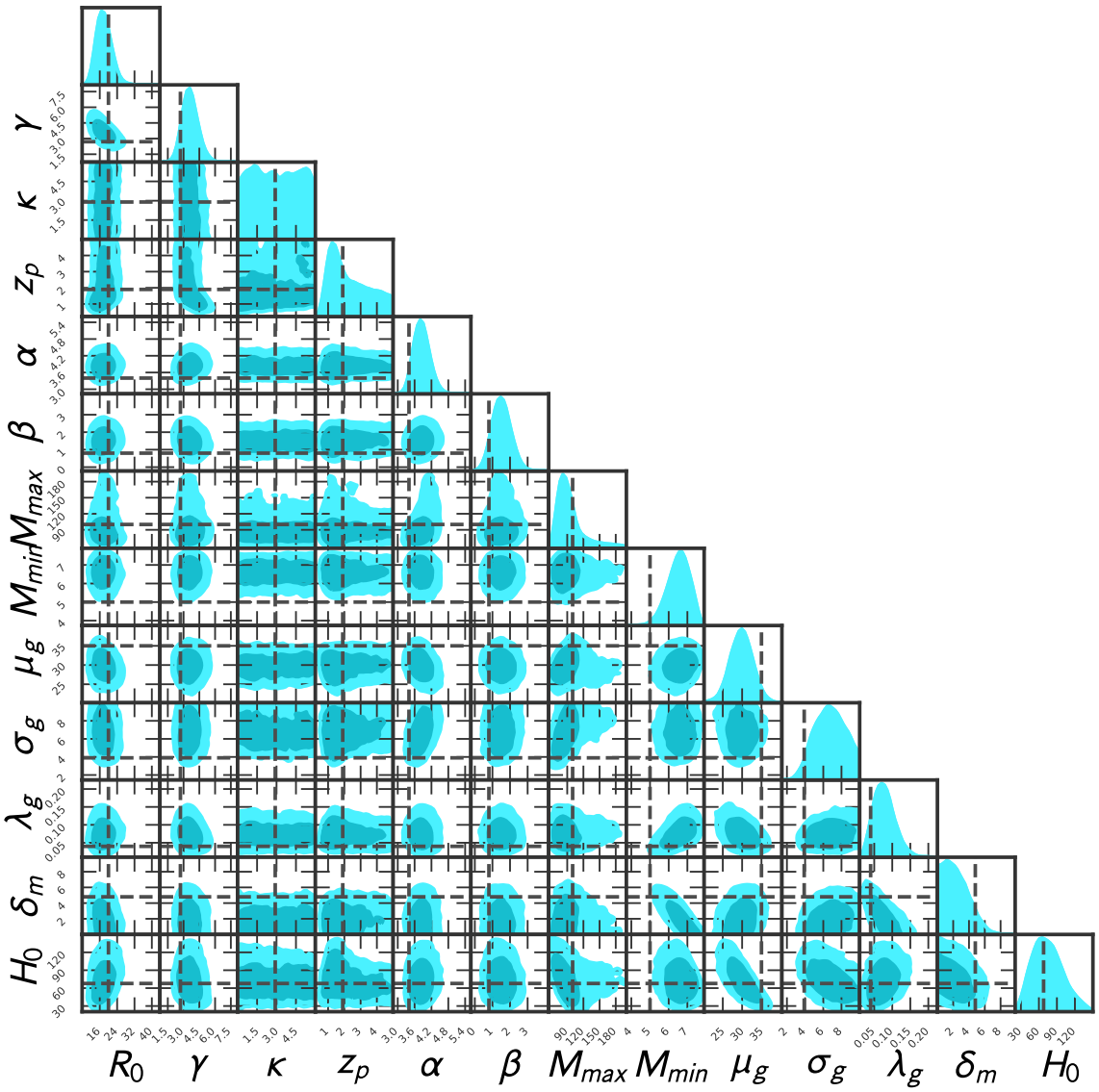

Figure 5.12: Posteriors of population parameters and H_0 for a simulated O1 to O4 GWTC [103]. The injected values for the parameters are presented with dashed black lines.

50 different injection sets. In the leftmost plots we see the distributions for a total of 3 observational years (same as the injection set for which results were presented previously). In this case, one can observe that the distributions vary a lot, especially the ones of m_2. By raising the observational time and using the same O1 to O4 sensitivities, the number of the detected events increases. For the selected cosmology and population parameters, we obtain around 1000 detected events with an $\mathrm{SNR}_{thr} > 12$. In the rightmost of Fig. 5.13 the distribution in the case of 20 observational years can be seen. As it is apparent,

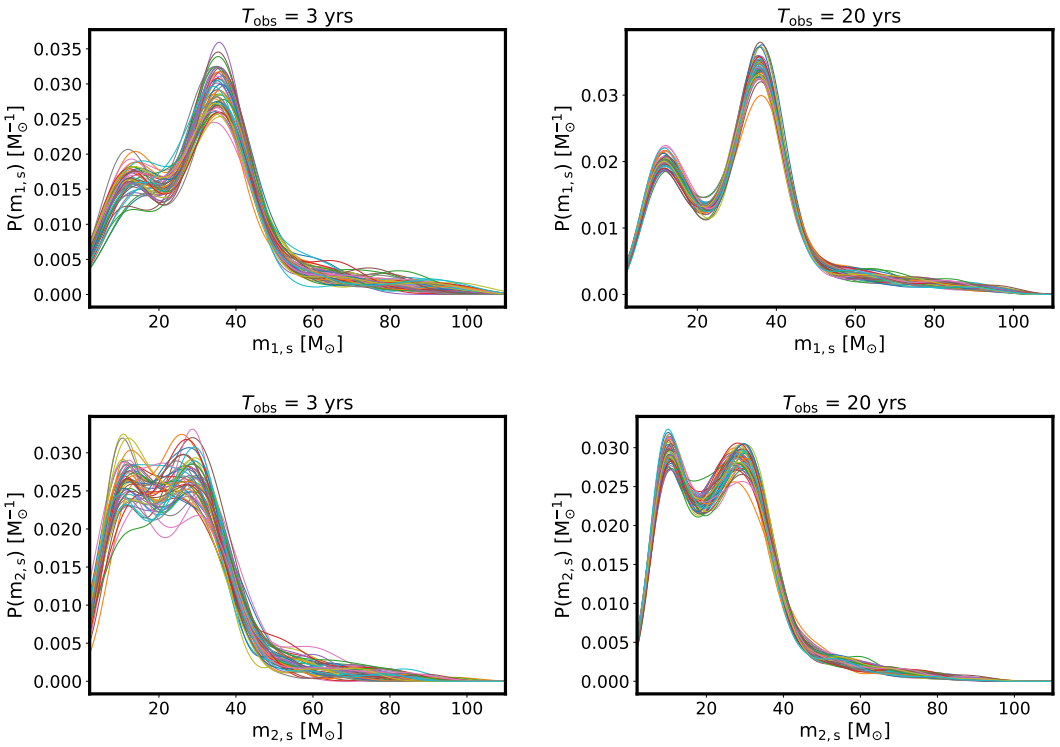

Figure 5.13: Various m_1 (top) and m_2 (bottom) distributions of the detected events with SNR > 12 for $T_{\rm obs} = 3$ years (left) and $T_{\rm obs} = 20$ years (right) produced for different random seeds. Raising the total observational time leads to more events being detected and the distributions being better defined [103].

the distributions in this case are much better defined and the constraints on population parameters will be better.

GWSim will be useful for testing purposes of cosmological and/or population pipelines, as well as making predictions of future measurement's precision. Next generation interferometers will also be added into GWSim.

Chapter 6

Conclusions

In this document, I presented all the work and research I did during my PhD. I was involved into various astrophysical and cosmological analyses using gravitational waves data. My PhD led to several short author and wide LIGO-Virgo-Kagra journal publications.

I was involved into the noise hunting of the Virgo detector that took place in the commissioning break between the O3a and O3b observational runs. Our contribution helped locating the sources of various noises that were previously unknown, and were affecting the sensitivity of the detector. I was also involved in the installation of the first instrumented baffle that was placed in the Virgo detector and the monitoring of its response. The measurements provided by this device were compared to various scattered light simulations.

On the physics side of the analyses, I was involved in the cosmological group of the LIGO-Virgo-Kagra collaboration. I contributed to the development of the cosmological pipelines, both using or not galaxy catalogues. This led to two collaboration papers presenting the best constraint up to date for the Hubble constant using dark sirens. The research on the cosmological parameters estimation led also to a deeper understanding of the importance of population parameters of the black holes, which is also of astrophysical interest. We developed a new model that starts from first principles and arrives at the mass distribution of black holes in the Universe. This is done by considering the time delay between formation of stars and the merging of binary black holes. We also

explored the information and constraints we get on parameters of models beyond General Relativity using gravitational waves data.

Finally, I also developed a pipeline that can simulate gravitational waves transient catalogues. The user can select to simulate data for various cosmological models, mass models and many more. The pipeline is useful since it can be used to perform predictions for results that we expect from future observational runs and also can be used to identify systematic uncertainties in other pipelines/methods.

Bibliography

[1] M. Maggiore. *Gravitational Waves. Vol. 1: Theory and Experiments*. Oxford Master Series in Physics. Oxford University Press, 2007. ISBN: 978-0-19-857074-5, 978-0-19-852074-0.

[2] S. M. Carroll. *Spacetime and Geometry*. Cambridge University Press, July 2019. ISBN: 978-0-8053-8732-2, 978-1-108-48839-6, 978-1-108-77555-7.

[3] E. Di Valentino and et al. "Snowmass2021 - Letter of interest cosmology intertwined II: The hubble constant tension". In: *Astroparticle Physics* 131 (2021), p. 102605. ISSN: 0927-6505. DOI: https://doi.org/10.1016/j.astropartphys.2021.102605. URL: https://www.sciencedirect.com/science/article/pii/S0927650521000499.

[4] V. Bonvin and M. Millon. Source code available at https://github.com/ vbonvin/H0_tension.

[5] Planck Collaboration and et al. "Planck 2018 results - VI. Cosmological parameters". In: *A&A* 641 (2020), A6. DOI: 10.1051/0004-6361/201833910. URL: https://doi.org/10.1051/0004-6361/201833910.

[6] A. G. Riess and et al. "Large Magellanic Cloud Cepheid Standards Provide a 1% Foundation for the Determination of the Hubble Constant and Stronger Evidence for Physics beyond ΛCDM". In: *The Astrophysical Journal* 876.1 (May 2019), p. 85. DOI: 10.3847/1538-4357/ab1422. URL: https://doi.org/10.3847/1538-4357/ab1422.

[7] S. Mastrogiovanni and et al. "Gravitational wave friction in light of GW170817 and GW190521". In: *Journal of Cosmology and Astroparticle Physics* 2021.02

(Feb. 2021), pp. 043–043. DOI: 10.1088/1475-7516/2021/02/043. URL: https://doi.org/10.1088%5C%2F1475-7516%5C%2F2021%5C%2F02%5C%2F043.

[8] K. et al. Leyde. *Current and future constraints on cosmology and modified gravitational wave friction from binary black holes*. 2022. DOI: 10.48550/ARXIV.2202.00025. URL: https://arxiv.org/abs/2202.00025.

[9] I. D. Saltas and et al. "Anisotropic Stress as a Signature of Nonstandard Propagation of Gravitational Waves". In: *Physical Review Letters* 113.19 (Nov. 2014). DOI: 10.1103/physrevlett.113.191101. URL: https://doi.org/10.1103%5C%2Fphysrevlett.113.191101.

[10] M. Lagos and et al. "Standard sirens with a running Planck mass". In: *Physical Review D* 99.8 (Apr. 2019). DOI: 10.1103/physrevd.99.083504. URL: https://doi.org/10.1103%5C%2Fphysrevd.99.083504.

[11] E. Belgacem and et al. "Modified gravitational-wave propagation and standard sirens". In: *Physical Review D* 98.2 (July 2018). DOI: 10.1103/physrevd.98.023510. URL: https://doi.org/10.1103%5C%2Fphysrevd.98.023510.

[12] G. W. Horndeski. "Second-order scalar-tensor field equations in a four-dimensional space". In: *Int. J. Theor. Phys.* 10 (1974), pp. 363–384. DOI: 10.1007/BF01807638.

[13] C. Deffayet and et al. "From k-essence to generalized Galileons". In: *Physical Review D* 84.6 (Sept. 2011). DOI: 10.1103/physrevd.84.064039. URL: https://doi.org/10.1103%5C%2Fphysrevd.84.064039.

[14] J. Gleyzes and et al. "New Class of Consistent Scalar-Tensor Theories". In: *Physical Review Letters* 114.21 (May 2015). DOI: 10.1103/physrevlett.114.211101. URL: https://doi.org/10.1103%5C%2Fphysrevlett.114.211101.

[15] D. Langlois and K. Noui. "Degenerate higher derivative theories beyond Horndeski: evading the Ostrogradski instability". In: *Journal of Cosmology and Astroparticle Physics* 2016.02 (Feb. 2016), pp. 034–034. DOI: 10.1088/1475-7516/2016/02/034. URL: https://doi.org/10.1088%5C%2F1475-7516%5C%2F2016%5C%2F02%5C%2F034.

[16] E. Belgacem and et al. "Testing modified gravity at cosmological distances with LISA standard sirens". In: *Journal of Cosmology and Astroparticle Physics* 2019.07 (July 2019), pp. 024–024. DOI: 10.1088/1475-7516/2019/07/024. URL: https://doi.org/10.1088%5C%2F1475-7516%5C%2F2019%5C%2F07%5C%2F024.

[17] M. Corman and et al. "Constraining cosmological extra dimensions with gravitational wave standard sirens: From theory to current and future multimessenger observations". In: *Physical Review D* 105.6 (Mar. 2022). DOI: 10.1103/physrevd.105.064061. URL: https://doi.org/10.1103%5C%2Fphysrevd.105.064061.

[18] G. Dvali and et al. "4D gravity on a brane in 5D Minkowski space". In: *Physics Letters B* 485.1-3 (July 2000), pp. 208–214. DOI: 10.1016/s0370-2693(00)00669-9. URL: https://doi.org/10.1016%5C%2Fs0370-2693%5C%2800%5C%2900669-9.

[19] G. Calcagni and et al. "Gravitational-wave luminosity distance in quantum gravity". In: *Physics Letters B* 798 (Nov. 2019), p. 135000. DOI: 10.1016/j.physletb.2019.135000. URL: https://doi.org/10.1016%5C%2Fj.physletb.2019.135000.

[20] C. Deffayet and K. Menou. "Probing Gravity with Spacetime Sirens". In: *The Astrophysical Journal* 668.2 (Oct. 2007), pp. L143–L146. DOI: 10.1086/522931. URL: https://doi.org/10.1086%5C%2F522931.

[21] B. P. Abbott and et al. "Observation of Gravitational Waves from a Binary Black Hole Merger". In: *Phys. Rev. Lett.* 116 (6 Feb. 2016), p. 061102. DOI: 10.1103/PhysRevLett.116.061102. URL: https://link.aps.org/doi/10.1103/PhysRevLett.116.061102.

[22] L. Tianjun and et al. "Measurements of mechanical thermal noise and energy dissipation in optical dielectric coatings". In: *Physical Review D* 89.9 (May 2014). DOI: 10.1103/physrevd.89.092004. URL: https://doi.org/10.1103%5C%2Fphysrevd.89.092004.

[23] F. Acernese and et al. "Advanced Virgo: a second-generation interferometric gravitational wave detector". In: *Classical and Quantum Gravity* 32.2 (Dec. 2014),

p. 024001. DOI: 10.1088/0264-9381/32/2/024001. URL: https://doi.org/10.1088%5C%2F0264-9381%5C%2F32%5C%2F2%5C%2F024001.

[24] J. Aasi and et al. "Advanced LIGO". In: *Classical and Quantum Gravity* 32.7 (Mar. 2015), p. 074001. DOI: 10.1088/0264-9381/32/7/074001. URL: https://doi.org/10.1088%5C%2F0264-9381%5C%2F32%5C%2F7%5C%2F074001.

[25] P. R. Saulson. *Fundamentals of Interferometric Gravitational Wave Detectors*. 2nd. ed. World Scientific, 2017. ISBN: 978-981-314-307-4, 978-981-314-620-4. DOI: 10.1142/10116.

[26] I. Fiori and et al. "The Hunt for Environmental Noise in Virgo during the Third Observing Run". In: *Galaxies* 8.4 (2020). ISSN: 2075-4434. DOI: 10.3390/galaxies8040082. URL: https://www.mdpi.com/2075-4434/8/4/82.

[27] O. Ballester and et al. "Measurement of the stray light in the Advanced Virgo input mode cleaner cavity using an instrumented baffle". In: *Classical and Quantum Gravity* 39.11 (May 2022), p. 115011. DOI: 10.1088/1361-6382/ac6a9d. URL: https://doi.org/10.1088%5C%2F1361-6382%5C%2Fac6a9d.

[28] S. Mastrogiovanni and et al. "Cosmology in the dark: On the importance of source population models for gravitational-wave cosmology". In: *Physical Review D* 104.6 (Sept. 2021). DOI: 10.1103/physrevd.104.062009. URL: https://doi.org/10.1103%5C%2Fphysrevd.104.062009.

[29] P. Madau and M. Dickinson. "Cosmic Star-Formation History". In: *Annual Review of Astronomy and Astrophysics* 52.1 (Aug. 2014), pp. 415–486. DOI: 10.1146/annurev-astro-081811-125615. URL: https://doi.org/10.1146%5C%2Fannurev-astro-081811-125615.

[30] B. P. Abbott and et al. "A gravitational-wave standard siren measurement of the Hubble constant". In: *Nature* 551.7678 (Oct. 2017), pp. 85–88. DOI: 10.1038/nature24471. URL: https://doi.org/10.1038%5C%2Fnature24471.

[31] H. Y. Chen and et al. "A two per cent Hubble constant measurement from standard sirens within five years". In: *Nature* 562.7728 (Oct. 2018), pp. 545–547. DOI:

10.1038/s41586-018-0606-0. URL: https://doi.org/10.1038%5C%2Fs41586-018-0606-0.

[32] I. Mandel and et al. "Extracting distribution parameters from multiple uncertain observations with selection biases". In: *Monthly Notices of the Royal Astronomical Society* 486.1 (Mar. 2019), pp. 1086–1093. DOI: 10.1093/mnras/stz896. URL: https://doi.org/10.1093%5C%2Fmnras%5C%2Fstz896.

[33] S. Vitale and et al. "Inferring the Properties of a Population of Compact Binaries in Presence of Selection Effects". In: *Handbook of Gravitational Wave Astronomy*. Springer Singapore, 2021, pp. 1–60. DOI: 10.1007/978-981-15-4702-7_45-1. URL: https://doi.org/10.1007%5C%2F978-981-15-4702-7_45-1.

[34] K. M. Górski and et al. "HEALPix: A Framework for High-Resolution Discretization and Fast Analysis of Data Distributed on the Sphere". In: 622 (Apr. 2005), pp. 759–771. DOI: 10.1086/427976. eprint: arXiv:astro-ph/0409513.

[35] A. Zonca and et al. "healpy: equal area pixelization and spherical harmonics transforms for data on the sphere in Python". In: *Journal of Open Source Software* 4.35 (Mar. 2019), p. 1298. DOI: 10.21105/joss.01298. URL: https://doi.org/10.21105/joss.01298.

[36] B. F. Schutz. "Determining the Hubble constant from gravitational wave observations". In: 323.6086 (Sept. 1986), pp. 310–311. DOI: 10.1038/323310a0.

[37] D. E. Holz and S. A. Hughes. "Using Gravitational-Wave Standard Sirens". In: *The Astrophysical Journal* 629.1 (Aug. 2005), pp. 15–22. DOI: 10.1086/431341. URL: https://doi.org/10.1086%5C%2F431341.

[38] N. Dalal and et al. "Short GRB and binary black hole standard sirens as a probe of dark energy". In: *Physical Review D* 74.6 (Sept. 2006). DOI: 10.1103/physrevd.74.063006. URL: https://doi.org/10.1103%5C%2Fphysrevd.74.063006.

[39] S. Nissanke and et al. "EXPLORING SHORT GAMMA-RAY BURSTS AS GRAVITATIONAL-WAVE STANDARD SIRENS". In: *The Astrophysical Journal* 725.1 (Nov. 2010), pp. 496–514. DOI: 10.1088/0004-637x/725/1/496. URL: https://doi.org/10.1088%5C%2F0004-637x%5C%2F725%5C%2F1%5C%2F496.

[40] B. S. Sathyaprakash and et al. "Cosmography with the Einstein Telescope". In: *Classical and Quantum Gravity* 27.21 (Sept. 2010), p. 215006. DOI: 10.1088/0264-9381/27/21/215006. URL: https://doi.org/10.1088/0264-9381/27/21/215006.

[41] W. Del Pozzo. "Inference of cosmological parameters from gravitational waves: Applications to second generation interferometers". In: *Physical Review D* 86.4 (Aug. 2012). DOI: 10.1103/physrevd.86.043011. URL: https://doi.org/10.1103%5C%2Fphysrevd.86.043011.

[42] S. Nissanke and et al. "Determining the Hubble constant from gravitational wave observations of merging compact binaries". In: *arXiv e-prints*, arXiv:1307.2638 (July 2013), arXiv:1307.2638. arXiv: 1307.2638 [astro-ph.CO].

[43] M. Soares-Santos and et al. "First Measurement of the Hubble Constant from a Dark Standard Siren using the Dark Energy Survey Galaxies and the LIGO/Virgo Binary–Black-hole Merger GW170814". In: *The Astrophysical Journal* 876.1 (Apr. 2019), p. L7. DOI: 10.3847/2041-8213/ab14f1. URL: https://doi.org/10.3847/2041-8213/ab14f1.

[44] G. Dálya and et al. "GLADE: A galaxy catalogue for multimessenger searches in the advanced gravitational-wave detector era". In: *Monthly Notices of the Royal Astronomical Society* 479.2 (June 2018), pp. 2374–2381. DOI: 10.1093/mnras/sty1703. URL: https://doi.org/10.1093%5C%2Fmnras%5C%2Fsty1703.

[45] R. Gray and et al. "Cosmological inference using gravitational wave standard sirens: A mock data analysis". In: *Physical Review D* 101.12 (June 2020). DOI: 10.1103/physrevd.101.122001. URL: https://doi.org/10.1103%5C%2Fphysrevd.101.122001.

[46] B. P. Abbott and et al. "A Gravitational-wave Measurement of the Hubble Constant Following the Second Observing Run of Advanced LIGO and Virgo". In: *The Astrophysical Journal* 909.2 (Mar. 2021), p. 218. DOI: 10.3847/1538-4357/abdcb7. URL: https://doi.org/10.3847%5C%2F1538-4357%5C%2Fabdcb7.

[47] P. Schechter. "An analytic expression for the luminosity function for galaxies." In: 203 (Jan. 1976), pp. 297–306. DOI: 10.1086/154079.

[48] R. Gray and et al. "A pixelated approach to galaxy catalogue incompleteness: improving the dark siren measurement of the Hubble constant". In: *Monthly Notices of the Royal Astronomical Society* 512.1 (Feb. 2022), pp. 1127–1140. DOI: 10.1093/mnras/stac366. URL: https://doi.org/10.1093%5C%2Fmnras%5C%2Fstac366.

[49] B. P. Abbott and et al. "GWTC-1: A Gravitational-Wave Transient Catalog of Compact Binary Mergers Observed by LIGO and Virgo during the First and Second Observing Runs". In: *Physical Review X* 9.3, 031040 (July 2019), p. 031040. DOI: 10.1103/PhysRevX.9.031040. arXiv: 1811.12907 [astro-ph.HE].

[50] B. P. Abbott and et al. "GW170817: Observation of Gravitational Waves from a Binary Neutron Star Inspiral". In: *Phys. Rev. Lett.* 119 (16 Oct. 2017), p. 161101. DOI: 10.1103/PhysRevLett.119.161101. URL: https://link.aps.org/doi/10.1103/PhysRevLett.119.161101.

[51] B. P. Abbott and et al. "Gravitational Waves and Gamma-Rays from a Binary Neutron Star Merger: GW170817 and GRB 170817A". In: *The Astrophysical Journal* 848.2 (Oct. 2017), p. L13. DOI: 10.3847/2041-8213/aa920c. URL: https://doi.org/10.3847/2041-8213/aa920c.

[52] B. P. Abbott and et al. "Multi-messenger Observations of a Binary Neutron Star Merger". In: *The Astrophysical Journal* 848.2 (Oct. 2017), p. L12. DOI: 10.3847/2041-8213/aa91c9. URL: https://doi.org/10.3847/2041-8213/aa91c9.

[53] A. Goldstein and et al. "An Ordinary Short Gamma-Ray Burst with Extraordinary Implications:Fermi-GBM Detection of GRB 170817A". In: *The Astrophysical Journal* 848.2 (Oct. 2017), p. L14. DOI: 10.3847/2041-8213/aa8f41. URL: https://doi.org/10.3847/2041-8213/aa8f41.

[54] V. Savchenko and et al. "INTEGRAL:Detection of the First Prompt Gamma-Ray Signal Coincident with the Gravitational-wave Event GW170817". In: *The*

Astrophysical Journal 848.2 (Oct. 2017), p. L15. DOI: 10.3847/2041-8213/aa8f94. URL: https://doi.org/10.3847/2041-8213/aa8f94.

[55] D. A. Coulter and et al. "Swope Supernova Survey 2017a (SSS17a), the optical counterpart to a gravitational wave source". In: *Science* 358.6370 (Dec. 2017), pp. 1556–1558. DOI: 10.1126/science.aap9811. URL: https://doi.org/10.1126%5C%2Fscience.aap9811.

[56] M. Soares-Santos and et al. "The Electromagnetic Counterpart of the Binary Neutron Star Merger LIGO/Virgo GW170817. I. Discovery of the Optical Counterpart Using the Dark Energy Camera". In: *The Astrophysical Journal* 848.2 (Oct. 2017), p. L16. DOI: 10.3847/2041-8213/aa9059. URL: https://doi.org/10.3847/2041-8213/aa9059.

[57] S. Valenti and et al. "The Discovery of the Electromagnetic Counterpart of GW170817: Kilonova AT 2017gfo/DLT17ck". In: *The Astrophysical Journal* 848.2 (Oct. 2017), p. L24. DOI: 10.3847/2041-8213/aa8edf. URL: https://doi.org/10.3847/2041-8213/aa8edf.

[58] N. R. Tanvir and et al. "The Emergence of a Lanthanide-rich Kilonova Following the Merger of Two Neutron Stars". In: *The Astrophysical Journal* 848.2 (Oct. 2017), p. L27. DOI: 10.3847/2041-8213/aa90b6. URL: https://doi.org/10.3847/2041-8213/aa90b6.

[59] V. M. Lipunov and et al. "MASTER Optical Detection of the First LIGO/Virgo Neutron Star Binary Merger GW170817". In: *The Astrophysical Journal* 850.1 (Nov. 2017), p. L1. DOI: 10.3847/2041-8213/aa92c0. URL: https://doi.org/10.3847/2041-8213/aa92c0.

[60] A. Drlica-Wagner and et al. "Dark Energy Survey Year 1 Results: The Photometric Data Set for Cosmology". In: *The Astrophysical Journal Supplement Series* 235.2 (Apr. 2018), p. 33. DOI: 10.3847/1538-4365/aab4f5. URL: https://doi.org/10.3847/1538-4365/aab4f5.

[61] T. M. C. Abbott and et al. "The Dark Energy Survey: Data Release 1". In: *The Astrophysical Journal Supplement Series* 239.2 (Nov. 2018), p. 18. DOI: 10.3847/1538-4365/aae9f0. URL: https://doi.org/10.3847/1538-4365/aae9f0.

[62] D. J. White and et al. "A list of galaxies for gravitational wave searches". In: *Classical and Quantum Gravity* 28.8, 085016 (Apr. 2011), p. 085016. DOI: 10.1088/0264-9381/28/8/085016. arXiv: 1103.0695 [astro-ph.CO].

[63] M. Bilicki and et al. "Two Micron All Sky Survey Photometric Redshift Catalog: A Comprehensive Three-dimensional Census of the Whole Sky". In: 210.1, 9 (Jan. 2014), p. 9. DOI: 10.1088/0067-0049/210/1/9. arXiv: 1311.5246 [astro-ph.CO].

[64] M. F. Skrutskie and et al. "The Two Micron All Sky Survey (2MASS)". In: 131.2 (Feb. 2006), pp. 1163–1183. DOI: 10.1086/498708.

[65] D. Makarov and et al. "HyperLEDA. III. The catalogue of extragalactic distances". In: 570, A13 (Oct. 2014), A13. DOI: 10.1051/0004-6361/201423496. arXiv: 1408.3476 [astro-ph.GA].

[66] Pâris, I. and et al. "The Sloan Digital Sky Survey Quasar Catalog: Twelfth data release". In: *A&A* 597 (2017), A79. DOI: 10.1051/0004-6361/201527999. URL: https://doi.org/10.1051/0004-6361/201527999.

[67] B. Hoyle and et al. "Dark Energy Survey Year 1 Results: redshift distributions of the weak-lensing source galaxies". In: *Monthly Notices of the Royal Astronomical Society* 478.1 (Apr. 2018), pp. 592–610. ISSN: 0035-8711. DOI: 10.1093/mnras/sty957. eprint: https://academic.oup.com/mnras/article-pdf/478/1/592/25005892/sty957.pdf. URL: https://doi.org/10.1093/mnras/sty957.

[68] N. Gehrels and et al. "GALAXY STRATEGY FOR LIGO-VIRGO GRAVITATIONAL WAVE COUNTERPART SEARCHES". In: *The Astrophysical Journal* 820.2 (Mar. 2016), p. 136. DOI: 10.3847/0004-637x/820/2/136. URL: https://doi.org/10.3847/0004-637x/820/2/136.

[69] B. P. Abbott and et al. "Binary Black Hole Population Properties Inferred from the First and Second Observing Runs of Advanced LIGO and Advanced Virgo". In: *The Astrophysical Journal* 882.2 (Sept. 2019), p. L24. DOI: 10.3847/2041-8213/ab3800. URL: https://doi.org/10.3847/2041-8213/ab3800.

[70] R. Abbott and et al. "GWTC-2: Compact Binary Coalescences Observed by LIGO and Virgo during the First Half of the Third Observing Run". In: *Physical Review X* 11.2 (June 2021). DOI: 10.1103/physrevx.11.021053. URL: https://doi.org/10.1103%5C%2Fphysrevx.11.021053.

[71] R. Abbott and et al. *GWTC-2.1: Deep Extended Catalog of Compact Binary Coalescences Observed by LIGO and Virgo During the First Half of the Third Observing Run*. 2021. DOI: 10.48550/ARXIV.2108.01045. URL: https://arxiv.org/abs/2108.01045.

[72] R. Abbott and et al. *GWTC-3: Compact Binary Coalescences Observed by LIGO and Virgo During the Second Part of the Third Observing Run*. 2021. DOI: 10.48550/ARXIV.2111.03606. URL: https://arxiv.org/abs/2111.03606.

[73] R. Abbott and et al. *The population of merging compact binaries inferred using gravitational waves through GWTC-3*. 2021. DOI: 10.48550/ARXIV.2111.03634. URL: https://arxiv.org/abs/2111.03634.

[74] R. Abbott and et al. *Constraints on the cosmic expansion history from GWTC-3*. 2021. DOI: 10.48550/ARXIV.2111.03604. URL: https://arxiv.org/abs/2111.03604.

[75] G. Dálya and et al. "GLADE : an extended galaxy catalogue for multimessenger searches with advanced gravitational-wave detectors". In: *Monthly Notices of the Royal Astronomical Society* 514.1 (May 2022), pp. 1403–1411. DOI: 10.1093/mnras/stac1443. URL: https://doi.org/10.1093%5C%2Fmnras%5C%2Fstac1443.

[76] M. Bilicki and et al. "WISE×SuperCOSMOS PHOTOMETRIC REDSHIFT CATALOG: 20 MILLION GALAXIES OVER 3π STERADIANS". In: *The Astro-*

physical Journal Supplement Series 225.1 (July 2016), p. 5. DOI: 10.3847/0067-0049/225/1/5. URL: https://doi.org/10.3847/0067-0049/225/1/5.

[77] B. W. Lyke and et al. "The Sloan Digital Sky Survey Quasar Catalog: Sixteenth Data Release". In: *The Astrophysical Journal Supplement Series* 250.1 (Aug. 2020), p. 8. DOI: 10.3847/1538-4365/aba623. URL: https://doi.org/10.3847/1538-4365/aba623.

[78] C. S. Kochanek and et al. "The K-Band Galaxy Luminosity Function". In: *The Astrophysical Journal* 560.2 (Oct. 2001), pp. 566–579. DOI: 10.1086/322488. URL: https://doi.org/10.1086/322488.

[79] P. Norberg and et al. "The 2dF Galaxy Redshift Survey: the bJ-band galaxy luminosity function and survey selection function". In: *Monthly Notices of the Royal Astronomical Society* 336.3 (Nov. 2002), pp. 907–931. ISSN: 0035-8711. DOI: 10.1046/j.1365-8711.2002.05831.x. eprint: https://academic.oup.com/mnras/article-pdf/336/3/907/2959521/336-3-907.pdf. URL: https://doi.org/10.1046/j.1365-8711.2002.05831.x.

[80] R. Abbott and et al. "GW190814: Gravitational Waves from the Coalescence of a 23 Solar Mass Black Hole with a 2.6 Solar Mass Compact Object". In: *The Astrophysical Journal Letters* 896.2 (June 2020), p. L44. DOI: 10.3847/2041-8213/ab960f. URL: https://doi.org/10.3847/2041-8213/ab960f.

[81] B. P. Abbott and et al. "GW190425: Observation of a Compact Binary Coalescence with Total Mass 3.4 $M_{\odot}$". In: *The Astrophysical Journal Letters* 892.1 (Mar. 2020), p. L3. DOI: 10.3847/2041-8213/ab75f5. URL: https://doi.org/10.3847%5C%2F2041-8213%5C%2Fab75f5.

[82] R. Abbott and et al. "Observation of Gravitational Waves from Two Neutron Star–Black Hole Coalescences". In: *The Astrophysical Journal Letters* 915.1 (June 2021), p. L5. DOI: 10.3847/2041-8213/ac082e. URL: https://doi.org/10.3847/2041-8213/ac082e.

[83] F. Mannucci and et al. "A fundamental relation between mass, star formation rate and metallicity in local and high-redshift galaxies". In: *Monthly Notices of*

the Royal Astronomical Society 408.4 (Oct. 2010), pp. 2115–2127. ISSN: 0035-8711. DOI: 10.1111/j.1365-2966.2010.17291.x. eprint: https://academic.oup.com/mnras/article-pdf/408/4/2115/4220896/mnras0408-2115.pdf. URL: https://doi.org/10.1111/j.1365-2966.2010.17291.x.

[84] V. Sommariva and et al. "Stellar metallicity of star-forming galaxies at z ~3". In: 539, A136 (Mar. 2012), A136. DOI: 10.1051/0004-6361/201118134. arXiv: 1112.2403 [astro-ph.CO].

[85] M. R. Krumholz and A. Dekel. "Metallicity-dependent Quenching of Star Formation at High Redshift in Small Galaxies". In: 753.1, 16 (July 2012), p. 16. DOI: 10.1088/0004-637X/753/1/16. arXiv: 1106.0301 [astro-ph.CO].

[86] P. Dayal and et al. "The physics of the fundamental metallicity relation". In: 430.4 (Apr. 2013), pp. 2891–2895. DOI: 10.1093/mnras/stt083. arXiv: 1202.4770 [astro-ph.CO].

[87] R. Farmer and et al. "Mind the Gap: The Location of the Lower Edge of the Pair-instability Supernova Black Hole Mass Gap". In: 887.1, 53 (Dec. 2019), p. 53. DOI: 10.3847/1538-4357/ab518b. arXiv: 1910.12874 [astro-ph.SR].

[88] S. Mukherjee. "The redshift dependence of black hole mass distribution: Is it reliable for standard sirens cosmology?" In: *Monthly Notices of the Royal Astronomical Society* (Aug. 2022). DOI: 10.1093/mnras/stac2152. URL: https://doi.org/10.1093%5C%2Fmnras%5C%2Fstac2152.

[89] C. Karathanasis and et al. *Binary black holes population and cosmology in new lights: Signature of PISN mass and formation channel in GWTC-3*. 2022. DOI: 10.48550/ARXIV.2204.13495. URL: https://arxiv.org/abs/2204.13495.

[90] G. Rakavy and G. Shaviv. "Instabilities in Highly Evolved Stellar Models". In: 148 (June 1967), p. 803. DOI: 10.1086/149204.

[91] Gary S. Fraley. "Supernovae Explosions Induced by Pair-Production Instability". In: 2.1 (Aug. 1968), pp. 96–114. DOI: 10.1007/BF00651498.

[92] M. Spera and M. Mapelli. "Very massive stars, pair-instability supernovae and intermediate-mass black holes with the sevn code". In: *Monthly Notices of the Royal Astronomical Society* 470.4 (June 2017), pp. 4739–4749. ISSN: 0035-8711. DOI: 10.1093/mnras/stx1576. eprint: https://academic.oup.com/mnras/article-pdf/470/4/4739/19287655/stx1576.pdf. URL: https://doi.org/10.1093/mnras/stx1576.

[93] M. Renzo and et al. "Sensitivity of the lower edge of the pair-instability black hole mass gap to the treatment of time-dependent convection". In: *Monthly Notices of the Royal Astronomical Society* 493.3 (Mar. 2020), pp. 4333–4341. ISSN: 0035-8711. DOI: 10.1093/mnras/staa549. eprint: https://academic.oup.com/mnras/article-pdf/493/3/4333/32920635/staa549.pdf. URL: https://doi.org/10.1093/mnras/staa549.

[94] K. Belczynski and et al. "A Comprehensive Study of Binary Compact Objects as Gravitational Wave Sources: Evolutionary Channels, Rates, and Physical Properties". In: 572.1 (June 2002), pp. 407–431. DOI: 10.1086/340304. arXiv: astro-ph/0111452 [astro-ph].

[95] Dominik M. and et al. "DOUBLE COMPACT OBJECTS. I. THE SIGNIFICANCE OF THE COMMON ENVELOPE ON MERGER RATES". In: *The Astrophysical Journal* 759.1 (Oct. 2012), p. 52. DOI: 10.1088/0004-637x/759/1/52. URL: https://doi.org/10.1088/0004-637x/759/1/52.

[96] M. Dominik and et al. "DOUBLE COMPACT OBJECTS. III. GRAVITATIONAL-WAVE DETECTION RATES". In: *The Astrophysical Journal* 806.2 (June 2015), p. 263. DOI: 10.1088/0004-637x/806/2/263. URL: https://doi.org/10.1088/0004-637x/806/2/263.

[97] M. Mapelli and et al. "The cosmic merger rate of stellar black hole binaries from the Illustris simulation". In: *Monthly Notices of the Royal Astronomical Society* 472.2 (Aug. 2017), pp. 2422–2435. ISSN: 0035-8711. DOI: 10.1093/mnras/stx2123. eprint: https://academic.oup.com/mnras/article-pdf/472/2/2422/19943102/stx2123.pdf. URL: https://doi.org/10.1093/mnras/stx2123.

[98] N. Giacobbo and et al. "Merging black hole binaries: the effects of progenitor's metallicity, mass-loss rate and Eddington factor". In: *Monthly Notices of the Royal Astronomical Society* 474.3 (Nov. 2017), pp. 2959–2974. ISSN: 0035-8711. DOI: 10.1093/mnras/stx2933. eprint: https://academic.oup.com/mnras/article-pdf/474/3/2959/22843349/stx2933.pdf. URL: https://doi.org/10.1093/mnras/stx2933.

[99] Mohammadtaher S. and W. M. Farr. "The Impact of Metallicity Evolution of the Universe on the Maximum Mass of LIGO Binary Black Holes". In: *The Astrophysical Journal* 883.1 (Sept. 2019), p. L24. DOI: 10.3847/2041-8213/ab40bd. URL: https://doi.org/10.3847/2041-8213/ab40bd.

[100] M. Toffano and et al. "The host galaxies of double compact objects across cosmic time". In: *Monthly Notices of the Royal Astronomical Society* 489.4 (Sept. 2019), pp. 4622–4631. ISSN: 0035-8711. DOI: 10.1093/mnras/stz2415. eprint: https://academic.oup.com/mnras/article-pdf/489/4/4622/30040415/stz2415.pdf. URL: https://doi.org/10.1093/mnras/stz2415.

[101] P. Kroupa. "The Initial mass function of stars: Evidence for uniformity in variable systems". In: *Science* 295 (2002), pp. 82–91. DOI: 10.1126/science.1067524. arXiv: astro-ph/0201098.

[102] R. Farmer et al. "Mind the Gap: The Location of the Lower Edge of the Pair-instability Supernova Black Hole Mass Gap". In: *The Astrophysical Journal* 887.1 (Dec. 2019), p. 53. ISSN: 1538-4357. DOI: 10.3847/1538-4357/ab518b. URL: http://dx.doi.org/10.3847/1538-4357/ab518b.

[103] C. Karathanasis and et al. *GWSim: A python package to create GW mock samples for different astrophysical populations and cosmological models of binary black holes*. 2022. DOI: 10.48550/ARXIV.2210.05724. URL: https://arxiv.org/abs/2210.05724.

[104] P. Fosalba and et al. "The MICE grand challenge lightcone simulation - I. Dark matter clustering". In: 448.4 (Apr. 2015), pp. 2987–3000. DOI: 10.1093/mnras/stv138. arXiv: 1312.1707 [astro-ph.CO].

[105] M. Crocce and et al. "The MICE Grand Challenge lightcone simulation – II. Halo and galaxy catalogues". In: *Monthly Notices of the Royal Astronomical Society* 453.2 (Aug. 2015), pp. 1513–1530. DOI: 10.1093/mnras/stv1708. URL: https://doi.org/10.1093%5C%2Fmnras%5C%2Fstv1708.

[106] P. Fosalba and et al. "The MICE Grand Challenge light-cone simulation – III. Galaxy lensing mocks from all-sky lensing maps". In: *Monthly Notices of the Royal Astronomical Society* 447.2 (Dec. 2014), pp. 1319–1332. DOI: 10.1093/mnras/stu2464. URL: https://doi.org/10.1093%5C%2Fmnras%5C%2Fstu2464.

[107] Gregory Ashton et al. "BILBY: A user-friendly Bayesian inference library for gravitational-wave astronomy". In: *Astrophys. J. Suppl.* 241.2 (2019), p. 27. DOI: 10.3847/1538-4365/ab06fc. arXiv: 1811.02042 [astro-ph.IM].

[108] T. A. Callister and et al. "Who Ordered That? Unequal-mass Binary Black Hole Mergers Have Larger Effective Spins". In: *Astrophys. J. Lett.* 922.1 (2021), p. L5. DOI: 10.3847/2041-8213/ac2ccc. arXiv: 2106.00521 [astro-ph.HE].